이학박사 학위논문

Infrared Supernova Remnants in the Large Magellanic Cloud

대마젤란운의 적외선 초신성 잔해

2012년 8월

서울대학교 대학원
물리천문학부 천문학전공
석 지 연

Infrared Supernova Remnants in the Large Magellanic Cloud

대마젤란운의 적외선 초신성 잔해

지도교수 구 본 철

이 논문을 이학박사 학위논문으로 제출함

2012년 4월

서울대학교 대학원

물리천문학부 천문학전공

석 지 연

석 지 연의 이학박사 학위논문을 인준함

2012년 6월

위 원 장 _____

부 위 원 장 _____

위 원 _____

위 원 _____

위 원 _____

학위논문 원문제공 서비스에 대한 동의서

본인의 학위논문에 대하여 서울대학교가 아래와 같이 학위논문 저작물을 제공하는 것에 동의합니다.

1. 동의사항

   (a) 본인의 논문을 보존이나 인터넷 등을 통한 온라인 서비스 목적으로 복제할 경우 저작물의 내용을 변경하지 않는 범위 내에서의 복제를 허용합니다.

   (b) 본인의 논문을 디지털화하여 인터넷 등 정보통신망을 통한 논문의 일부 또는 전부의 복제·배포 및 전송 시 무료로 제공하는 것에 동의합니다.

2. 개인(저작자)의 의무

   본 논문의 저작권을 타인에게 양도하거나 또는 출판을 허락하는 등 동의 내용을 변경하고자 할 때는 소속대학(원)에 공개의 유보 또는 해지를 즉시 통보하겠습니다.

3. 서울대학교의 의무

   (a) 서울대학교는 본 논문을 외부에 제공할 경우 저작권 보호장치(DRM)를 사용하여야 합니다.

   (b) 서울대학교는 본 논문에 대한 공개의 유보나 해지 신청 시 즉시 처리해야 합니다.

논문제목: Infrared Supernova Remnants in the Large Magellanic Cloud

학 위 구 분 : 이학박사
학 과 : 서울대학교 대학원 물리천문학부 천문학전공
학 번 : 2006-20463
연 락 처 : jyseok@astro.snu.ac.kr
저 작 자 : 석 지 연 (인)

제 출 일 : 2012년 8월 일

서울대학교총장 귀하

Infrared Supernova Remnants in the Large Magellanic Cloud

by

Ji Yeon Seok
(jyseok@astro.snu.ac.kr)

A dissertation submitted in partial fulfillment of the requirements for the degree of

Doctor of Philosophy

in

Astronomy

in

Astronomy Program
Department of Physics and Astronomy
Seoul National University

Committee:

Professor	Hyung Mok Lee
Professor	Bon-Chul Koo
Professor	Takashi Onaka
Professor	Myung Gyoon Lee
Professor	Woong-Tae Kim

ABSTRACT

Supernova remnants (SNRs) are unique places where we can study the physical and chemical evolution of the interstellar medium by SN shocks. In particular, dust processing by shocks can be directly investigated by observing SNRs in infrared (IR) wavebands. I present the near- to mid-IR (NIR/MIR) study of SNRs using the *AKARI* and *Spitzer* data of the Large Magellanic Cloud (LMC).

The LMC has a great advantage to study IR emission from SNRs thanks to its low IR confusion compared to the Milky Way. I systematically examine both the *AKARI* and *Spitzer* images of all known 45 LMC SNRs and could identify 28 SNRs with distinguishable IR emission in total. 13 SNRs are firstly identified in several IR bands by this study. Measured fluxes as well as general information are listed in catalogs for further studies. Using IR flux correlations as well as IR colors, the origins of IR emission from SNRs are examined. Even if the correlations or the IR colors can suggest the origins, however, more direct evidence is required to confirm the dominant emission mechanism. The IR emission is compared with X-ray and radio, and correlations are found among the emissions. Good correlation between the *Spitzer* 24/70 ratios and plasma properties (gas temperature and density) can verify the dust heating and cooling physics. IR faint LMC SNRs relative to their radio brightnesses are newly found, which indicates that the contribution of SNRs might be small to the total IR luminosity of galaxies. The high detection rate of IR SNRs in the LMC is remarkable compared to that of Galactic SNRs, and the low IR confusion is thought to be a primary reason for it. I discuss the origin of IR emission for all detected SNRs, which is important for correct understanding of shock processing and evolution of SNRs.

I also carried out a detailed study of SNR N49 in the LMC with the NIR ($2.5 - 5$ μm) spectroscopic observations performed by *AKARI*. The observations were performed as a coarse spectral mapping to cover most of the bright region in the east, which enables me to compare the distribution of various line emissions and to

examine their correlation. I detect the 3.3 μm aromatic feature in the remnant, which is for the first time to report the presence of the 3.3 μm aromatic feature related to a SNR. In the line maps of H_2 1-0 O(3), 3.3 μm feature, and Brα, the distribution of the aromatic feature shows overall correlation with those of other emissions together with regional differences reflecting the local physical conditions. By comparison with other archival imaging data at different wavelengths, the association of the aromatic emission to other ionic/molecular emission is clarified. I examine archival *Spitzer* IRS data of N49 and find signatures of other polycyclic aromatic hydrocarbon (PAH) features at 6.2, 7.7, and 11.3 μm corresponding to the 3.3 μm aromatic feature. Based on the band ratios of PAHs, I find that PAHs in N49 are not only dominantly neutral but also small in size. I discuss the origin of the PAH emission in N49 and conclude that the emission is either from PAHs that have survived the shock or PAHs in the preshock gas heated by radiative precursor.

Keywords: ISM: dust, extinction – infrared: ISM: lines and bands – ISM: supernova remnants – Magellanic Clouds

Student Number: 2006-20463

Contents

List of Figures

List of Tables

Chapter 1

Introduction

1.1 SNRs in IR

A supernova (SN) explosion is one of the most energetic events in the Universe ejecting various elements of stellar mass including synthesized heavy elements with an enormous kinetic energy (E $\sim 10^{51}$ erg). A significant amount of dust grains may be formed in the SN ejecta too, although its contribution to dusty galaxies in the early Universe is still controversial (e.g., Draine 2009). It plays an important role in the physical and chemical evolution of the interstellar medium (ISM) by generating strong shocks which heat and accelerate the medium, and in particular, dust grains in the ISM can be eroded, fragmented, or sputtered by experiencing shock waves.

These processes can be studied by observing the remnants of the explosion, supernova remnants (SNRs), at various wavelengths. In particular, infrared (IR) observation is a new window to probe SNRs compared to other wavelengths such as radio, optical, and X-ray. *Infrared Astronomy Satellite (IRAS)* opened an era of IR studies in 1980s by detecting IR emission from a number of SNRs (e.g., Arendt 1989; Saken et al. 1992). The instrumental abilities such as spatial resolution and wavelength coverage, however, had several limitations to reveal the nature of the IR emission from individual SNRs in detail. Since the *IRAS*, instrumental tech-

nology has remarkably progressed in recent decades, and *Spitzer Space Telescope*, launched in 2003, and *AKARI infrared space telescope* launched in 2006, have made significant improvements in this field. These IR observations enable us to study IR morphology of SNRs, interaction between SN shocks and ambient medium, and especially physical processes associated with dust grains because dust grains, either newly synthesized or swept-up by SN shocks, radiate essentially only in the IR.

1.2 Mechanisms of IR Emission

There are four sources of the IR emission in SNRs in general; ionic/molecular emission lines, thermal dust continuum, non-thermal synchrotron emission, and polycyclic aromatic hydrocarbon (PAH) bands (see Koo et al. 2007, and references therein). Synchrotron emission predominates only for a young pulsar wind nebula (PWN) such as Crab. PAH emission is suggested as one of the IR origins based on the IR colors (Reach et al. 2006), but only few detections have been reported (e.g., Tappe et al. 2006) although one of the path ways to form PAHs is theoretically expected to be the fragmentation of larger grains by shocks (Jones et al. 1996). It is usually either the thermal dust emission or line emission that dominate the IR emission in this wave band. Thermal continuum originates from collisionally-heated dust grains in hot plasma (e.g., Dwek 1987). Line emission is observed from hot gas swept up by radiative shocks. For ionic lines, there are the forbidden lines from the elements such as Ne, O, Fe ions or hydrogen recombination lines such as Brα at 4.05 μm. Molecular lines are mainly transitional lines of molecular hydrogens such as various rotational H_2 lines (e.g., pure rotational: 0-0 S(0) at 28.2 μm to S(19) at 3.40 μm, ro-vibrational: 1-0 O(3) at 2.80 μm to O(8) at 4.16 μm).

1.3 Large Magellanic Cloud

The Large Magellanic Cloud (LMC) is a nearby irregular galaxy and is a satellite galaxy of the Milky Way. The LMC is different from the Milky Way in many ways.

Its metallicity is about one third of the Galactic metallicity, and the dust-to-gas ratio is one fifth of the Galactic ratio (Pei 1992). In addition, dust composition is different; The Galactic and LMC extinction curves require a mixture of both graphite and silicate grains, and the graphite-to-silicate abundance ratio (r_c/r_s) of the Galaxy is about four times higher than the ratio of the LMC ($r_c/r_s = 0.95$ and 0.22, respectively, Pei 1992). (Even the extinction curve of the Small Magellanic Cloud can be fitted by silicate grain alone.) These facts could suggest that the relative abundance of carbonaceous compound decreases from the Galaxy to the LMC (to the SMC). In terms of SNe/SNRs, the SN rate for the LMC ($\sim$ 0.5 per 100 yr) is one fifth of the Galaxy ($\sim$ 2.5 per 100 yr, Tammann et al. 1994). By SN type, the ratio of SN Ia to SNe II + Ib (core-collapse SN) is 1:11 for the LMC, while 1:6.3 for the Galaxy (adopting Sbc as the Galactic Hubble type, Tammann et al. 1994). The SN rate is known to depend on the luminosity of a galaxy and on its Hubble type.

The LMC is a unique place for studying IR SNRs. It is relatively close, so we can see the detailed structure of SNRs ($\sim$ 50 kpc, Panagia 1999). There are more than forty radio/X-ray SNRs offering non-biased samples with the well-known distance (e.g., Desai et al. 2010). Since the distance ambiguity of the Galactic SNRs often exists, this is one of the strong advantages to study SNRs in the LMC. However, the most important advantage compared to Galactic SNRs is that the LMC is located far off from the Galactic plane, therefore, we can avoid much back/foreground confusion by a number of IR sources.

Understanding the IR properties of the Magellanic (and the Galactic) SNRs is also useful in interpreting the IR emission from SNRs in remote galaxies where we cannot resolve them. As we mentioned above, the IR emission can be emitted by various physical processes in several distinct regions. For the SNRs in remote galaxies, therefore, modeling is essential. For example, Tanaka et al. (2012) detect IR emission in a very young ($\leq$ 100 yrs) SNR in NGC 1313 using the *Spitzer* and *AKARI* space telescopes and conclude that the IR emission might be from

circumstellar dust swept up by the blast wave. The IR emission is also expected from newly-formed dust in cooling, metal-rich SN ejecta (see Nozawa et al. 2010, and the references therein), but the estimated dust masses from the IR emission are usually insignificant except in the LMC SNR 1987A and in Cas A where dust masses as large as 0.2 to 0.7 $M_{\odot}$ have been detected (Matsuura et al. 2011; Sibthorpe et al. 2010). It is clear that the natures and the physical environments of SNe/SNRs are diverse, and the understanding of the IR emission from remote SNRs should be proceded with understanding of the IR properties of the nearby SNRs.

1.4 IR survey of SNRs

1.4.1 Galactic SNRs

Since *IRAS* was launched, several IR studies on Galactic SNRs have been done by using a large number of samples. Dwek et al. (1987) compared IR and X-ray fluxes of nine SNRs with both IR and X-ray emission to probe their main cooling process. There are statistical studies of entire Galactic SNRs (e.g., Arendt 1989; Saken et al. 1992); Arendt (1989) found 51 SNRs with probable/possible IR emission out of 157 Galactic SNRs and probe any correlations between IR and other wavelength fluxes. The above studies, however, had instrumental limitations in both spatial resolution and sensitivity, and more seriously, confusion with other Galactic sources such as HII regions was a big problem. One of the *Spitzer* Legacy programs, Galactic Legacy Infrared Mid-Plane Survey Extraordinaire (GLIMPSE), has provided much improved data with the four IRAC arrays with filters centered at 3.6, 4.5, 5.8, and 8 μm. The GLIMPSE survey has mapped the inner Galaxy ($10^{\circ} < |l| < 65^{\circ}$, $|b| < 1^{\circ}$). Reach et al. (2006) and Lee (2005) have independently searched IR SNRs within the survey field and detected 18 and 16 IR SNRs out of 95 and 100 SNRs, respectively. The GLIMPSE is a significant advance both because of the large increase in angular resolution and sensitivity and because of a new coverage set of IR wavelengths (Reach et al. 2006). However, significant confusion from back/foreground sources is

still inevitable, and no data for outer Galaxy is one of its limitations.

1.4.2 SNRs in the LMC

For LMC SNRs, there are some previous works by using *IRAS* data (e.g., Graham et al. 1987; Schwering 1989). These early works, however, could not detect many IR SNRs because of their relatively small sizes compared to the spatial resolution and lack of known samples at those time. The *Spitzer* observations enable us to study more detailed structure of SNRs in the LMC. Using the recent *Spitzer* Survey of the LMC: Surveying the Agents of a Galaxy Evolution (SAGE, Meixner et al. 2006), it becomes possible to investigate almost the whole region of the LMC ($7^\circ \times 7^\circ$) at $3-8$ μm and at $24-160$ μm. R. Williams et al. (2006) detected four with IR emission at several bands out of six SNRs by using their independent observations and discussed the origin of IR emission in those SNRs. In addition to this, a separate survey of 39 LMC SNRs was conducted to study the interstellar dust lifecycle in terms of ejecta formation by SNe and dust destruction by SNR blast waves (PI: K. Borkowski). Its preliminary results suggest that a substantial amount of small grains are destroyed in both Type Ia (Borkowski et al. 2006a) and core-collapse SNRs (B. Williams et al. 2006). Tappe et al. (2006) reported the detection of bright mid-infrared (MIR) emission together with the PAH features in the oxygen-rich SNR N132D using the *Spitzer* imaging and spectroscopy.

More recently *AKARI* has performed a large scale survey of the LMC (Ita et al. 2008, and see § 2.2.1). The *AKARI* has a continuous coverage of imaging from $2.5-26$ μm, which is a powerful tool to investigate the IR traits of SNRs. In particular, the 11 and 15 μm bands are unique to *AKARI* and could provide important information unobtainable with *Spitzer* observations. While there are various studies about individual SNRs using the numerous IR data, more statistical studies including entire SNRs in the LMC have not been done yet, so it becomes essential to study SNRs and their environment with a large number of samples.

1.5 Multi-wavelength survey of LMC SNRs

Unlike IR studies on LMC SNRs, various surveys at multi-wavelengths have been performed previously and have been used for statistical studies. At radio and X-ray, Filipovic et al. (1998) compared radio and X-ray fluxes of 36 LMC SNRs/SNR candidates by using *Parkes* radio observations and *ROSAT* X-ray survey data, and R. Williams et al. (1999) also studied X-ray properties of 31 LMC SNRs with *ROSAT* data. At optical wavelengths, Smith et al. (2000) performed Magellanic Cloud Emission Line Survey (MCELS) to cover most LMC region with [O III], Hα, and [S II] and discovered new SNRs/SNR candidates based on a high [S II]/Hα ratio. Also, there is a long slit optical spectroscopic survey of 25 LMC SNRs (Payne et al. 2008). At ultra-violet (UV) wavelengths, *FUSE* far-UV survey of 38 LMC SNRs has been done and found 14 SNRs with UV emission (Blair et al. 2006). Based on the above data, multi-wavlength studies with large samples of LMC SNRs have recently been done, for example, to probe star formation around a SNR (Desai et al. 2010) or to investigate a size distribution of LMC SNRs (Badenes et al. 2010).

1.6 PAH emission in a SNR

In PAH processing, interstellar shocks are known to play a crucial role. It is largely accepted that PAHs could be either the remaining dust condensation nuclei that escaped the grain growth process in asymptotic giant branch ejecta or the fragmentation of dust grains through shattering collision in fast interstellar shocks (e.g., Tielens 2008; Jones et al. 1996). Also, interstellar shock waves have been considered as one of the main mechanisms to destroy PAH molecules. In spite of plentiful observations of PAH features, however, there are still unanswerable questions on the role of interstellar shocks in the evolution of PAHs. Particularly, how supernova shocks affect PAH molecules is barely explored. Detection of PAH features in SNRs are unexpectedly rare, recalling that the one of their formation processes is related to interstellar shocks.

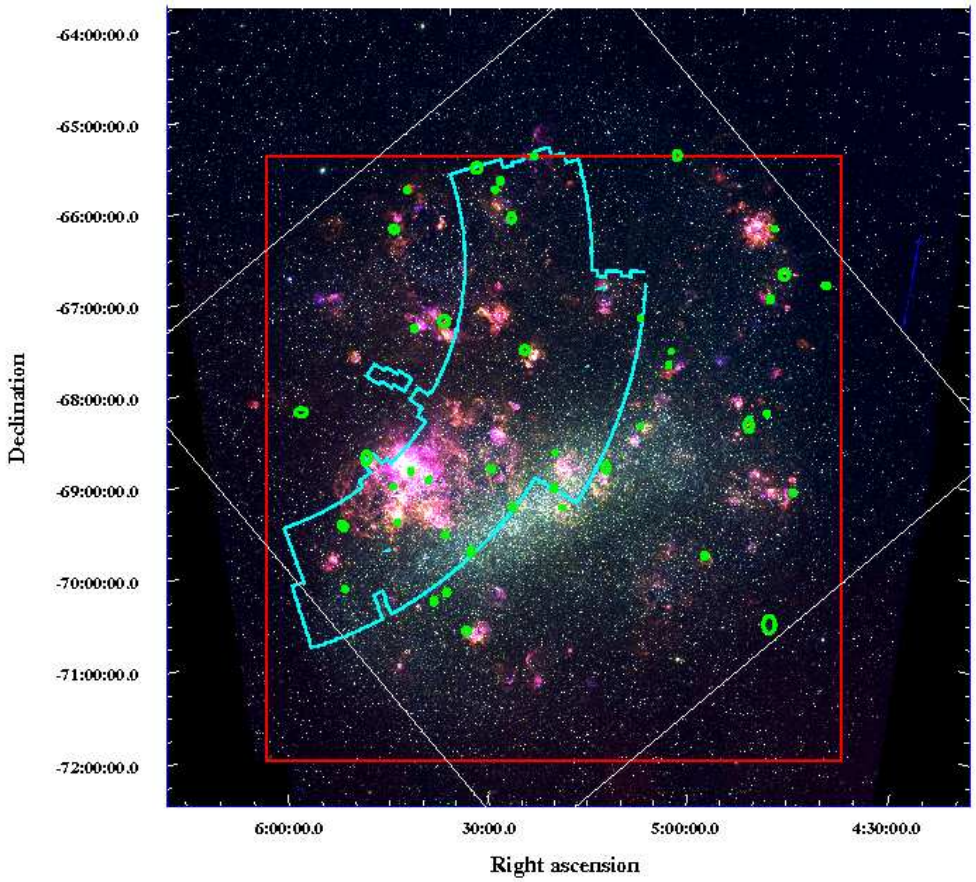

Figure 1.1 Distribution of all known 45 SNRs marked on the MCELS composite image of the LMC (Hα: *red*, [S II]: *green*, [O III]: *blue*). Green symbols represent the positions of SNRs, and the size of each symbol demonstrates the size of the corresponding SNR. The spatial coverage of the *AKARI* LMC survey (*cyan*), the *ATCA* radio survey (*red*), and the *Spitzer* SAGE survey (*white*) is also overlaid.

There have been considerable literatures dealing with the survivability of PAH molecules in shocked environments. In particular, since PAH emission has been categorized as one of the IR emission mechanisms expected for SNRs based on the *Spitzer* imaging data (Reach et al. 2006), substantial efforts have been made in order to search for observational evidence of PAH emission in SNRs. By using *Spitzer* Infrared Spectrograph (IRS) observations, Tappe et al. (2006) firstly reported the detection of $15 - 20$ μm hump attributed to C–C–C bending modes of large PAHs ($\sim$ 4000 C-atoms) with the weakly detected 11.3 μm PAH feature in a SNR N132D in the LMC. Based on the lack of PAH features at $6 - 9$ μm and the high ratio of $15 - 20$ μm hump to 11.3 μm feature, they, however, interpret that small PAHs are rapidly destroyed by thermal sputtering in the SN blast wave. Among the *Spitzer* IRS spectra of several Galactic SNRs, some in Neufeld et al. (2007) and Hewitt et al. (2009) also show the major PAH features with strong ionic and/or molecular lines, yet both authors have not mentioned the association of the features with the SNRs in the papers. In most cases that PAH emission is observed in SNRs, no convincing evidence for the PAH emission intrinsic to the SNRs has been reported. This lack of detection of PAH features in SNRs probably results from the difficulty of differentiation between PAH emission from SNRs and that from other back/foreground sources.

1.7 Purpose of Thesis

The main objectives of this thesis are as follows; By making catalogs of IR SNRs in the LMC, I would like to carry out statistical studies of the LMC SNRs with associated IR emission. Then, I focus on detailed investigation of PAH emission process in a SNR.

First of all, I summarize general information of all known LMC SNRs, and the noticeable content is the IR detection status of each SNR by *AKARI* and *Spitzer*. For the SNRs with IR emission, a separate catalog contains their IR fluxes measured

at the *AKARI* and/or *Spitzer* bands. In addition, the IR morphology of each SNR is described with their band images. These catalogs are expected to be useful and powerful for further both statistical and individual IR SNR studies. Based on the above catalog, I examine the characteristics of the IR SNRs in the LMC. The IR fluxes can be compared to other wavelength fluxes (e.g., radio or X-ray), and any correlations among them can be checked. In previous studies (e.g., Dwek et al. 1987), it is known that IR-to-X-ray flux ratios can be used as a measure of the relative importance of remnant cooling by gas-grain collisions to its cooling by atomic processes. Also, there is a well-known relation between FIR and radio fluxes for galaxies, and I can examine whether there is a similar correlation for SNRs. The origin of the IR emission in each SNR can be investigated by using, for example, several IR band ratios. For those dominated by dust continuum, dust properties such as mass and temperature can be estimated, and overall dust cooling and heating processes are discussed.

Since there have been only few piece of observational evidence, detecting PAH emission intrinsically associated with a SNR is important. Using *AKARI* and *Spitzer* spectroscopic observations, I detect PAH emission from the SNR N49, and correlations between PAH and other ionic/molecular line emission distribution are examined. If more than two PAH band features are detected, the PAH band ratios can be used as an indicator for charge states of PAHs. The charge state is proportional to local physical properties (i.e., $\sim G_0 T^{1/2}/n_e$, Tielens 2008), so I examine the local conditions in a SNR by using an empirical relation between a PAH band ratio and the physical properties (Galliano et al. 2008). Finally, I discuss the origin of PAH emission in a SNR. Survival conditions of PAHs in shocked environment and emission mechanism of PAH features in a SNR can be important issues.

Bibliography

Arendt, R. G. 1989, ApJS, 70, 181

Blair, W. P., Ghavamian, P., Sankrit, R., & Danforth, C. W. 2006, ApJS, 165, 480

Borkowski, K. J., Williams, B. J., Reynolds, S. P., et al. 2006, ApJ, 642, L141

Badenes, C., Maoz, D., & Draine, B. T. 2010, MNRAS, 407, 1301

Desai, K. M., et al. 2010, AJ, 140, 584

Draine, B. T. 2009, Cosmic Dust-Near and Far (ASP Conf. Ser. 414), ed. T. Henning, E. Grün, & J. Steinacker (San Francisco, CA: ASP), 453

Dwek, E. 1987, ApJ, 322, 812

Dwek, E., Petre, R., Szymkowiak, A., & Rice, W. L. 1987, ApJ, 320, L27

Filipovic, M. D., et al. 1998, A&AS, 127, 119

Galliano, F., Madden, S. C., Tielens, A. G. G. M., Peeters, E., & Jones, A. P. 2008, ApJ, 679, 310

Graham, J. R., Evans, A., Albinson, J. S., et al. 1987, ApJ, 319, 126

Hewitt, J. W., Rho, J., Andersen, M., & Reach, W. T. 2009, ApJ, 694, 1266

Jones, A. P., Tielens, A. G. G. M., & Hollenbach, D. J. 1996, ApJ, 469, 740

Koo, B.-C., Lee, H.-G., Moon, D.-S., et al. 2007, PASJ, 59S, 455

Lee, H.-G. 2005, Journal of Korean Astronomical Society, 38, 385

Matsuura, M., Dwek, E., Meixner, M., et al. 2011, Science, 333, 1258

Meixner, M., Gordon, K. D., Indebetouw, R., et al. 2006, AJ, 132, 2268

Neufeld, D. A., Hollenbach, D. J., Kaufman, M. J., et al. 2007, ApJ, 664, 890

Nozawa, T., Kozasa, T.,Tominaga, N., et al. 2010, ApJ, 713, 356

Panagia 1999, in IAU Symp. 190, New Views of the Magellanic Clouds, ed. Y.-H. Chu, N. Suntzeff, J. Hesser, and D. Bohlender (San Francisco: ASP), 549

Payne, J. L., Filipovic, M. D., Millar, W. C., et al. 2008, Serbian Astronomical Journal, 177, 53

Pei, Y. C. 1992, ApJ, 395, 130

Reach, W. T., Rho, J., Tappe, A., et al. 2006, AJ, 131, 1479

Saken, J. M., Fesen, R. A., & Shull, J. M. 1992, ApJS, 81, 715

Schwering, P. B. W. 1989, A&AS, 79, 105

Sibthorpe, B., Ade,P. A. R., Bock, J. J., et al. 2010, ApJ, 719, 1553

Smith, C., Leiton, R.,& Pizarro, S. 2000, Stars, Gas and Dust in Galaxies: Exploring the Links, 221, 83

Tammann, G. A., Loeffler, W., & Schroeder, A. 1994, ApJS, 92, 487

Tanaka, M., Nozawa, T., Sakon, I., et al. 2012, ApJ, 749, 173

Tappe, A., Rho, J., and Reach, W. T. 2006, ApJ, 653, 267

Tielens, A. G. G. M. 2008, ARA&A, 46, 289

Williams, B. J., Borkowski, K. J., Reynolds, S. P., et al. 2006, ApJ, 652, L33

Williams, R. M., Chu, Y.-H., and Gruendl, R. 2006, AJ, 132, 1877

Williams, R. M., Chu, Y.-H., Dickel, J. R., et al. 1999, ApJS, 123, 467

Chapter 2

Catalog of IR SNRs in the LMC

2.1 Introduction

Before the *IRAS* was launched, SNR studies, in particular, studies about a large number of SNRs had been carried out mainly in the radio, optical, and X-ray regimes. The All-Sky survey of the *IRAS* enabled us to complete a survey of Galactic SNRs in 10 to 100 μm bands for the first time. Arendt (1989) examine 157 objects and found 51 SNRs with probable IR emission. Later on, Saken et al. (1992) carried out an independent survey of the IR emission for 161 Galactic SNRs and could find clear IR emission from 35 SNRs with nine additional possible detections. Both studies show that about 30% of the known SNRs exhibit some evidence of IR emission related to the SNRs. The IR spectra of SNRs are regarded to be dominated by thermal dust emission, and any contribution of line emission could not be confirmed clearly. Based on the measured IR fluxes of the SNRs, it is found that young SNRs show stronger emission at 12 and 25 μm while older SNRs do at 60 and 100 μm. This implicates the relation between SNR evolution and dust properties in a SNR. IR emission is compared to radio and X-ray emission, which show a generally good agreement with

both radio and X-ray emission. However, the moderate-to-severe source confusion in or near the Galactic plane makes the detection of IR emission in the Galactic SNRs difficult.

Almost two decades later, the *Spitzer* offers another opportunity to attempt an IR survey of SNRs. Toward the inner Galactic plane ($10^\circ < l < 65^\circ$ and $285^\circ < l < 350^\circ$, $|b| < 1^\circ$), two *Spitzer* surveys, GLIMPSE and MIPSGAL provide improved IR data with higher angular resolution and sensitivity at the four IRAC and two MIPS bands, respectively. In particular, the IRAC bands cover NIR wavelengths that the *IRAS* did not. Reach et al. (2006) present a new IR survey of 95 SNRs in GLIMPS, and as a complement, Pinheiro Gonçalves et al. (2011) search for MIR counterparts of 121 SNRs in MIPSGAL. In the area both *Spitzer* surveys cover, the previous *IRAS* surveys found possible emission from 12 and 14 remnants (Arendt 1989; Saken et al. 1992), with only seven in common each other. On the other hand, 18 and 39 SNRs are identified in the IRAC and MIPS bands, respectively. Using GLIMPSE, diverse origins of IR emission such as ionic/molecular emission, and PAH emission are investigated, and it is found that the remnants interacting with dense ambient medium have most of the shock cooling through molecular or ionic lines. Using MIPSGAL, dust temperatures and masses in the Galactic SNRs are estimated to range from 45 to 70 K and from 0.06 and 2.60 $M_\odot$, and a correlation between total MIR flux (24 and 70 μm) and the 1.4 GHz non-thermal radio flux is identified as found for external galaxies (Helou et al. 1985). However, the detection rate of the IR emission still remains about 30%, albeit the improvement of the data quality, mainly because of inevitable confusion with back/foreground sources and diffuse emission in the line of sight.

In this context, the LMC is the best place to study IR emission from SNRs keeping away from the IR bright Galactic sources. Graham et al. (1987) have discovered IR emission from three out of four LMC SNRs using the *IRAS* data, of which a considerable fraction is due to dust grains heated by collisions with hot plasma. As a survey of the LMC SNRs, Schwering (1989) identify five out of 25 SNRs showing

good quality IR emission as well as eight with possible IR emission. While these early studies are constrained by the limited resolution and sensitivity of the *IRAS*, more detailed studies about LMC SNRs are recently carried out by using *Spitzer* imaging and spectroscopic data (e.g., R. Williams et al. 2006; Borkowski et al. 2006a; B. Williams et al. 2006). However, all these works are about several individual SNRs not about the whole SNRs in the LMC. Hence, it is essential to survey the IR emission of the whole LMC SNRs and to examine their properties statistically. Then, the IR emission from the LMC SNRs can be compared to that from the Galactic SNRs in terms of environmental effects such as different dust composition and metallicity. In this chapter, we present the detection of LMC SNRs in 3 to 70 μm bands using all available data of both *AKARI* and *Spitzer*. We measure IR fluxes of the SNRs detected in any IR bands, and the derived IR properties as well as basic information such size, SN type, and age are summarized in several lists.

2.2 Data

2.2.1 *AKARI* LMC survey

The *AKARI* large-scale survey of the Large Magellanic Cloud (PI: T. Onaka) is one of the three *AKARI* large-scale survey programs. The survey was performed from May 2006 to July 2007 using the on-board instrument Infrared Camera (IRC, Onaka et al. 2007)). IRC has three channels: NIR/MIR-S channels sharing the same $10' \times 10'$ field-of-view (FoV) and MIR-L channel observing the sky about $25'$ away from the NIR/MIR-S FoV. The survey covers about a 10 deg^2 region of the LMC which includes most of the major regions of the LMC in all three channels (Figure 1.1). Note that there is a discrepancy of the observed areas among the bands due to their separate FoVs. So areas near the boundary of the survey were covered in either NIR/MIR-S or MIR-L channel. The imaging observations were carried out in five bands: N3 ($2.7-3.8$ μm), S7 ($5.9-8.4$ μm), S11 ($8.5-13.1$ μm), L15 ($12.6-19.4$ μm), and L24 ($20.3-26.5$ μm). The total integration time is 133 s for an N3 band image

and 147 s for the other bands, and the 10σ detection limits for point sources are 0.086, 0.188, 0.369, 0.811, and 1.744 mJy for N3, S7, S11, L15, and L24, respectively (Ita et al. 2008). We processed the images by using the standard IRC imaging data reduction pipeline (Lorente et al. 2007). In addition to these imaging observations, NIR low-resolution slit-less spectroscopy ($R \sim 20$) was performed for the same 10 deg^2 region in $2 - 5$ μm with the NIR prism spectroscopic mode (NP) of IRC. We have also examined the spectroscopic data of individual SNRs. Since most of them are not visible at this spectral range and even the SNRs showing NIR spectra have difficulties to extract useful information due to confusion from background and/or nearby sources, we will not mention the NP results in this paper.

2.2.2 *Spitzer* LMC data

To search for IR emission from SNRs in the LMC, we examine all available archival data of *Spitzer* at each position of the known SNRs. As mentioned in the previous section, there is the SAGE survey of the LMC ($\sim 7^\circ \times 7^\circ$) using the Infrared Array Camera (IRAC) and the Multiband Imaging Photometer (MIPS) (Meixner et al. 2006). The SAGE survey provides a uniform and unbiased data covering all LMC SNRs at IRAC (3.6, 4.5, 5.8, and 8 μm) and MIPS (24, 70, and 160 μm) bands (Figure 1.1). In addition, there are a number of pointing observations toward the LMC. In particular, the independent survey of MC SNRs (PI: K. Borkowski) conducts deep MIPS 24 μm imaging observations of 33 LMC SNRs as well as several IRAC and MIPS 70 μm imaging toward some SNRs (e.g., Borkowski et al. 2006a; B. Williams et al. 2006). Consequently, we examine deeper *Spitzer* imaging data of LMC SNRs as many as possible and used the SAGE data if other deeper images are not available.

2.3 SNR identification

Although the LMC is scarcely obscured by diffuse emission from the Galactic disk, it is required to disentangle IR emission of a SNR from IR emission of other objects. Since a core-collapse SNR is often embedded in a HII region or a HII complex, it is difficult to confirm IR emission associated with the SNR based on only IR images. Since IR morphology can show some similarities to those seen at other wavelengths, we compare the IR data with other multi-wavelength data such as *ATCA* (*Australia Telescope Compact Array*) 4.8 and 8.6 GHz radio survey data[1] (Dickel et al. 2005), optical images from MCELS[2] (Magellanic Cloud Emission LIne Survey; Smith et al. 2000), and X-ray images from *Chandra* Supernova Remnant Catalog[3]. Figure 1.1 shows the coverage of the SAGE survey with the positions of 45 LMC SNRs on a true color image made of the MCELS data. Almost all SNRs are included in the SAGE, the MCELS, and the *ATCA* survey, and a half of them are observed by *AKARI* or *Chandra*.

2.3.1 SNRs in the *AKARI* LMC survey

Twenty one, previously-known LMC SNRs are included in the *AKARI* LMC survey area. Figure 1.1 shows their positions within the boundary of the area covered in the *AKARI* LMC survey. We examined whether there is IR emission associated with the SNRs. Some SNRs are embedded within IR-bright HII regions or HII complexes such as 30 Doradus, so that careful inspection has been done to discriminate the SNR emission from the surrounding medium by comparing them to the reference data. We have identified nine SNRs in total that have associated IR emission in the NIR and/or MIR bands including three Type Ia SNRs and six core-collapse SNRs (Type II SNRs for simplification, hereafter). Most identified SNRs have distinct shell-like features in the MIR-L bands as well as some related emission in the S11 band. Only

[1] http://www.atnf.csiro.au/research/lmc_ctm

[2] http://www.ctio.noao.edu/mcels/

[3] http://hea-www.harvard.edu/ChandraSNR/

a few SNRs show any emission possibly associated with the SNR in shorter wave bands. SN 1987A is unresolved in all bands, and N158A shows IR emission only from its pulsar wind nebula (PWN). Figures 2.1 and 2.2 show the *AKARI* MIR-band images of the identified nine SNRs, and Figure 2.3 shows the *AKARI* N3 and S7 band images of the two SNRs (N49 and N157B) with the related NIR structures (excluding SN 1987A and N158A).

2.3.2 SNRs in the *Spitzer* data

While only a few SNRs in the *AKARI* LMC survey show NIR emission, it seems that many of SNRs excluded in the *AKARI* survey show IR emission even in NIR bands. When dealing with diffuse IR emission from a SNR that is faint compared to bright point sources, it is difficult to identify IR emission from the SNR, especially at the shorter wavelengths. To avoid confusion by point sources, we apply point source subtraction to all IRAC images using Point Spread Function photometry with an IDL code, *StarFinder* (Diolaiti et al. 2000). If necessary, MIPS 24 μm point-source subtracted images are used for further analysis, too. After carrying out the star subtraction and the comparison with the reference data, we can find 28 out of 45 SNRs showing IR emission at several IR bands, and IR morphologies of 13 SNRs in the *Spitzer* bands are firstly reported. Moreover, although the detections of N11L at 4.5 μm and N103B at 24 μm are previously reported (R. Williams et al. 2006; B. Williams et al. 2009), we can also identify their IR emissions in other *Spitzer* bands.

2.4 IR morphology of SNRs

Most of the identified SNRs are visible in the S11, L15, and L24 bands. In the S11 band, however, the SNR features are confused by the foreground and background emission, which might be dominated by strong PAH 11.3 μm band emission from dust. We subtract this background emission using the S7 band image which is also

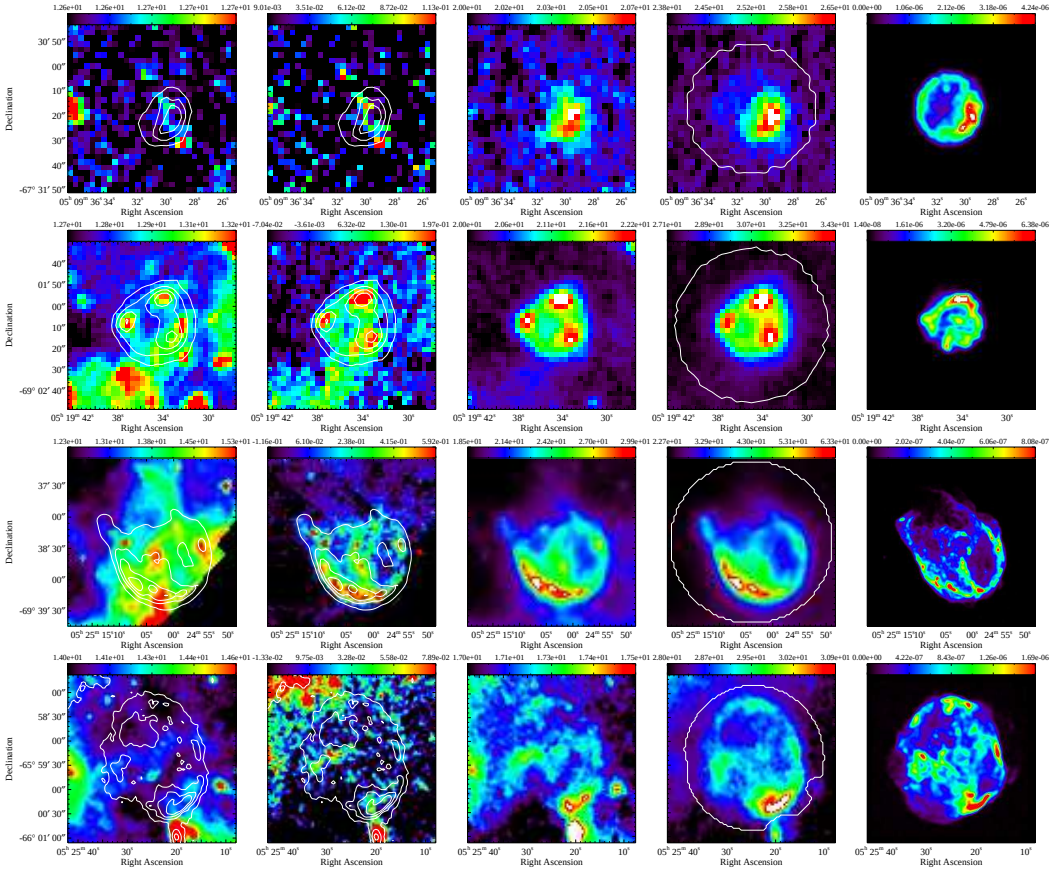

Figure 2.1 From *top* to *bottom*: *AKARI* images of 0509–67.5, 0519–69.0, N132D, and N49B. For each SNR, S11, ‘ S11-S7”, L15, and L24 images are shown together with their *Chandra* X-ray (0.3–2.1 keV) images for comparison. The S11-S7 images are made by subtracting the scaled S7 images from the S11 images (see text for details). The *Chandra* images are from the CSRC. The contours in the S11 and S11-S7 images show the brightness distribution of SNRs in the L24 band, and the contours in the L24 images represent the area used for flux derivations. For N49B, the images are smoothed with a two-pixel Gaussian. The units on the colorbar of the *AKARI* images are MJy sr^{-1}, and the *Chandra* are counts cm^{-2}s^{-1}.

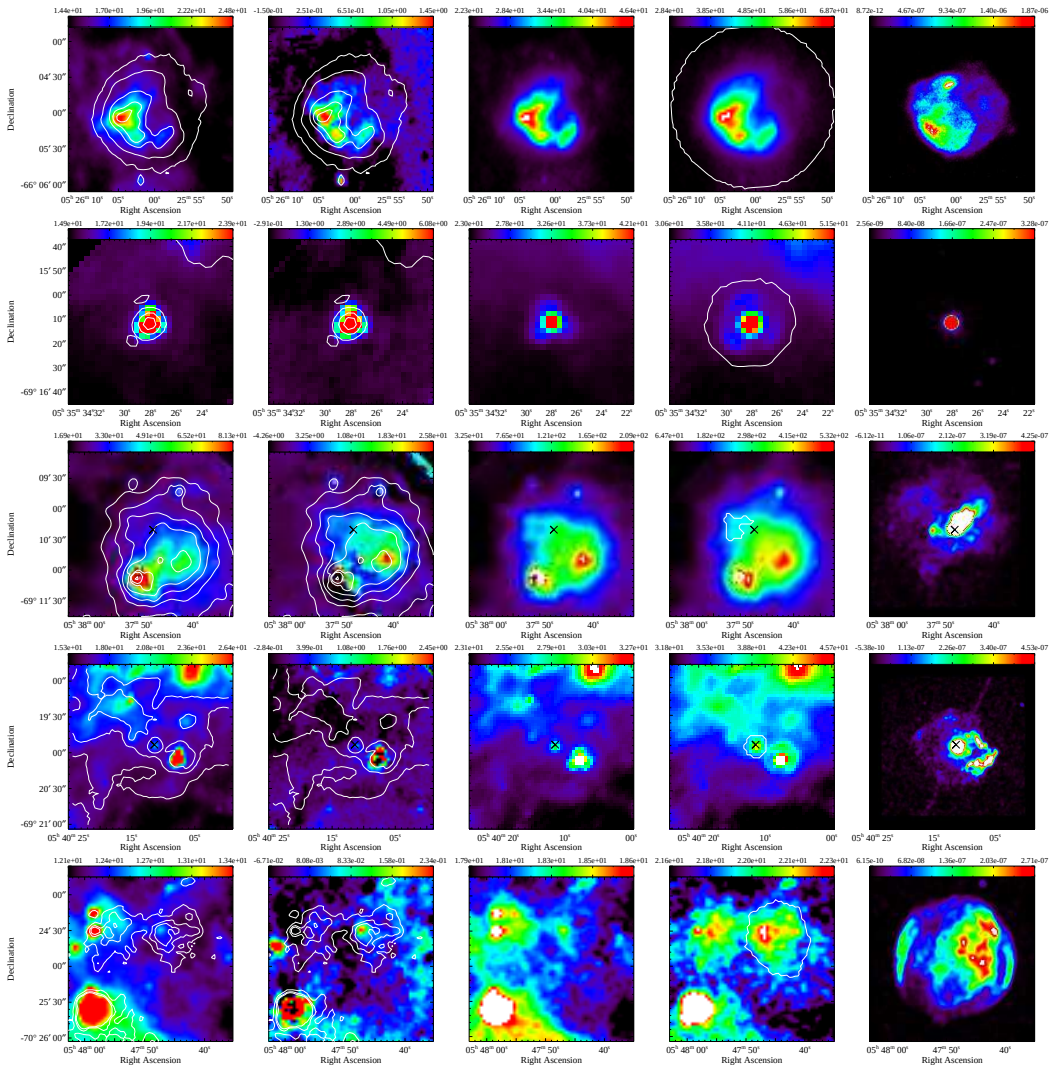

Figure 2.2 From *top* to *bottom*: Same as Figure 2.1 but for N49, SN 1987A, N157B, N158A, and 0548–70.4."×" marks on the third and forth rows represent the positions of pulsars in N157B and N158A, respectively. The images of 0548–70.4 are smoothed with a two-pixel Gaussian. Note that for N157B and 0548–70.4, the flux has been extracted from the limited region due to the confusion (see §2.6.1).

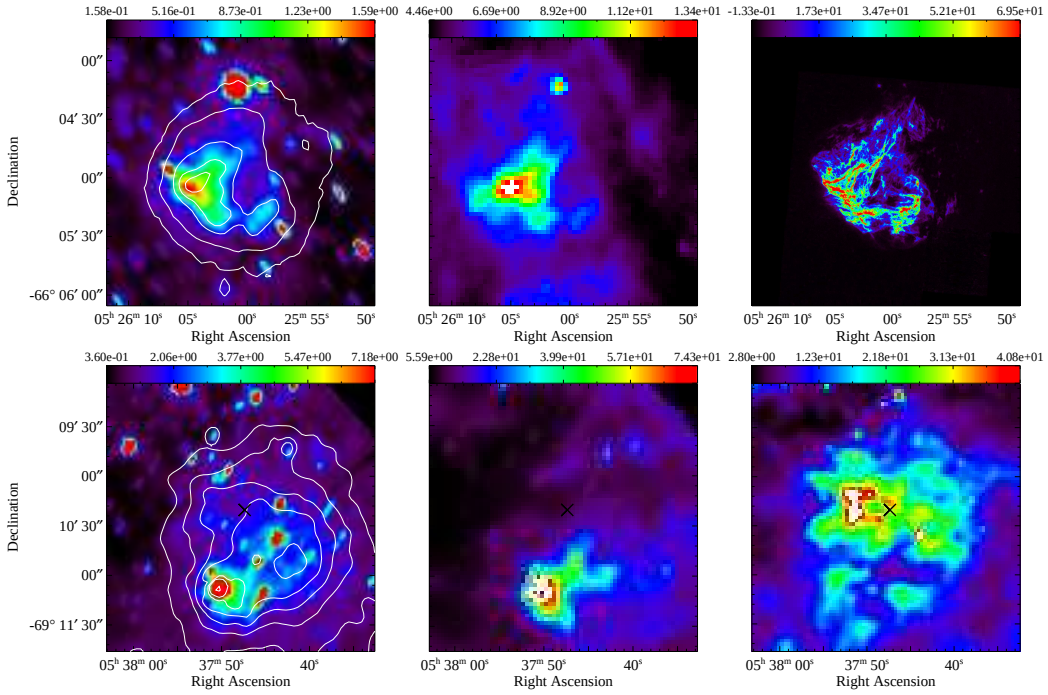

Figure 2.3 N3, S7, and Hα images of N49 (*top*) and N157B (*bottom*). These two and unresolved SNRs (SN 1987A and N158A) are identified in these bands. The contours in the N3 images show the brightness distribution of SNRs in the L24 band. Optical images of N49 and N157B are from the *Hubble Space Telescope (HST)* WFPC2 (Bilikova et al. 2007) and the MCELS survey, respectively.

dominated by the PAH emission from the background. We estimate the mean ratio of S11 to S7 surface brightness of the background emission in each SNR field from a pixel-to-pixel plot of S11 versus S7 brightness and subtract the scaled S7 image from the S11 image, i.e., $S11 - (a \times S7 + b)$, where the scaling factors a and b range $0.4 - 1.4$ and $9 - 14$ MJy sr^{-1}, respectively. The resulting "S11-S7" image shows the SNR features much more clearly than the original S11 image. In Figures 2.1 and 2.2, we show the S11, S11-S7, L15, and L24 images of nine identified SNRs together with their *Chandra* X-ray images.

In all sources detected in the *AKARI* images, we see distinct MIR emission features at the position of SNRs in the S11, L15, and L24 bands. The first five sources (0509–67.5, 0519–69.0, N132D, N49B, and N49) show shell-like structures that are similar to the X-ray SNRs, so that the association of the IR emission with the SNRs is conclusive. The MIR brightness distribution appears to be correlated with the X-ray brightness distribution in general, but in 0519–69.0 and N49, the morphologies are somewhat different, e.g., their peak positions do not coincide with each other. SN 1987A is not resolved in our observation, but the positional coincidence verifies the association. N157B is a Crab-like SNR and there is *no* detectable MIR emission associated with the X-ray/radio PWN[4]. (The very bright emission to the south of the remnant is associated with star-forming regions, not with the SNR.) However, this remnant has bright, extended Hα emission with a strong peak to the east of the PWN (Chu et al. 1992), and the faint "horseshoe-shaped" structure near the center of the field corresponds to the bright optical filaments (see next). Another Crab-like SNR, N158A, shows only IR emission from its PWN. The positional coincidence of the IR emission at the center indicates its association with the PWN, but other emission associated with the X-ray shell cannot be identified. 0548–70.4

[4]If we extrapolate the radio spectrum of the PWN (Lazendic et al. 2000), the expected surface brightness at the radio peak, $(\alpha, \delta) = (05^h37^m45^s, -69°10'11'')$, is estimated to be 2.7 and 3.0 MJy sr^{-1} at 7 and 11 μm, which is greater than the 2 σ detection limit, 0.7 and 1.9 MJy sr^{-1}, in the S7 and S11 bands, respectively. This suggests that the PWN has a spectral break at a wavelength longer than 11 μm.

is located in a rather complicated field with several MIR sources around, but still the MIR emission corresponding to the X-ray bright interior can be clearly seen. The brightness distribution of the MIR emission, however, appears different from the X-rays. The limbs are barely visible only in L24 band. For all SNRs in Figures 2.1 and 2.2, Spitzer obtained 24 μm images (Borkowski et al. 2006a; B. Williams et al. 2006; R. Williams et al. 2006), and our L24 images are consistent with them. The *AKARI* S11 and L15 images are new, and the fact that each SNR shows compatible morphologies in three bands suggests that the MIR emissions in these three bands are of the same origin.

In shorter wavebands, four SNRs are clearly visible: N49, SN 1987A, N157B, and N158A. N132D, the MIR brightest SNR, does not show distinct NIR emission corresponding to the features seen in the MIR bands, which is partly due to its location in the complex area (Tappe et al. 2006). The N3 and S7 images of N49 and N157B are shown in figure 2.3 with their Hα images. N49 has a bright wedge-shaped feature in the eastern part of the remnant and it matches well with the bright optical filaments. N157B is contaminated by the emission from the bright source below the remnant, but still we can identify the features corresponding to the optical filamentary structures including the bright horseshoe-shaped one. The optical counterparts can be distinguished in all IRC bands except the S7. These N3 and S7 images are consistent with the *Spitzer* images which have a bit higher resolution (R. Williams et al. 2006). We briefly describe the characteristics of each source in Appendix.

IR morphologies of all 28 SNRs in the *Spitzer* bands are shown in Figure 2.4 to A.13. All nine SNRs detected in the *AKARI* bands are included (Figure 2.4 and 2.5). Most of the detected SNRs show shell-like structures in the MIPS bands. In particular, all of nine SNRs identified only in the MIPS bands clearly manifest shell-like morphologies which correspond well to their X-ray morphologies (Figure 2.4). In the IRAC bands, we examine both the original and the star-subtracted images to avoid severe confusion by point sources (Figure 2.6). Many of SNRs detected in the

IRAC bands have good spatial correlations with their optical morphologies. Some SNRs show complete shell structures whereas others do only filamentary or patchy emissions. In addition, we could detect several knotty emissions in N103B, which are also seen in Hα and X-ray, too (Figure A.6 and see §A.9). More detailed description of each SNR is in Appendix.

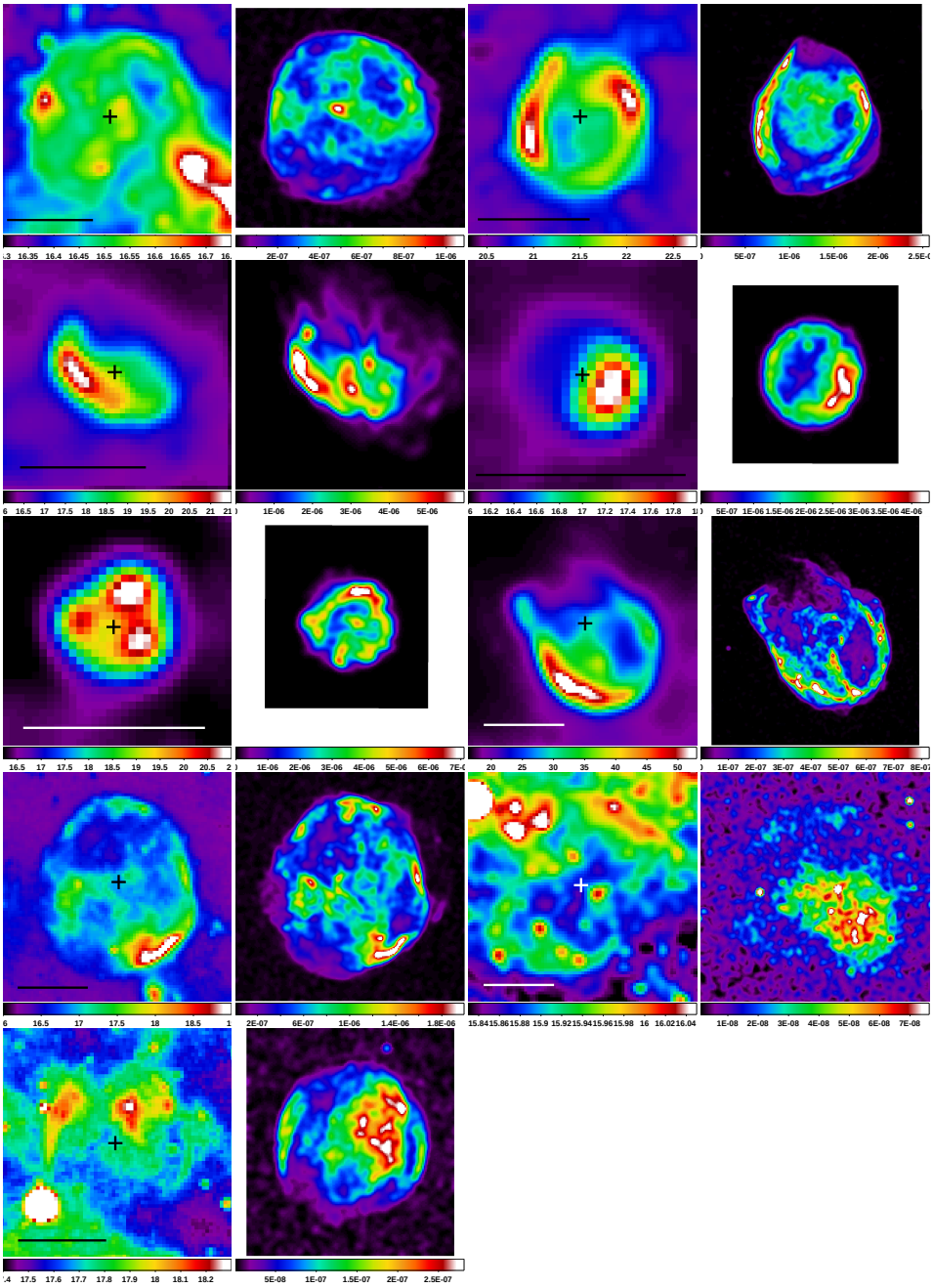

Figure 2.4 *Spitzer* MIPS 24 μm images of nine SNRs only visible in the MIPS bands. Their *Chandra* $0.3-10$ keV images are shown for comparison. The first and third columns are the MIPS 24 μm images, and the second and fourth columns are the *Chandra* images. *Top row*: SNR 0453–68.5 and DEM L71. *Second row*: N23 and SNR 0509–67.5. *Third row*: SNR 0519–69.0 and N132D. *Fourth row*: N49B and DEM L238. *Bottom row*: SNR 0548–70.4. In the 24 μm images, the cross marks the center position of each SNR listed in Table 2.1, and the scale bar corresponds $1'$ (i.e., 15 pc at 50 kpc). The units on the colorbar are MJy sr^{-1} for the MIPS images and counts cm^{-2} s^{-1} for the *Chandra* images. North is up, and east is to the left.

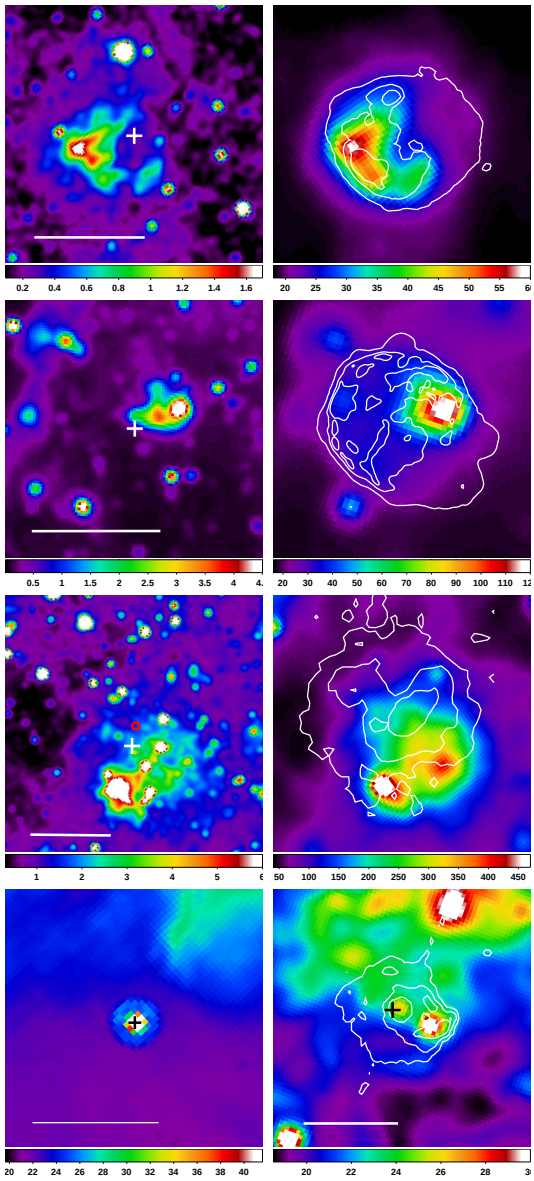

Figure 2.5 Five SNRs previously detected in all *Spitzer* bands; N49 in *top row*, N63A in *second row*, N157B in *third row*, and SNR 1987A (observed on 26 Aug. 2007) & N158A in *bottom row*. For N49, N63A, and N157B, 3.6 and 24 μm images are shown while only 24 μm images are shown for the two unresolved SNRs (SNR 1987A and the PWN of N158A). For comparison, contours from *Chandra* wide-band ($0.3 - 10$ keV) data are overlaid in the 24 μm images except for SN 1987A. The cross marks the central position of each SNR listed in Table 2.1, and the scale bar corresponds $1'$. The circle in the 3.6 μm image of N157B denotes the position of the PWN. All images are smoothed with a three-pixel Gaussian. The units on the colorbar are MJy sr^{-1}. North is up, and east is to the left.

2.5 General information of SNRs in the LMC

We firstly summarize general properties of all SNRs in the LMC such as their position, SN type, and SNR age in Table 2.1. We refer to Desai et al. (2010) for names, positions and sizes of the SNRs. According to previous studies, 10 and 20 SNRs are known to be Type Ia and core-collapse SNRs, respectively, and SN types of the rest are still uncertain. The youngest SNR is SN 1987A, and ages of the oldest SNRs can reach hundreds of thousands (e.g., SNR 0450–70.9, N86, and DEM L72). We measure 4.8 GHz radio fluxes of 42 SNRs included in the *ATCA* survey and list them for further analysis, too. The size of a source aperture is defined as two times larger than the size of each SNR in Table 2.1, and the background intensity is estimated from an annulus of each source aperture. The statistical errors (1 σ) of the 4.8 GHz fluxes are less than 5%. The results of the *AKARI* and the *Spitzer* detection are also summarized; 19 SNRs are seen in the IRAC bands while all detected SNRs show emission features in the MIPS 24 μm band. All SNRs detected in the *AKARI* survey are seen in the *Spitzer* bands.

Table 2.1. SNRs in the Large Magellanic Cloud

SNR B1950 (1)	Common name (2)	R.A. (J2000) (3)	Dec. (J2000) (4)	Size (arcmin) (5)	4.8 GHz (mJy) (6)	SN type (7)	Age (yr) (8)	*AKARI* detection (9)	*Spitzer* detection (10)	Ref. (11)
0448–67.1	J0448–6659	04:48:25	-67:00:12	4.5×3.4	...	...	...	N	U	—
0449–69.4	J0449–6921	04:49:22	-69:20:25	2.0	56	...	...	N	U	—
0450–70.9	0450–709	04:50:30	-70:50:05	7.7×5.3	380	...	≥ 45000	N	I1 – M2	1
0453–66.9	SNR in N4	04:53:14	-66:55:42	4.3	102	...	...	N	I1 – M2	—
0453–68.5	0453–68.5	04:53:38	-68:29:27	2.0	138	II (C)	~ 13000	N	M1 – M2	2
0454–67.2	SNR in N9	04:54:33	-67:13:00	2.8×2.2	39	Ia	~ 30000	N	U	3
0454–66.5	N11L	04:54:50	-66:25:37	1.4×1.0	65	II	$7000 - 15000$	N	I1 – I3, M1 – M2	4
0455–68.7	N86	04:55:44	-68:38:23	6.5×3.5	167	...	$20000 - 86000$	N	I1 – M2	4
0500–70.2	N186D	04:59:56	-70:07:58	2.6×2.3	62	II	~ 11000	N	U	5
0505–67.9	DEM L71	05:05:42	-67:52:39	1.5×1.2	9	Ia	~ 4360	N	M1 – M2	2
0506–68.0	N23	05:05:55	-68:01:47	1.2×0.8	131	II	~ 4600	N	M1 – M2	2
0506–65.8	DEM L72	05:06:06	-65:41:08	6.4×4.7	...	...	~ 100000	N	I4 – M2	6
0509–68.7	N103B	05:08:59	-68:43:35	0.50	238	Ia	~ 1000	N	I1 – M2	7
0509–67.5	0509–675	05:09:31	-67:31:17	0.56	38	Ia	~ 410	S11 – L24	M1 – M2	7
0513–69.2	0513–692	05:13:14	-69:12:20	4.5×3.2	178	...	...	U	U	—
0519-69.7	SNR in N120	05:18:44	-69:39:09	1.6×1.3	181	II	...	N	U	8
0519–69.0	0519–690	05:19:35	-69:02:09	0.55	55	Ia	~ 610	S11 – L24	M1 – M2	7
0520–69.4	0520–694	05:19:44	-69:26:08	2.4×2.1	99	...	...	U	U	—
0522-65.8	J0521–6542	05:21:39	-65:43:10	3.0×2.4	...	...	...	N	U	—
0523–67.9	SNR in N44	05:23:07	-67:53:12	3.5	126	II	~ 18000	U	U	5, 9

Table 2.1 (cont'd)

SNR B1950 (1)	Common name (2)	R.A. (J2000) (3)	Dec. (J2000) (4)	Size (arcmin) (5)	4.8 GHz (mJy) (6)	SN type (7)	Age (yr) (8)	*AKARI* detection (9)	*Spitzer* detection (10)	Ref. (11)
0524–66.4	DEM L175A	05:24:20	-66:24:23	4.1×2.8	98	II	...	U	U	8
0525–69.6	N132D	05:25:04	-69:38:20	2.0×1.5	1737	II (O)	~ 3150	S11 – L24	M1 – M2	2
0525-66.0	N49B	05:25:25	-65:59:19	2.5×2.3	263	II	~ 10000	S11 – L24	M1 – M2	2
0525–66.1	N49	05:26:00	-66:04:57	1.5×1.3	669	II	~ 6600	N3 – L24	I1 – M2	9
0528–69.2	0528–692	05:27:39	-69:12:04	2.7×2.0	87	II	...	U	U	8
0527–65.8	DEM L204	05:27:54	-65:49:38	4.5	88	...	...	U	U	—
0531–70.2	J0530–7008	05:30:44	-70:07:10	3.5×2.8	96	...	...	N	U	—
0532–71.0	SNR in N206	05:31:56	-71:00:19	3.0	214	II (C)	~ 25000	N	I1 – M1	2, 10
0532–67.5	0532–675	05:32:30	-67:31:33	4.5	207	...	...	N	U	—
0534–69.9	0534–699	05:34:02	-69:55:03	1.7×1.4	74	Ia	~ 10000	U	U	2
0534–70.5	DEM L238	05:34:18	-70:33:26	2.9×2.5	79	Ia	$10000 - 15000$	U	M1	11
0535–69.3	SNR 1987A	05:35:28	-69:16:11	< 0.1	89	IIpec	24	N3 – L24	I1 – M2	—
0535–66.0	N63A	05:35:44	-66:02:14	1.4×1.2	657	II	$2000 - 5000$	N	I1 – M2	9
0536–69.3	Honeycomb	05:35:48	-69:18:04	1.4×0.6	108	...	...	U	U	—
0536–67.6	DEM L241	05:36:03	-67:35:04	2.4	139	II (C)	...	N	I1 – M2	12
0536–70.6	DEM L249	05:36:07	-70:38:37	3.0×2.0	64	Ia	$10000 - 15000$	N	I1 – M2	11
0538–66.5	DEM L256	05:37:30	-66:27:47	3.6×2.8	67	...	≤ 50000	N	I1 – M2	6
0538–69.1	N157B	05:37:48	-69:10:35	1.7×1.2	1923	II (C)	~ 5000	N3, S11 – L24	I1 – M1	9
0540–69.7	SNR in N159	05:39:59	-69:44:02	1.8	972	II	≥ 18000	U	I1 – M2	13
0540–69.3	N158A	05:40:12	-69:19:55	1.3×1.1	474	IIP (C)	$760 - 1660$	N3 – L24	I1 – M2	14, 15

Table 2.1 (cont'd)

SNR B1950 (1)	Common name (2)	R.A. (J2000) (3)	Dec. (J2000) (4)	Size (arcmin) (5)	4.8 GHz (mJy) (6)	SN type (7)	Age (yr) (8)	*AKARI* detection (9)	*Spitzer* detection (10)	Ref. (11)
0543–68.9	DEM L299	05:43:10	-68:58:49	5.8×4.0	293	...	...	N	I1– M2	—
0547–69.7	DEM L316B	05:46:59	-69:42:50	3.4×2.8	289	II	≥ 42000	U	I1 – I3, M1 – M2	16, 17
0547–69.7	DEM L316A	05:47:22	-69:41:26	2.0	143	Ia	$27000 - 39000$	U	I1 – I3, M1 – M2	16, 17
0548–70.4	0548–704	05:47:49	-70:24:54	2.0×1.8	43	Ia	~ 7100	S11 – L24	M1 – M2	2
0551–68.4	J0550-6823	05:50:30	-68:23:22	5.2×3.5	316	II (O)	...	N	U	18

Note. — Col. (1)–(5): SNR names, alternative names, positions, and angular sizes from Desai et al. (2010). Angular sizes are mostly in optical, but some are in X-ray/IR. Col. (6): 4.8 GHz radio fluxes of SNRs measured by using ATCA data (Dickel et al. 2005). The flux measurement is described in text. Col. (7): SNR type from literatures. Except Crab-like SNRs marked as "II(C)", Type II SNRs are shell type SNRs of core-collapse SN origin. Oxygen-rich SNRs are marked as "II (O)". Col. (8): SNR age from literatures. Col. (9)–(10): Detection status by *AKARI* and *Spitzer*. If IR emission is detected from a SNR, the detected filter name is given (*AKARI*: N3, S7, S11, L15, and L24, *Spitzer*: I1, I2, I3, I4, M1, and M2). Otherwise, U: undetected and N: no data. Col. (11) References for SNR ages and types; [1] R. Williams et al. (2004); [2] Lopez et al. (2011); [3] Seward et al. (2006); [4] R. Williams et al. (1999); [5] Jaskot et al. (2011); [6] Klimek et al. (2010); [7] Ages estimated from light echos by Rest et al. (2005); [8] Chu & Kennicutt (1988); [9] R. Williams et al. (2006); [10] R. Williams et al. (2005); [11] Borkowski et al. (2006b); [12] Bamba et al. (2006); [13] Seward et al. (2010); [14] Park et al. (2010); [15] B. Williams et al. (2008); [16] R. Williams & Chu (2005); [17] Nishiuchi et al. (2001); [18] Bozzetto et al. (2011)

2.6 Flux measurement

2.6.1 *AKARI* flux

For the identified SNRs, we derive their fluxes in each band (Table 2.2). The S11 fluxes are derived from the S11-S7 images except N49, SN 1987A, and N158A that show appreciable emission in the S7 band. The areas used for flux estimation are marked in the L24 images of figure 2.1 and 2.2. The fluxes are extracted from the entire SNR area except four SNRs: N132D, N157B, N158A, and 0548–70.4. N132D is incompletely covered in the NIR and MIR-S bands so that we could obtain the total fluxes only in the MIR-L. The fraction of the uncovered area, however, is small, so that we estimate the total S11 flux by first deriving the ratio of the S11 to L15 flux from the shared area and then by multiplying it to the total L15 flux. N157B is confused by the southern star-forming regions, so we extract only the fluxes from the horseshoe-shape region in order to avoid any contamination from other sources. N158A show the IR emission only from its PWN, and other extended emission could not be distinguished by nearby bright emission. 0548–70.4 is located in a complicated area, and the background stars are located near the eastern rim.

Our measured IR fluxes are uncertain by $10 - 30\%$ ($1\ \sigma$) considering the uncertainties in measurements, background estimation, and the absolute calibration. For most sources, the error in the absolute calibration dominates, which is about 10% (see Koo et al. 2007). The IRC fluxes are the fluxes at reference wavelengths assuming a flux distribution of $f_\lambda \propto \lambda^{-1}$ (Lorente et al. 2007). We do not apply the color-correction since the origin of the IR emission can differ from source to source. All flux values we employ for further analysis are not the color-corrected ones except in § 3.3.2 where we derive the dust properties. The derived IRC fluxes are mostly consistent with the published *Spitzer* fluxes (e.g., Borkowski et al. 2006a). For SN 1987A, Dwek et al. (2008) showed that its flux at 24 μm was ~ 30 mJy on February 4, 2004 (day 6190) and increased by a factor of 2 after 947 days (day 7137). The *AKARI* spectrum was obtained from October 31 to November 4, 2006 (day

7190 − 7194), and the derived IRC fluxes are similar to those of the latest spectra with the *Spitzer* Infrared Spectrograph (IRS).

2.6.2 *Spitzer* flux

For the newly identified SNRs, their fluxes in each band are estimated by using star-subtracted IRAC and (original) MIPS images. IR emissions clearly associated with SNRs are determined for the flux measurement, and the extracted SNR regions are marked in Figure 2.6. Background subtraction is coherently applied by using the annulus of the extracted region with 15″ in width. As SNRs are embedded in bright H II regions or H II complexes, for example, SNR in N159, it is problematic to define their own emissions. Or, specific features in SNRs appear in several bands while other features are distinct in few bands. In those cases, fluxes of restricted regions are measured. The calculated fluxes and the flux information of previously known SNRs are accumulated in Table 2.3.

Table 2.2 AKARI IRC fluxes of LMC SNRs

SNR	*N3* (mJy)	*S7* (mJy)	*S11* (mJy)	*L15* (mJy)	*L24* (mJy)
0509–67.5	<0.1	<0.2	0.3 ± 0.1	3.9 ± 0.4	20 ± 2
0519–69.0	<0.6	<1.3	2.5 ± 0.3	33 ± 3	110 ± 11
N132D[a]	...	...	60 ± 6	980 ± 98	3370 ± 340
N49B	<0.6	<1.6	3.5 ± 0.4	55 ± 5	360 ± 36
N49	36 ± 4	280 ± 28	330 ± 33	870 ± 87	1930 ± 193
SN 1987A	1.5 ± 0.1	4.9 ± 0.5	32 ± 3	43 ± 4	65 ± 7
N157B[b]	4.3 ± 0.4	<1.9	39 ± 4	280 ± 28	730 ± 73
N158A[b]	1.6 ± 0.2	3.4 ± 0.7	4.4 ± 0.6	7.1 ± 0.8	16.1 ± 2.0
0548–70.4[b]	<0.2	<0.6	0.6 ± 0.2	10 ± 1	24 ± 2

[a]N132D has not been fully covered in the *S11* band. We derive the *S11* flux by first deriving the ratio of the *S11* to *L15* flux from the shared area and then by multiplying it to the total *L15* flux.

[b]The fluxes of N157B, N158A, and 0548–70.4 are not from the entire SNRs but from limited areas (see Figure 2.2).

Note. — Fluxes at reference wavelengths of each band are given. The reference wavelengths are 3.2, 7.0, 11.0, 15.0, and 24.0 μm for the *N3*, *S7*, *S11*, *L15*, and *L24*, respectively. *S11* fluxes are from *S11*-*S7* images except N49 and SN 1987A. Fluxes are not color-corrected. Flux errors are 1 σ, and limits are 3 σ.

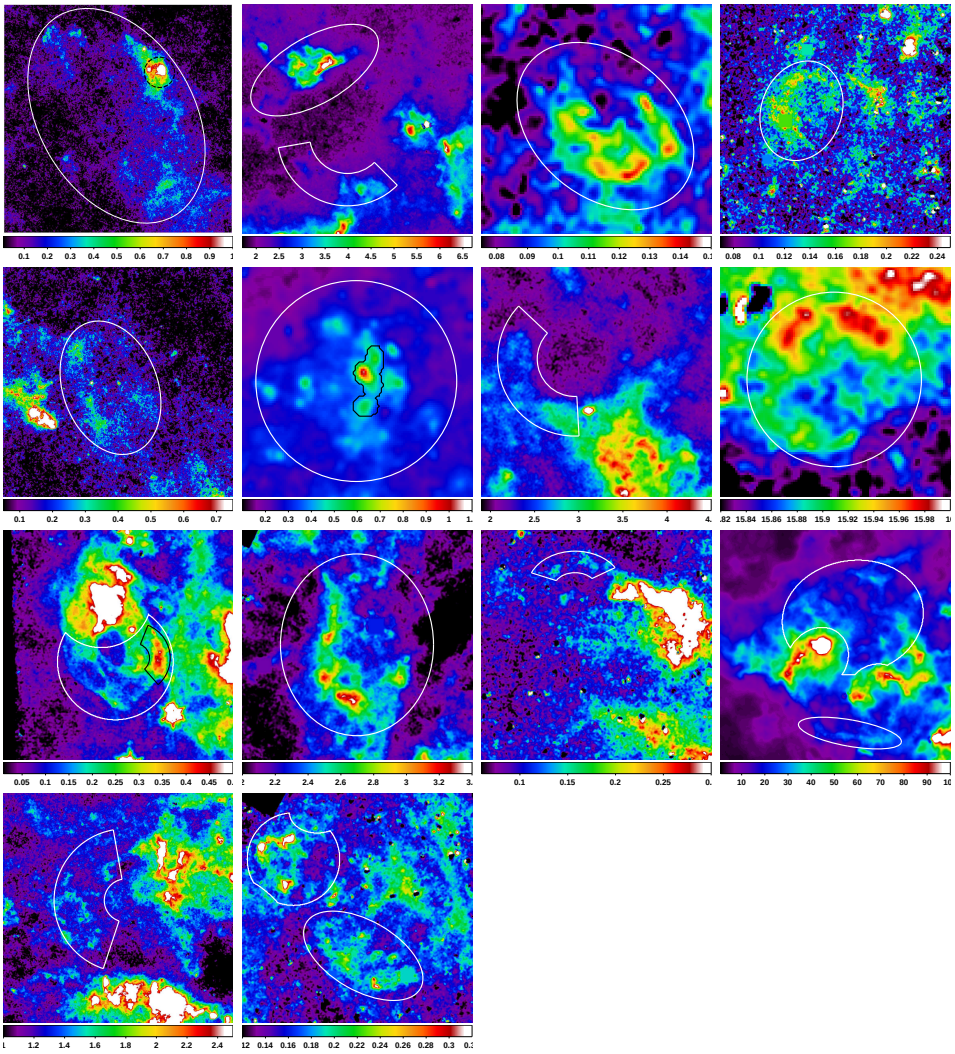

Figure 2.6 Representative *Spitzer* images of 15 SNRs of which IR fluxes are measured in this paper. *Top row*: SNR 0450–70.9 (8.0 μm), SNR in N4 (8.0 μm), N11L (4.5 μm), and N86 (4.5 μm). *Second row*: DEM L72 (8.0 μm), N103B (4.5 μm), SNR in N206 (8.0 μm), and DEM L238 (24 μm). *Third row*: DEM L241 (4.5 μm), DEM L249 (8.0 μm), DEM L256 (3.6 μm), and SNR in N159 (8.0 μm). *Bottom row*: DEM L299 (5.8 μm) and DEM L316A/B (4.5 μm). All images are star-subtracted (see text). Regions where fluxes are extracted are marked in each figure (*white*). Specific areas of which fluxes are separately measured are denoted in N103B and DEM L241 (*black*). In SNR 0450–70.9, the northwestern region excluded for the flux estimation is also designated (*black dashed circle*). The units on the colorbar are MJy sr^{-1}. For all images, north is up, and east is to the left.

Table 2.3. *Spitzer* fluxes of LMC SNRs

SNR	I1 (mJy)	I2 (mJy)	I3 (mJy)	I4 (mJy)	M1 (mJy)	M2 (mJy)	Region	Area (arcmin^2)	Reference
0450–70.9	28.2±0.31	27.1±0.35	149±1.4	367±1.4	249±4.6	5057±63	whole	76.56	this work
SNR in N4 NE	18±0.1	12±0.1	102±0.4	276±0.5	307±1.6	5316±42	northeastern region	6.25	this work
SNR in N4 S	3.6±0.07	2.3±0.09	22±0.3	50±0.6	39±0.9	578±32	southern shell	3.22	this work
0453–68.5	...	...	...	...	37.5±4[a]	...	whole	4.71	this work
	...	...	...	...	13±1.3	250±50	northern shell	...	1
N11L	1.14 ± 0.04	1.78 ± 0.04	4.10 ± 0.16	≤ 3.4	13 ± 0.75	132 ± 21	whole	1.68	this work
	...	1.5	...	< 8.5	...	...	whole	0.73	2
N86	7.5 ± 0.18	7.2 ± 0.09	24 ± 0.31	17.7 ± 0.47	37 ± 1.35	258 ± 25	northeastern region	3.98	this work
DEM L71	...	...	...	< 1.06	88.2±8.8	455±94	whole shell	...	3
N23	...	...	...	...	147±15[a]	...	whole	1.69	this work
	...	...	...	...	100±10	240±50	southeastern shell	...	1
DEM L72	≤ 3.2	≤ 2.9	≤ 31	74.9±0.69	48.0±2.2	1036±30	whole	19.48	this work
N103B	≤ 7.5	≤ 4.5	≤ 41	≤ 115	505±2	549±28	whole	0.78	this work
N103B kn	0.8±0.02	0.9±0.01	3.4±0.06	10±0.2	— [b]	— [b]	knots	0.04	this work
0509–67.5[c]	...	...	...	< 0.2	16.7±1.7	< 32.7	whole	...	3
0519–69.0[c]	...	...	...	< 0.9	92.0±9.2	< 121	whole	...	3
N132D NW[c]	...	...	...	...	730±73	430±96	northwestern shell	...	1
N132D S[c]	...	...	...	...	1000±100	770±170	southern shell	...	1
N49B[c]	...	...	...	...	275±27[a]	...	whole	7.43	this work
	...	...	...	...	43±4.3	395±79	northern shell	...	1
N49[c]	32	41	130	180	1500	10200	whole	1.11	2
SNR in N206	3.35 ± 0.04	2.42 ± 0.05	16.1 ± 0.19	30 ± 0.3	24.5 ± 1.3	≤ 134	eastern shell	1.64	this work
DEM L238	≤ 1.04	≤ 0.92	≤ 0.49	≤ 0.48	10±0.4	≤ 77	whole	7.56	this work
SNR 1987A[c]	...	...	2.44±0.19	7.48±0.19	29.8±1.7	...	whole	aperture[d]	4
N63A	37	32	130	300	2300	7700	whole	1.31	2
DEM L241	10.5±0.17	15±0.14	≤ 2.3	≤ 6.1	293±15	≤ 1253	whole	3.84	this work
DEM L241 W	3.5±0.06	3.7±0.04	9.6±0.3	26±0.8	61±4	665±87	western shell	0.5	this work

Table 2.3 (cont'd)

SNR	I1 (mJy)	I2 (mJy)	I3 (mJy)	I4 (mJy)	M1 (mJy)	M2 (mJy)	Region	Area (arcmin^2)	Reference
DEM L249	6.1 ± 0.07	7.2 ± 0.06	47 ± 0.2	94 ± 0.39	54 ± 1.1	798±40	whole	6.63	this work
DEM L256	0.40±0.03	0.39±0.03	1.30±0.12	1.27±0.16	5.1±1.6	108±14	northern shell	0.57	this work
N157B[c]	62	87	< 140	< 210	...	...	w/o southern clouds	1.20	2
N158A[c]	1.77±0.23	2.19±0.27	3.61±0.46	5.10±0.74	13.19±3.95	< 366	PWN	0.03	5
SNR in N159 N	128±1.3	149±1.2	371±7	918±19	8078±551	10145±2858	northern lobe	3.25	this work
SNR in N159 S	22±0.76	26±0.55	76.9±1.8	222±5.1	2464±133	4717±490	southern shell	0.66	this work
DEM L299	6.67 ± 0.11	7.99 ± 0.12	17.7 ± 0.4	97 ± 1	94 ± 3	1475 ± 69	eastern shell	7.52	this work
DEM L316B	1.9±0.05	5.0±0.04	14.6±0.2	≤ 2.4	24±1.4	597±37	southern shell	3.34	this work
DEM L316A	2.8±0.04	6.1±0.06	23±0.19	≤ 14	31±1	445±26	whole	2.88	this work
0548–70.5[c]	...	...	...	...	42±4[a]	...	whole	3.43	this work
	...	...	...	< 3.82	2.63±0.30	19.9±4.7	northeastern shell	...	3

Note. — Infrared fluxes of detected SNRs in the *Spitzer* bands. The uncertainty is taking only statistical uncertainties of background fluctuation. Upperlimits are 3 σ. SNRs with a bold name are also observed by *AKARI* (Table 2.2). When necessary information does not exist in references, we mark it as ellipsis. References for adopting fluxes; [1] B. Williams et al. (2006): Fluxes only measured from the confined regions that are clearly bright at both 24 and 70 μm. [2] R. Williams et al. (2006): Area on the sky (of SNR) for which flux densities are estimated and descriptions for some cases (N49, N63A, and N157B) are given in Table 2 of the reference. [3] Borkowski et al. (2006a) [4] Bouchet et al. (2006): The IRAC fluxes and the MIPS flux are observed on 6487 and 6184 days after the SN explosion, respectively. [5] B. Williams et al. (2008)

[a]24 μm fluxes from the whole SNRs are newly measured by this work. Their 24 and 70 μm fluxes from the literatures are measured from the regions where both band fluxes can be clearly extracted. For Figure 3.7, 3.11, and 3.12, these 24 μm fluxes from the whole SNRs are used.

[b]Knots are no longer distinguishable at the MIPS bands.

[c]IR fluxes of these SNRs are measured by using the *AKARI* data, too (Figure 2.2)

[d]Radii used for aperture photometry were 4.8″, 6.0″, and 14.7″ at 5.8, 8.0, and 24 μm, respectively (Bouchet et al. 2006).

Bibliography

Arendt, R. G. 1989, ApJS, 70, 181

Bamba, A., Yamazaki, R., Yoshida, T., Terasawa, T., & Koyama, K. 2005, ApJ, 621, 793

Bilikova, J., Williams, R. N. M., Chu, Y.-H., Gruendl, R. A., & Lundgren, B. F. 2007, AJ, 134, 2308

Borkowski, K. J., Williams, B. J., Reynolds, S. P., et al. 2006, ApJ, 642, L141

Borkowski, K. J., Hendrick, S. P., & Reynolds, S. P. 2006, ApJ, 652, 1259

Bouchet, P., Dwek, E., Danziger, J., et al. 2006, ApJ, 650, 212

Bozzetto, L. M., Filipović, M. D., Crawford, E. J., et al. 2011, arXiv:1109.3945

Chu, Y.-H., Kennicutt, R. C., Jr., Schommer, R. A., & Laff, J. 1992, AJ, 103, 1545

Chu, Y.-H., & Kennicutt, R. C., Jr. 1988, AJ, 96, 1874

Desai, K. M., Chu, Y.-H., Gruendl, R. A., et al. 2010, AJ, 140, 584

Dickel, J., McIntyre, V., Gruendl, R., & Milne, D. 2005, AJ, 129, 790

Diolaiti, E., Bendinelli, O., Bonaccini, D., et al. 2000, Proc. SPIE, 4007, 879

Dwek, E., Arendt, R. G., Bouchet, P., et al. 2008, ApJ, 676, 1029

Graham, J. R., Evans, A., Albinson, J. S., et al. 1987, ApJ, 319, 126

Helou, G., Soifer, B. T., & Rowan-Robinson, M. 1985, ApJ, 298, L7

Ita, Y., Onaka, T., Kato, D., et al. 2008, PASJ, 60S, 435

Jaskot, A. E., Strickland, D. K., Oey, M. S., et al. 2011, ApJ, 729, 28

Klimek, M. D., Points, S. D., Smith, R. C., Shelton, R. L., & Williams, R. 2010, ApJ, 725, 2281

Koo, B.-C., Lee, H.-G., Moon, D.-S., et al. 2007, PASJ, 59S, 455

Lazendic, J. S., Dickel, J. R., Haynes, R. F., Jones, P. A., & White, G. L. 2000, ApJ, 540, 808

Lopez, L. A., Ramirez-Ruiz, E., Huppenkothen, D., Badenes, C., & Pooley, D. A. 2011, ApJ, 732, 114

Lorente, R., Onaka, T., Ita, Y., Ohyama, Y., & Pearson, C. 2007, AKARI IRC Data User's Manual ver. 1.3

Meixner, M., Gordon, K. D., Indebetouw, R., et al. 2006, AJ, 132, 2268

Nishiuchi, M., Yokogawa, J., Koyama, K., & Hughes, J. P. 2001, PASJ, 53, 99

Onaka, T., Matsuhara, H., Wada, T., et al. 2007, PASJ, 59S, 401

Park, S., Hughes, J. P., Slane, P. O., et al. 2010, ApJ, 710, 948

Pinheiro Gonçalves, D., Noriega-Crespo, A., Paladini, R., Martin, P. G., & Carey, S. J. 2011, AJ, 142, 47

Reach, W. T., Rho, J., Tappe, A., et al. 2006, AJ, 131, 1479

Rest, A., Suntzeff, N. B., Olsen, K., et al. 2005, Nature, 438, 1132

Saken, J. M., Fesen, R. A., & Shull, J. M. 1992, ApJS, 81, 715

Schwering, P. B. W. 1989, A&AS, 79, 105

Seward, F. D., Williams, R. M., Chu, Y.-H., et al. 2010, AJ, 140, 177

Seward, F. D., Williams, R. M., Chu, Y.-H., et al. 2006, ApJ, 640, 327

Smith, C., Leiton, R., & Pizarro, S. 2000, ASPC, 221, 83

Tappe, A., Rho, J., & Reach, W. T. 2006, ApJ, 653, 267

Williams, B. J., Borkowski, K. J., Reynolds, S. P., et al. 2009, Bulletin of the American Astronomical Society, 41, #488.06

Williams, B. J., Borkowski, K. J., Reynolds, S. P., et al. 2008, ApJ, 687, 1054

Williams, B. J., Borkowski, K. J., Reynolds, S. P., et al. 2006, ApJ, 652, 33

Williams, R. M., Chu, Y.-H., & Gruendl, R. 2006, AJ, 132, 1877

Williams, R. M., Chu, Y.-H., Dickel, J. R., et al. 2005, ApJ, 628, 704

Williams, R. M. & Chu, Y.-H. 2005, ApJ, 635, 1077

Williams, R. M., Chu, Y.-H., Dickel, J., et al. 2004, ApJ, 613, 948

Williams, R. M., Chu, Y.-H., Dickel, J., et al. 1999, ApJ, 514, 798

Chapter 3

Statistical studies of IR SNRs in the LMC

3.1 IR properties of SNRs

3.1.1 IR fluxes

We compare the *AKARI* L15 and L24 fluxes of the identified SNRs in Figure 3.1. There is a tight correlation between the two fluxes as expected, but the *L15/L24* flux ratio ranges from 0.15 up to 0.7. The brightest SNRs are N132D and N49. These two SNRs are interacting with their ambient molecular clouds (Banas et al. 1997), and the bright IR emission may be related to the interaction. Type Ia SNRs are the faintest among the identified SNRs with (*L24*, *L15*) = (20, 3.9) to (110, 33) (mJy), while Type II SNRs are located in the upper right part where (*L24*, *L15*) = (65, 43) to (3370, 980) (mJy).

We compare the *Spitzer* 24 μm and 70 μm fluxes of 28 SNRs (Figure 3.2, $left$). Regardless of their IR emitting mechanisms, a good correlation between those fluxes can be seen. Even after normalizing the IR fluxes to radio fluxes, the correlation still remains good as reported for Galactic SNRs (Pinheiro Gonçalves et al. 2011). It seems that there is rough tendency that Type Ia SNRs such as SNR 0509–67.5 or SNR 0548–70.4 have low flux densities while core-collapse SNRs, especially, SNRs interacting with nearby molecular clouds (e.g., N49) or SNRs embedded in H II regions

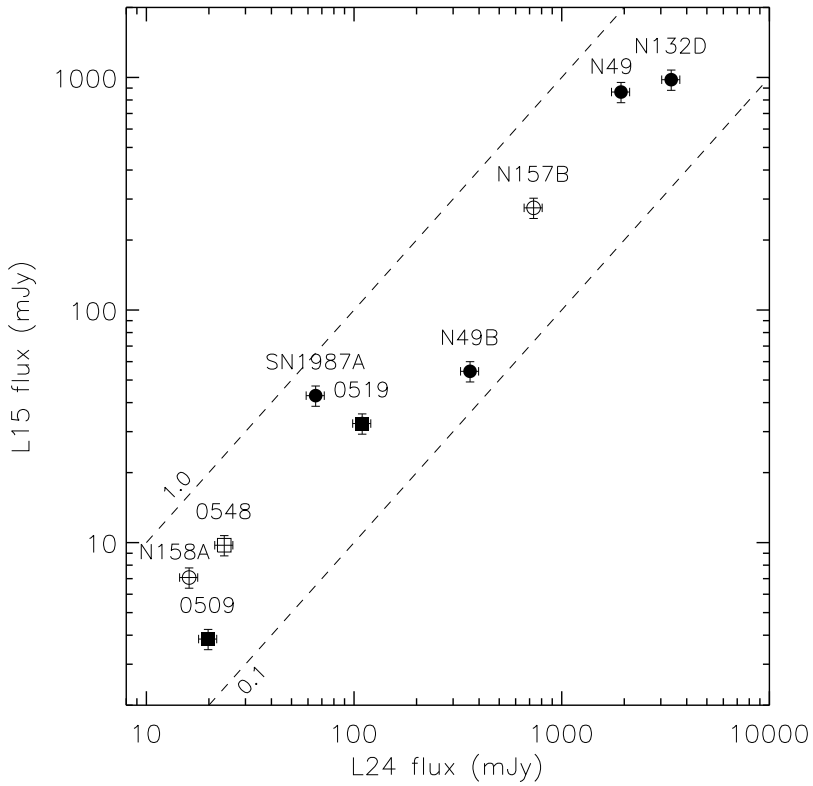

Figure 3.1 L15 flux versus L24 flux for nine identified SNRs. Square symbols are for Type Ia SNRs and circles for Type II SNRs. Open symbols are for the objects of which fluxes are extracted from limited areas. In the case of N158A, the fluxes are extracted only from its PWN. Dashed lines show $L15/L24 = 0.1$ and 1.

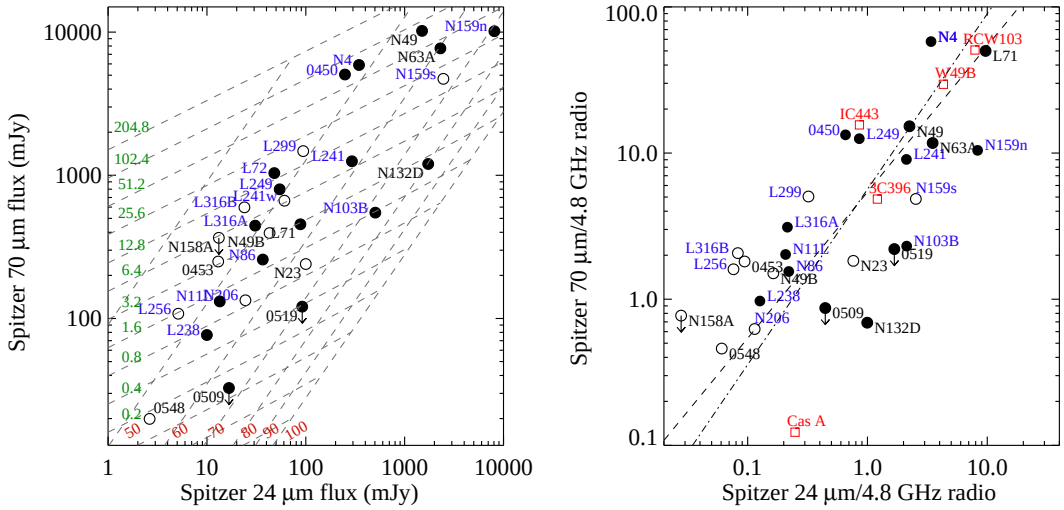

Figure 3.2 *Left*: 70 μm flux versus 24 μm flux for all IR SNRs in the LMC. Fluxes are measured from either whole SNRs (*filled circle*) or limited area of SNRs (*open circle*). Using the modified black-body, 24 and 70 μm fluxes are theoretically calculated at given dust masses and dust temperatures (*dashed line*, see text in §3.1.1). Dust temperature and dust mass range from 40 to 100 K and from 0.1 to 205 $M_{\odot}$, respectively. *Right*: Same as the left plot but all fluxes are normalized to 4.8 GHz radio flux of each SNR. For SNRs having total IR fluxes, we perform a linear fitting in a logarithmic scale given as $y = 5.4^{+1.8}_{-1.3} \times x$ (*dashed line*). As a comparison, ratios of five Galactic SNRs (RCW 103, W49B, IC443, 3C396, and Cas A) are shown (*square*). The correlation of Galactic SNRs in the MIPSGAL survey is also plotted (*dash-dot line*) assuming that the spectral index is 0.5 (slope = 1.2$\pm$0.1, Pinheiro Gonçalves et al. 2011).

(e.g., N63A) have high flux densities as the similar tendency seen in the *AKARI* flux comparison. Assuming that whole MIR emission originates from dust continuum, the *Spitzer* MIR fluxes can be reproduced by adopting a single-component modified black-body. Flux density, F_ν, can be given by

$$F_\nu = \frac{\kappa_\nu B_\nu(T_d)}{d^2} M_d \tag{3.1}$$

where T_d is dust temperature, M_d is dust mass, κ_ν is dust mass absorption coefficient, B_ν is the Planck function, and d is the distance to the LMC (50 kpc). The absorption coefficient is adopted from the "average" LMC model of Weingartner & Draine (2001), which consists of mixture of carbonaceous grains and amorphous silicate grain with the maximum carbon abundance in very small grain population[1]. All fluxes of the SNRs in Figure 3.2 (*left*) can be explained by dust mass of $\sim$ 0.1 to 100 $M_\odot$ and dust temperature of $\sim$ 50 to 90 K. Those having unreasonably high dust mass might indicate either MIR contribution from line emission or existence of multi-components of dust temperature, or both.

3.1.2 IR colors

Figure 3.3 is a "color-color" diagram comparing *S11/L15* to *L15/L24* flux ratios. In the figure, the dashed line represents the relation between the flux ratios for thermal dust emission. The dust emission model that we adopt is a single-temperature modified black-body (Equation 3.1). We also show the synthetic colors of two well-known Galactic SNRs, RCW 103 and IC 443, for comparison. RCW 103 is a young ($\sim 10^3$ yr) SNR with fast ($\geq$ 300 km s^{-1}) shocks interacting with dense CSM/ISM, and its MIR spectrum is dominated by forbidden lines from Ar, Ne, O, and Fe ions (Oliva et al. 1999). On the other hand, IC 443 is a prototype of old SNRs interacting with molecular clouds, and its MIR spectrum is dominated by pure rotational H_2 lines (Neufeld et al. 2007). We synthesized their IRC colors from the published

[1]Absorption coefficient data files are from the homepage of Bruce T. Draine, available at http:www.astro.princeton.edu/$\sim$draine.

spectra to obtain (*L15*/*L24*, *S11*/*L15*) = (1.6, 0.16) and (90, 4.3) for RCW 103 and IC 443, respectively.

Figure 3.3 shows that the MIR flux ratios of the *AKARI* LMC SNRs are quite different from the two line-dominated Galactic SNRs and well aligned along the dust-emission line. Note that Type Ia SNRs are located in the lower left part and SN 1987A has the highest ratios. This good alignment seems to suggest that the MIR emission from these SNRs is, or at least dominated by, thermal dust emission. Indeed, for N132D and SN 1987A, the *Spitzer* spectroscopic observations showed that the contribution from ionic/molecular lines or PAH emission is small in these SNRs (Tappe et al. 2006; Bouchet et al. 2006). Meanwhile, the MIR emission of N49, which is also lying close to the dust-emission line, has been found to be dominated by ionic lines from shocked gas (R. Williams et al. 2006). However, it is not likely that such high temperature ($\sim$ 150 K) can be achieved by this mature ($\sim$ 6600 yr) remnant. Moreover, the colors of the PWN of N158A is similar to the dust emission even though it is a bit apart from the dust-emission line. Therefore, although the fact that an SNR is located close to the dust-emission line in Figure 3.3 alone does not assure that its MIR emission is thermal dust continuum emission, the diagram is still helpful to distinguish between line-dominated and dust-dominated SNRs taking account of their physical contexts. We will discuss the origin of the observed MIR emissions in §3.3.2.

For the SNRs detected in IRAC bands, we compare their IRAC colors ($F_{3.6}/F_{5.8}$ and $F_{4.5}/F_8$) in Figure 3.4. It is known that the origin of IR emission can be inferred by the IRAC colors (Reach et al. 2006). Presumable IRAC colors associated with ionic/molecular shocks, PAHs, and synchrotron emission are adopted from Reach et al. (2006). The representative Galactic SNRs (Cas A, RCW 103, and IC 443) are shown (Pinheiro Gonçalves et al. 2011, and references therein). Recall that RWC 103 and IC 443 are dominated by ionic line emission and molecular line emission, respectively. Most LMC SNRs fall on the area of the diagram for SNRs associated with molecular shocks while several do on the area for SNRs with PAH emission,

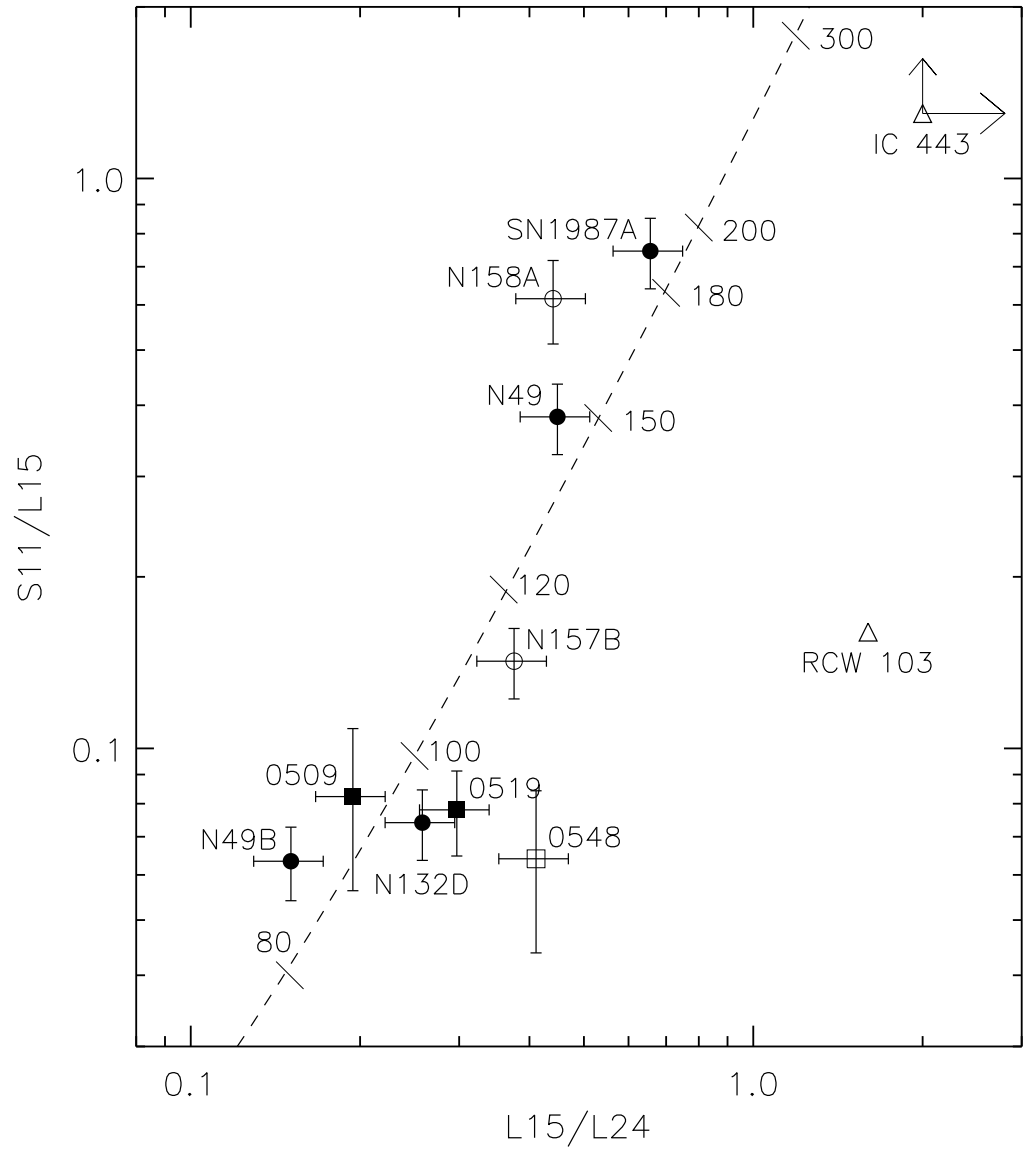

Figure 3.3 *S11/L15* flux ratio versus *L15/L24* flux ratio. Symbol designation is the same as Figure 3.1. The dashed line represents the expected ratios from modified black body curve of thermal dust emission. Dust temperatures are marked along the line. We also show the synthetic colors of two Galactic SNRs, RCW 103 and IC 443 with triangles (see text for an explanation).

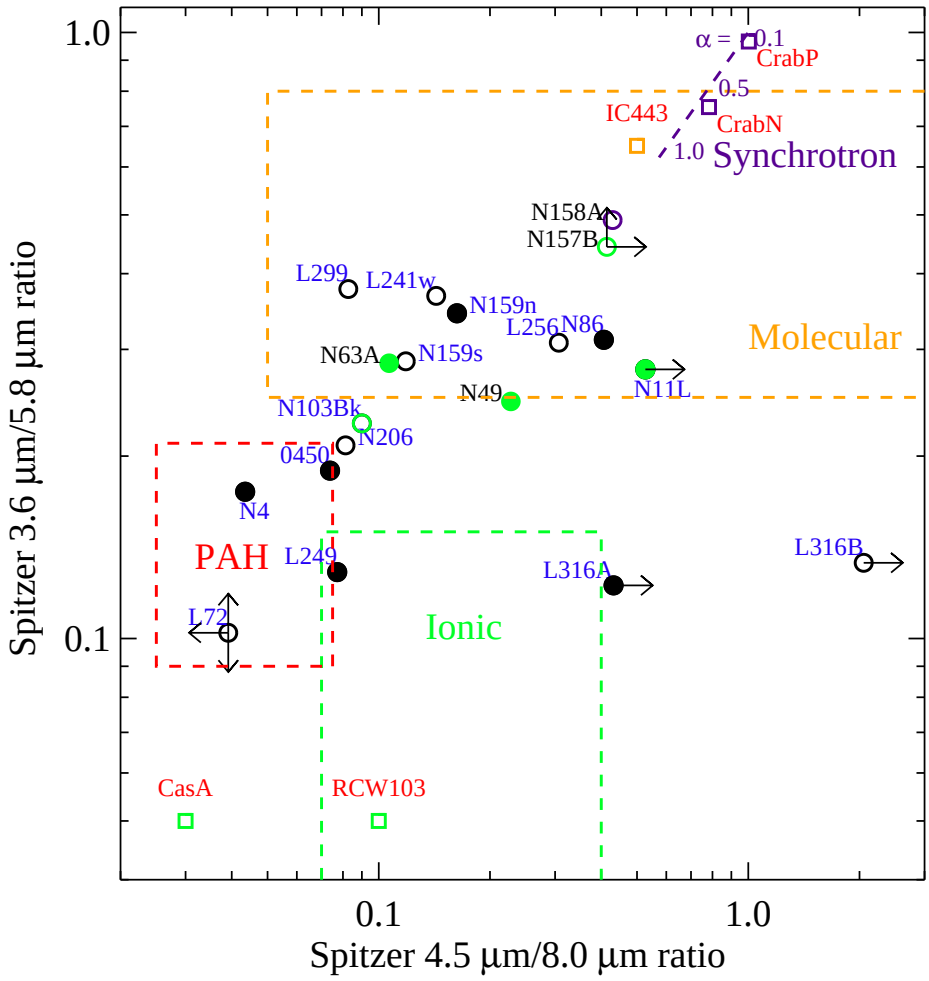

Figure 3.4 An IRAC color-color diagram of the LMC SNRs. Observed IR colors are measured from whole (*filled circle*) or partial (*open circle*) regions of SNRs. Colors of the Galactic SNRs are also shown. Expected IRAC color ranges for ionic (*green*) and molecular (*orange*) shocks, PAH emission (*red*), and synchrotron emission (*purple*) are depicted based on Reach et al. (2006). For SNRs of which dominant mechanisms of IR emission are previously known, their symbols are colored according to the above color classification.

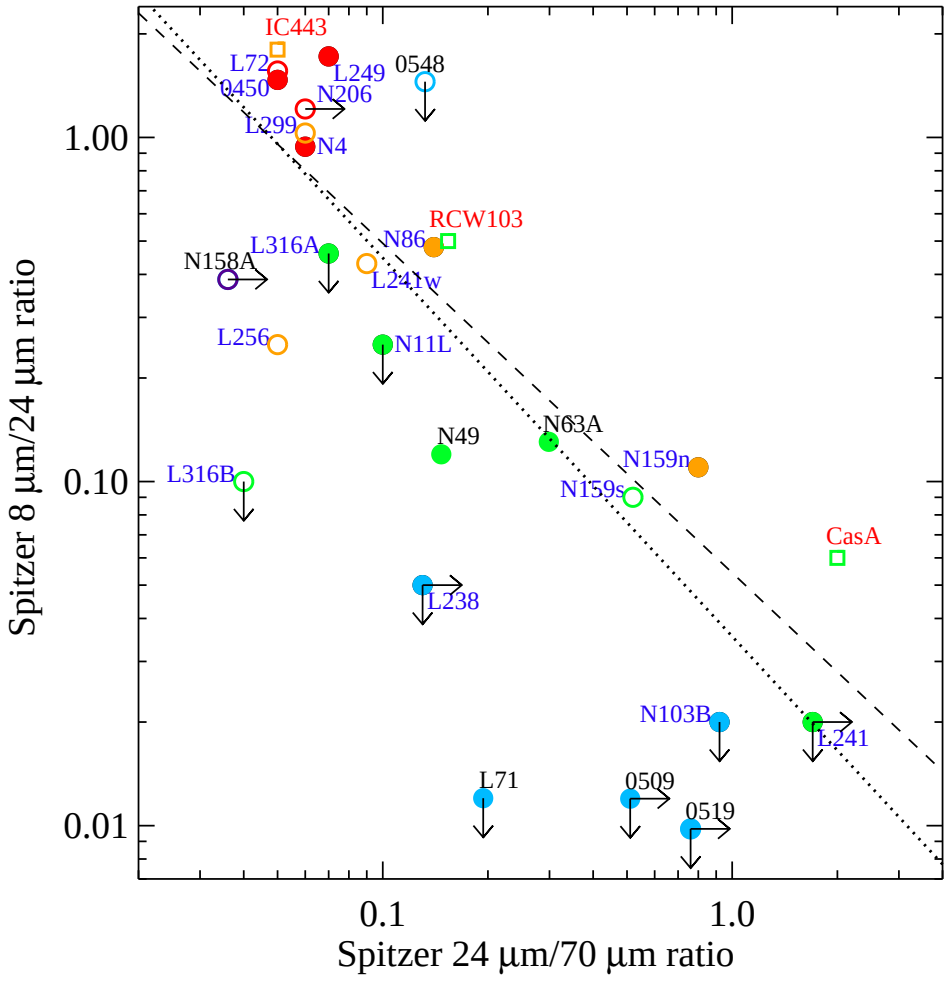

Figure 3.5 MIR color-color diagram of the LMC SNRs using the *Spitzer* 8, 24, and 70 μm fluxes. Symbol designation is the same as Figure 3.4. Colors of symbols represent their known or presumable origins of IR emission, and SNRs dominated by dust emission are marked with an *azure* color (see text for the classification of IR origins). A correlation is found between MIR colors, which can be fitted with a slop of -0.96 ± 0.23 in the logarithmic scale (*dashed line*). The linear correlation derived for Galactic SNRs (Pinheiro Gonçalves et al. 2011) is also overlaid (*dotted line*).

and only few have IRAC colors of SNRs associated with ionic shocks. However, it is noticeable that N49 and N63A, well-known to be ionic-line dominated (e.g., R. Williams et al. 2006), actually have IRAC colors for molecular shocks. This could indicate that it should be cautious to interpret the IRAC colors using this diagram.

Figure 3.5 shows a color-color diagram of 8 μm to 24 μm flux ratios (F_8/F_{24}) versus 24 μm to 70 μm ratios (F_{24}/F_{70}) for the LMC SNRs. As a comparison, the three Galactic SNRs are overlaid, again. There is a crude linear relation between F_8/F_{24} and F_{24}/F_{70}, of which similar trends have been observed for Galactic SNRs (Arendt 1989; Pinheiro Gonçalves et al. 2011). The correlation can be fitted with a slope of -0.96 ± 0.23 in the logarithmic scale, which is similar to the correlation seen for the Galactic SNRs (Pinheiro Gonçalves et al. 2011). In the diagram, it is interesting that relatively young SNRs such as SNR 0509–67.5 or DEM L71 are located in the lower-right area ($F_8/F_{24} \leq 0.05$ and $F_{24}/F_{70} \geq 0.1$) while old SNRs such as SNR 0450–70.9 or DEM L72 are located in the upper-left area ($F_8/F_{24} \geq 0.5$ and $F_{24}/F_{70} \leq 0.1$). This trend might reflect the association between the evolution of a SNR and the mechanism of IR emission (see more §3.3.2).

3.2 Comparison to multi-wavelength data

3.2.1 IR vs. X-ray

Figure 3.6 compares the *AKARI* L24 fluxes (νF_ν) to the X-ray fluxes which are interstellar-absorption corrected X-ray fluxes in energy range of 0.3 to 2.1 keV. For all MIR detected SNRs, X-ray observations using *Chandra* are available. To have a homogeneous set of X-ray fluxes for these SNRs, we derive X-ray fluxes of these sources from archival Chandra data. For the intrinsic flux of the source, correction of the interstellar absorption is required, and the resulting X-ray flux can be sensitive to assumed hydrogen column density (N_H). When available, we adopt N_H from literatures, and the X-ray flux in the given energy range is estimated by fitting the X-ray spectrum from the archival data. When N_H is not readily available from

literatures, N_H was also derived by fitting the X-ray spectrum. The uncertainty of the intrinsic flux is dominated by uncertainty in N_H. We consider our absorption corrected X-ray fluxes will be uncertain by a factor of a few at most. In the case of SN 1987A of which time variation in X-ray flux is considerably large, we interpolate the latest fluxes from Park et al. (2007) to obtain the X-ray flux corresponding to the *AKARI* flux. Using the MIR-L and the X-ray data, it is found that there is a good correlation between the two fluxes. Both the L24 and L15 fluxes show a good correlation with the X-ray fluxes (correlation coefficient = 0.98 and 0.90, respectively). The relation between the L24 and X-ray fluxes derived from a linear least-squares fit is

$$[\nu F_\nu]_{24\mu\mathrm{m}} = (1.28 \pm 0.10) \times F_X \tag{3.2}$$

where $[\nu F_\nu]_{24\mu\mathrm{m}}$ (erg cm^{-2} s^{-1}) is the flux in the L24 band and F_X (erg cm^{-2} s^{-1}) is the X-ray flux in 0.3–2.1 keV band. For this and later fits, we exclude N157B and 0548–70.4 of which IR fluxes are extracted from the limited areas but include N158A of which both IR and X-ray fluxes are from its PWN.

The correlation between the two fluxes is expected to some degree because the IR brightness distributions of the identified SNRs are in general correlated with their X-ray distributions except N157B. If the MIR emission is dominated by thermal dust continuum emission, the dust grains emitting the MIR emission are heated by collisions with electrons in the X-ray emitting plasma so that the two are physically associated, although the flux ratio depends on plasma temperature and therefore on the age of the remnant (e.g., Dwek et al. 2008). The correlation in Figure 3.6 (*left*) is *not* the result of both quantities being proportional to the SNR area. It is shown in Figure 3.6 (*right*) displaying the surface brightness of the SNRs at 24 μm and X-ray. There is a good correlation between the surface brightnesses too, and the best fit is given as

$$\Sigma_{24\mu\mathrm{m}} = (1.28 \pm 0.01) \times \Sigma_X \tag{3.3}$$

where $\Sigma_{24\mu\mathrm{m}} \equiv [\nu F_\nu]_{24\mu\mathrm{m}}/\Delta\Omega_S$ and $\Sigma_X \equiv F_X/\Delta\Omega_S$ where $\Delta\Omega_S$ is the total solid angle of the SNR from table 2.1. Since the fluxes of N157B and 0548–70.4 were

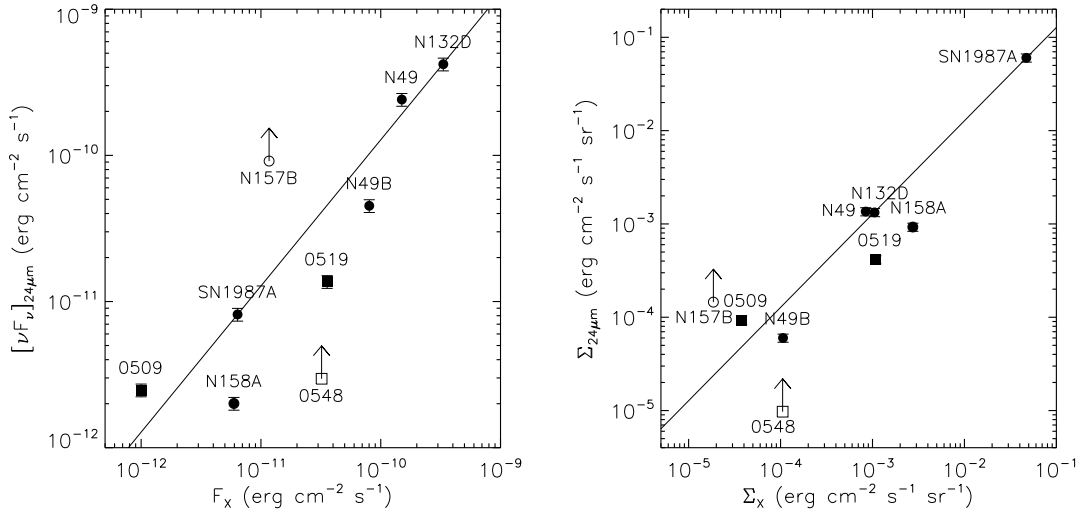

Figure 3.6 *AKARI* 24 μm versus *Chandra* X-ray ($0.3-2$ keV) fluxes (*left*) and surface brightness of the SNRs (*right*). Symbol designation is the same as Figure 3.1, but note that the symbol of N158A is filled here since both the IR and X-ray fluxes are extracted from its PWN. The solid line represents best-fit linear-regression line.

derived from limited areas, their surface brightnesses are lower limits. When the MIR emission originates mainly from dust, the dust temperature depends on the density and temperature of electrons. The X-ray flux is proportional to square of electron density, and at sufficiently high temperature and high densities, the dust temperature becomes only dependent on the electron density (Dwek et al. 2008, and see §3.3.3). This suggests the MIR surface brightness is closely related to the electron density so that the relationship can lead to the good correlation shown in Figure 3.6.

We compare *Spitzer* 24 μm fluxes (νF_ν) to *Chandra* soft band ($0.3-2$ keV) X-ray fluxes in Figure 3.7. All X-ray fluxes are from the *Chandra* SNR catalog except for DEM L241, of which X-ray flux is estimated by using *XMM-Newton* data ($0.5-10$ keV, Bamba et al. 2006). In general, since the contribution of hard X-ray component

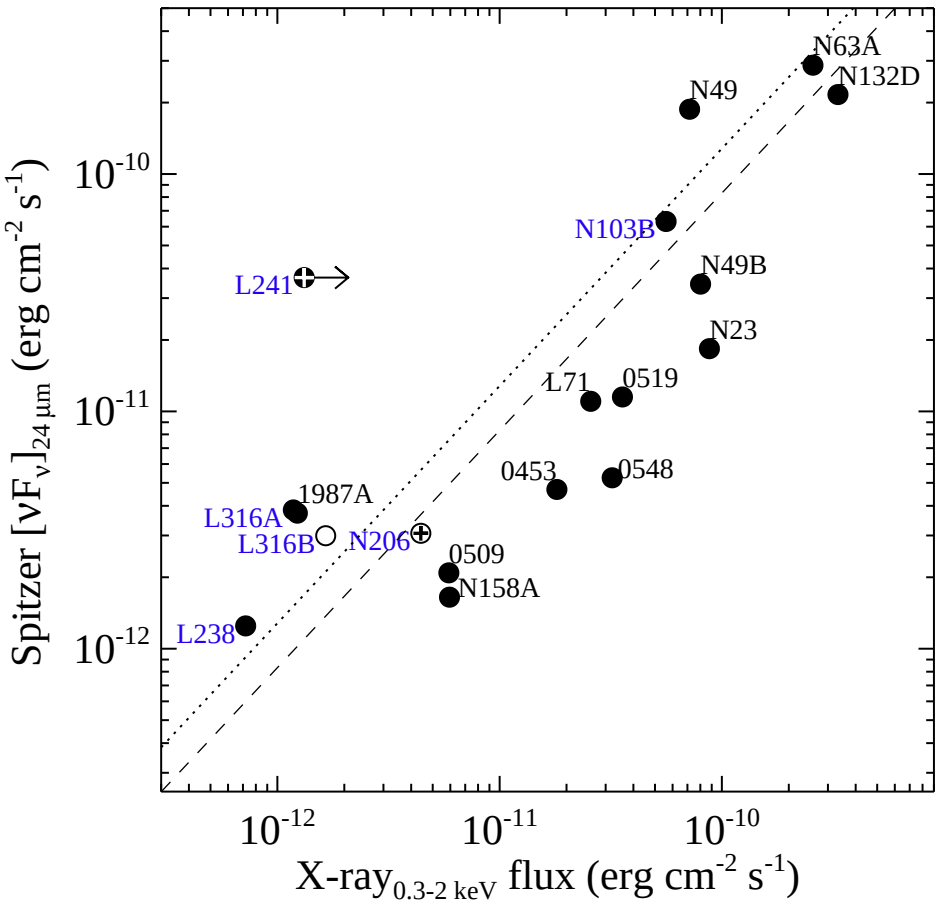

Figure 3.7 Correlation between *Spitzer* 24 μm fluxes and X-ray fluxes. All X-ray fluxes are *Chandra* (0.3−2 keV) fluxes from the *Chandra* SNR catalog, but for DEM L241, a *XMM-Newton* wide-band ($0.5 - 10$ keV) flux is used (Bamba et al. 2006). Although the *XMM-Newton* flux is from a wider band, the hard X-ray emission (≥ 2 keV) is usually less than the soft X-ray emission ($0.3 - 0.5$ keV) in a SNR, so the X-ray flux of DEM L241 is regarded as a lower-limit. Symbol designation is the same as Figure 3.2, but the symbol of N158A is filled as mentioned in Figure 3.6. Also two SNRs (SNR in N206 and DEM L241) without spatial correlation between IR and X-ray emission are marked (*cross*). The correlation is fitted by a slope of $0.83^{+0.34}_{-0.24}$ (*dashed line*), which is slightly lower than that seen in the *AKARI* survey (slope $= 1.28 \pm 0.10$, *dotted line*).

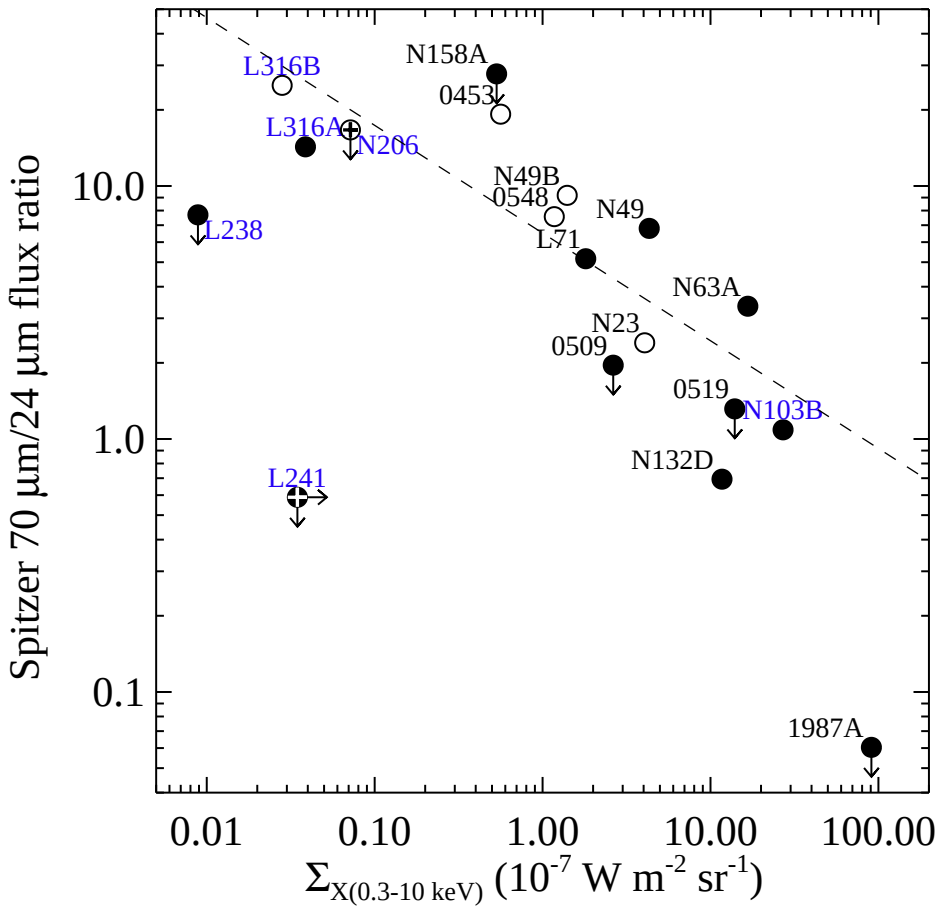

Figure 3.8 *Spitzer* 70/24 flux ratios vs. X-ray surface brightness. Symbol designation is the same as Figure 3.7. The correlation between the ratios and the surface brightnesses can be fitted by a function of $y = 6.52^{+1.45}_{-1.19} \times x^{-0.43\pm0.09}$ (*dashed line*).

is less than a few percentage, the *XMM-Newton* flux is comparable to those of other SNRs. While all X-ray fluxes are from whole SNR regions, 24 μm fluxes of some SNRs are estimated from limited regions of the SNRs (*open circle*), so only 24 μm fluxes from whole SNRs (*filled circle*) can be used for the comparison. As expected from morphological similarities between the 24 μm and X-ray images (Figure 2.4), the 24 μm fluxes are well-correlated with the X-ray fluxes (correlation coefficient = 0.86). We measure the slope of the correlation by using a linear fit, and the best fit is given as $F_{24\mu\mathrm{m}} = (0.83^{+0.34}_{-0.24}) \times F_{\mathrm{X}}$. The slope is in agreement with one derived from SNRs in the *AKARI* survey (1.28 ± 0.10 in Equation 3.2).

This good correlation between IR and X-ray can be inferred by the fact that MIR emission in a SNR is indeed physically related to X-ray emission. Dust continuum is considered as a primary origin of MIR emission ($\geq 10\mu$m) from a SNR although ionic emission lines such as an [O IV] line at 25.88 μm and a [Fe II] line at 25.98 μm, might overwhelmingly contribute the MIR emission (e.g., up to 80% of the MIPS 24 μm emission for SNR N49, R. Williams et al. 2006). It is known that dust continuum arises from collisional heating by hot plasma emitting X-ray emission. Dust temperature directly depends on the plasma properties, in particular, electron density and electron temperature (e.g., Dwek 1987; Dwek et al. 1987), which can result in the tight correlation between IR and X-ray emission.

In addition, *Spitzer* 70/24 μm flux ratios are compared with X-ray surface brightness (Figure 3.8). There is a trend that the 70/24 ratios decrease as the X-ray surface brightnesses increase. Even SNRs with their IR fluxes extracted from limited areas also follow this trend while their X-ray brightnesses are measured from the whole. The trend can be fitted by a function of $y = 6.52^{+1.45}_{-1.19} \times x^{-0.43\pm0.09}$. This trend can be attributed to the dependency of dust emission on density of hot gas emitting X-rays. Meanwhile, the correlation becomes weak at the low X-ray surface brightness. If X-ray emitting gas becomes cooler, both gas temperature and density affect dust temperature, which might explain the weak correlation. This correlation between 70/24 ratios and X-ray brightnesses has recently been found in the Galactic SNR,

G292.0+1.8 (see Figure 5 in Ghavamian et al. 2012). IR as well as X-ray fluxes are extracted from different regions in G292.0+1.8, and the 70/24 ratios show a declining trend with increasing X-ray surface brightness. However, it should be cautious to interpret Figure 3.8, because IR emission in some SNRs can be contributed by ionic line (or synchrotron) emission. As Ghavamian et al. (2012) mention, X-ray surface brightness can also be overestimated due to ejecta emission which is not related to the shocked circumstellar (or interstellar) dust.

The relative strength, a ratio of IR-to-X-ray fluxes (IRX ratio), is often used as an indicator of the dominant cooling mechanism during the lifetimes of SNRs (Dwek et al. 1987). A dusty ISM is known to be cooled either by an IR cooling mechanism by gas-grain collisions or a cooling mechanism by atomic processes. To estimate IRX precisely, a flux of soft X-rays radiated by slow shocks interacting with dust and a total IR flux are needed. However, it is difficult to measure both the fraction of the soft X-ray flux in the $0.3-2$ keV band flux and the total IR fluxes for the LMC SNRs. Thus, we simply use the 24 μm fluxes ($[\nu F_\nu]_{24\mu\mathrm{m}}$) and the $0.3-2$ keV X-ray fluxes to derive IRX ratios, which can be regarded as a lower-limit of the IRX ratio. Most SNRs show the IRX ratios between 0.35 and 3.26 except DEM L241 with a large IRX (~ 28). The large IRX of DEM L241 might be due to the different band coverage of *XMM-Newton* although there are several Galactic SNRs having the IRX ratios higher than 100 (e.g., Cas A: 340., IC 443: 360, Dwek et al. 1987). The average IRX is 1.59 excluding DEM L241, and we can also obtain the representative IRX of 1.60 using the derived 24 μm–X-ray correlation. The average of IRX, actually a lower-limit of IRX, is higher than unity, which suggests that the IR cooling is the dominant cooling mechanism, in general.

The IRX ratio can also constrain the dust abundance in the environement. If a dust-to-gas mass ratio is fixed, IRX depends only on plasma temperature (Dwek et al. 2008). For the LMC ISM abundance taken as a 0.6 times solar abundance (Welty et al. 1999), the theoretical IRX ratio is from about 2 to 12 for soft X-rays with $T_e \sim 3 \times 10^6$ K (Dwek et al. 2008). When the observed IRX is lower or higher than

the theoretical value, it can imply dust destruction or dust enhancement. Since we only have lower-limits of IRX ratios, it is difficult to say whether the measured IRX of 1.59 indicates that dust grains in SNRs are destroyed by shocks or not. To clarify the presence of dust destruction, careful inspection of both IR spectra and X-ray spectra of the LMC SNRs must be required.

Spatial correlation between IR and X-ray

Although the good correlation between the IR and X-ray fluxes is found, the IR morphologies of some SNRs are not well matched with their X-ray morphologies. We compare the IR morphologies of the SNRs to their X-ray morphologies by using the archival *Chandra* data (Figure 3.9) and *XMM* images from literatures (Klimek et al. (2010, for DEM L72 and DEM L256), Bamba et al. (2006, for DEM L241)). Among the 28 IR SNRs, nine SNRs show considerable discrepancy between IR and X-ray morphologies (listed in Table 3.1) whereas 15 SNR do show good spatial correlation. There is no available X-ray data for the other four SNRs. There are various conditions that can deform the IR morphology of a SNR, and one of the primary factors can be an interaction with a nearby molecular cloud. Since the good spatial correlation basically arises by dominant dust emission associated with hot plasma, significant contribution from different IR origins can make the IR morphology unrelated to the X-ray. When a SNR interacts with an ambient molecular cloud, strong molecular emission can contribute the total IR emission of the SNR. Also, the dense regions can protect PAHs against complete destruction by shocks, so PAH emission can also contribute considerably. In fact, all nine SNRs show NIR emission; The IRAC colors of three SNRs (DEM L72, SNR in N206, and DEM L249) are similar to the colors for PAH emission, and the colors of the others are similar to those for molecular shocks (Figure 3.4).

For those SNRs without the IR-X-ray correlation, we examine the existence of CO emission around each SNR to find more direct evidence for the interaction with molecular clouds. For the inspection, we use a masked CO intensity map from

Table 3.1. Nine LMC SNRs without good spatial correlation between IR and X-ray

SNR	NANTEN[a]	MAGMA[b]	Note[c]
N11L	N	N/A	CO emission adjacent to the southern boundary
DEM L72	N	N/A	No CO emission observed
SNR in N206	N	N/A	CO emission adjacent to the southern boundary
DEM L241	Y	Y	CO emission seen inside the SNR
DEM L249	N	Y	Weak CO emission at the southern part detected by MAGMA
DEM L256	Y	N/A	CO emission at the northern part detected by NANTEN
N157B	Y	Y	CO emission at the southern part
SNR in N159	Y	Y	Strong CO emission across the SNR
N158A	N	Y	CO emission near the northern boundary detected by MAGMA

Note. — Among 28 SNRs with IR emission, nine do not show spatial IR-X-ray correlation. Except four SNRs without available X-ray data, the rest of them show good correlation. In the case that the *Chandra* data is not available, references for the X-ray data are listed.

[a]Presence or absence of CO emission near a SNR based on NANTEN survey from (Table 1 in Desai et al. 2010)

[b]Presence or absence of CO emission near a SNR based on MAGMA survey. Y: Exist, Y: No emission seen, N/A: No available data.

[c]Short description about CO emission around SNRs.

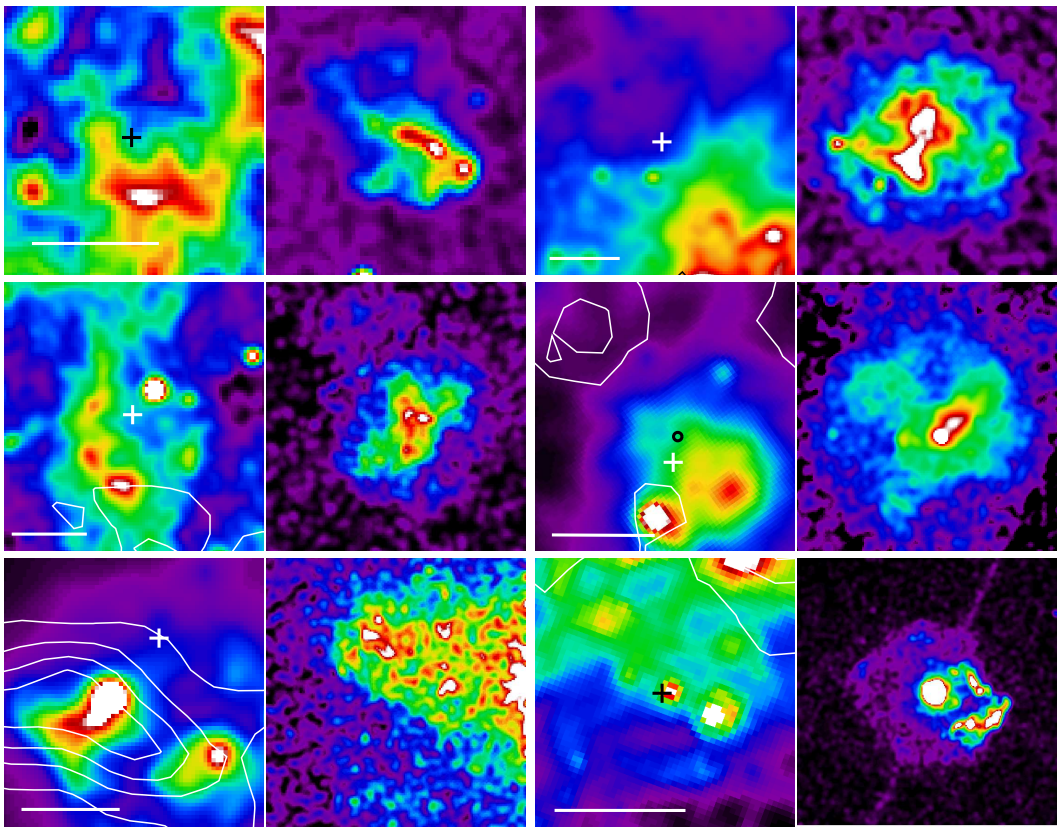

Figure 3.9 *Spitzer* 24 μm and X-ray images of six SNRs showing spatial discrepancy between IR and X-ray emissions. From the top-left, N11L, SNR in N206, DEM L249, N157B, SNR in N159, and N158A. CO contours from MAGMA data are overlaid in the 24 μm images of each SNR. Contour levels are 0.5 to 3.5 K km s^{-1} at intervals of 1 K km s^{-1}, but CO levels in DME L249/SNR in N159 are different as there are very weak/strong CO emission around them (0.25 to 1 K km s^{-1} at intervals of 0.25 K km s^{-1} for DEM L249 and 5 to 25 K km s^{-1} at intervals of 5 K km s^{-1} for SNR in N159). The cross marks the center position of each SNR listed in Table 2.1, and the scale bar corresponds 1$'$ (i.e., 15 pc at 50 kpc). A circle in the 24 μm image of N157B denotes the position of its pulsar. North is up, and east is to the left.

the MAGMA Data Release 1[2] (Magellanic Mopra Assessment, Wong et al. 2011). The MAGMA survey is CO ($J = 0 \rightarrow 1$) observations done by the Mopra 22 m telescope, which covers $\sim$ 100 giant molecular clouds (GMCs) selected based on a previous survey for GMCs in the LMC, the NANTEN survey (Fukui et al. 2001). The detection limit of the MAGMA is approximately $I_{\rm CO} = 2$ K km s^{-1} (or $N({\rm H_2}) \sim 1.4 \times 10^{22}$ cm^{-2}). Since the MAGMA survey does not cover the all LMC SNRs, we also refer images of the NANTEN survey, Figure 1 and 2 in Desai et al. (2010). Among the nine SNRs, six SNRs actually show the association with molecular clouds in the MAGMA and/or NANTEN surveys (Table 3.1). In addition, we can verify CO emission adjacent to the southern boundaries of two SNRs, N11L and SNR in N206. As the MAGMA survey does not cover these SNRs, and the NANTEN survey has a large beam ($2'.6$ half power beam), small clouds that possibly exist around them would not be detected. The last one, DEM L72 does not have any evidence for the interaction with a molecular cloud. However, considering that the IR emission in DEM L72 is categorized to PAH emission, the existence of PAHs could indicate the presence of dense clumps as discussed later in Chapter 4 (also see Micelotta et al. 2010a). Therefore, the IR emission arising from the interaction with dense ambient medium (e.g., molecular clouds) possibly leads the lack of the spatial correlation between IR and X-ray.

3.2.2 IR vs. radio

Figure 3.10 compares the *AKARI* L24 flux (F_ν) to the radio flux at 4.8 GHz. We derived the radio fluxes by using the *ATCA* 4.8 GHz continuum images of Dickel et al. (2005). We estimated the background intensity using an annulus for most sources. The statistical errors (1 σ) of the SNRs are less than 5%. For SN 1987A, due to the time-variability of its radio flux, we applied a flux density gradient (17.5

[2]The masked intensity map is made by masking by the 3-σ contour of a cube that has been smoothed to $90''$ resolution, then integrating from 200 to 305 km s^{-1}. The data can be downloaded from http://mmwave.astro.illinois.edu/magma/DR1/.

μJy day^{-1}, Manchester et al. 2002) to the observed 4.8 GHz flux (33 mJy in day 5846) in order to obtain the radio flux corresponding to the *AKARI* flux, i.e. 33 mJy + 17.5 μJy day$^{-1}\times$ (7190 $-$ 5846 day) $\simeq$ 56.5 mJy. The scaled flux is used for a further analysis. Figure 3.10 shows that there is a fairly tight correlation between the two fluxes. The correlation is as good as that between the L24 and X-ray fluxes (correlation coefficient = 0.98). The relations derived from a least-squares fit are

$$[F_\nu]_{24\mu\mathrm{m}} = (1.89 \pm 0.09) \times F_{4.8\mathrm{GHz}} \tag{3.4}$$

and

$$\Sigma_{24\mu\mathrm{m}} = (1.89 \pm 0.09) \times \Sigma_{4.8\mathrm{GHz}} \tag{3.5}$$

where $F_{4.8\mathrm{GHz}}$ (erg cm^{-2} s^{-1} Hz^{-1}) is the radio flux at 4.8 GHz and $\Sigma_{4.8\mathrm{GHz}} \equiv F_{4.8\mathrm{GHz}}/\Delta\Omega_S$ is the radio surface brightness at 4.8 GHz.

The correlation between the L24 and radio fluxes in Figure 3.10 is remarkable considering that there is no direct physical connection between the IR and the radio synchrotron emission. The synchrotron emission is due to the compression of electrons and magnetic fields in the ISM except the PWN N157B and N158A. The contribution of synchrotron emission to the observed 24 μm emission should be negligible. Then the apparent correlation between the two fluxes in the figure could be due to their common dependence on the physical parameters of SNRs such as shock velocity and ambient density. We note that Type Ia SNRs are faint in both IR and radio (and X-ray too), while the SNRs probably interacting with nearby molecular clouds are bright in both bands. Since Type Ia SNRs are expected to be in a lower-density environment, this trend indicates that one of the most important factors for the detection in the IR is likely to be the density of the ambient medium, and the correlation between IR and radio might arise from their common dependence on the density.

This correlation could be compared to that among galaxies. It has been known for over three decades that there is a tight correlation between the far-infared and radio emission from galaxies, and recent *Spitzer* studies have shown that even MIR

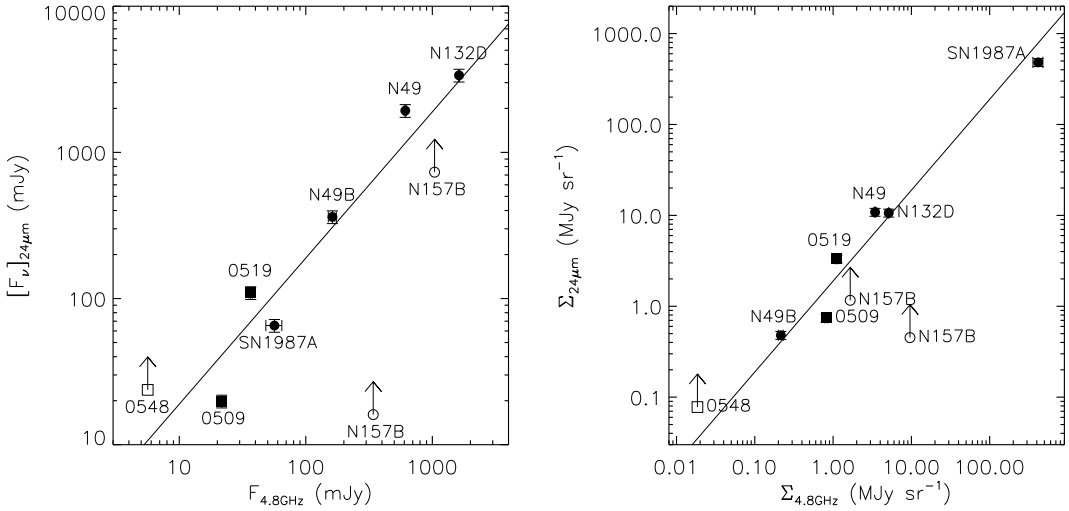

Figure 3.10 *AKARI* 24 μm versus 4.8 GHz radio continuum fluxes (*left*) and surface brightness (*right*). The solid line represents best-fit linear regression line.

and radio has a fairly good correlation ($F_{24\mu\mathrm{m}}/F_{1.4\mathrm{GHz}} \sim 7-25$, Appleton et al. 2004; Boyle et al. 2007). For comparison, the corelation in Figure 3.10 implies the 24 μm to 1.4 GHz flux ratios of 1.0 using a spectral index of -0.5 for radio synchrotron emission. Therefore, if the 1.4 GHz radio emission from galaxies is mainly from SNRs, the contribution of SNRs to the 24 μm fluxes from galaxies would be $4-14$ %, the rest of which might be contributed from the star-formation activity.

Similarly, we compare the *Spitzer* 24 μm fluxes to the 4.8 GHz radio fluxes in Figure 3.11. The 24 μm fluxes are moderately correlated to the 4.8 GHz fluxes (correlation coefficient = 0.61), however the correlation becomes worse than that seen in the *AKARI* 24 μm fluxes of fewer samples (correlation coefficient = 0.98). The correlation can be derived by performing a linear fit, which gives $F_{24\mu\mathrm{m}} = (0.97^{+0.30}_{-0.23}) \times F_{4.8\mathrm{GHz}}$. The measured slope is lower than that of the *AKARI* samples (slope = 1.89, Equation 3.4). We try to describe the data better by adopting one more term for fitting, which gives $F_{24\mu\mathrm{m}} = (0.49^{+1.08}_{-0.34}) \times F_{4.8\mathrm{GHz}}^{1.14\pm0.23}$. This relation

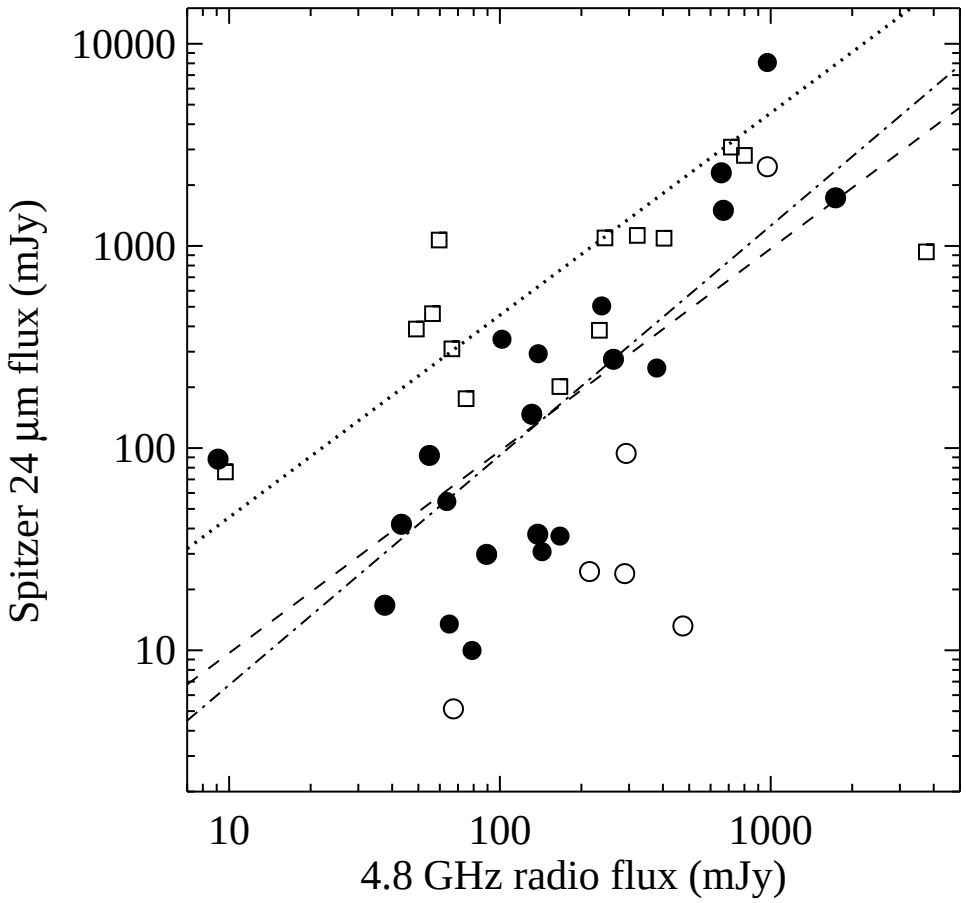

Figure 3.11 Correlation between *Spitzer* 24 μm fluxes and *ATCA* 4.8 GHz radio fluxes. Symbol designation is the same as Figure 3.2. Fluxes of the Galactic SNRs (*square*) are scaled to the distance of the LMC for comparison. The correlation is fitted by a slope of $0.97^{+0.30}_{-0.23}$ (*dashed line*) which is lower than that of LMC SNRs in the *AKARI* survey (slope = 1.89±0.09, *dotted line*). To describe the data better, one more term is adopted to fit, and the result is given as $F_{24\mu\mathrm{m}} = (0.49^{+1.08}_{-0.34}) \times F_{4.8\mathrm{GHz}}^{1.14\pm0.23}$ (*dash-dotted line*).

explains the observed correlation slightly better, but the difference is not significant. When IR fluxes are compared with radio fluxes, there is a well-known property for the ratio of IR-to-radio flux, $q_{\lambda,\mathrm{IR}} = \log(F_{\lambda,\mathrm{IR}}/F_{1.4\mathrm{GHz}})$ where $F_{\lambda,\mathrm{IR}}$ and $F_{1.4\mathrm{GHz}}$ are flux densities at a given IR wavelength and 1.4 GHz (i.e., 21 cm), respectively. Then, q_{24} can be derived by $q_{24} = \log(F_{24\mu\mathrm{m}}/F_{4.8\mathrm{GHz}}) - \alpha\log(4.8\ \mathrm{GHz}/1.4\ \mathrm{GHz})$, where α is a spectral index of a SNR. Since spectral indices of the LMC SNRs are not specified, we assume them as 0.5 en bloc. The q_{24} of the individual SNRs range from -1.17 to 0.72, and the total q_{24} for the LMC SNRs, $q_{24,tot} = \log(\Sigma(F_{24\mu\mathrm{m}})/\Sigma(F_{1.4\mathrm{GHz}}))$, is 0.14.

We investigate the ratios of IR fluxes to 4.8 GHz radio fluxes for each SNRs (Figure 3.2, *right*). Note that some IR fluxes are extracted from limited regions while all radio fluxes represent total fluxes. There is a good correlation between the ratios as expected from the good correlation between 24 and 70 μm fluxes (Figure 3.2, *left*). This correlation is well fitted by a linear function in logarithmic scale given as $y = 5.4^{+1.8}_{-1.3} \times x$. For this fitting, IR fluxes estimated from the whole SNRs are used only. We compare this result with the case of Galactic SNRs. Ratios of five representative Galactic SNRs and a slope derived for Galactic SNRs in the MIPSGAL survey are overlaid. To derive the ratios of the Galactic SNRs, we take IR properties of four SNRs from Pinheiro Gonçalves et al. (2011) and of Cas A from Hines et al. (2004) and convert their 1 GHz fluxes to 4.8 GHz fluxes using their spectral indices from Green (2009). The slope of Galactic SNRs is measured by Pinheiro Gonçalves et al. (2011) using 1.4 GHz fluxes instead of 4.8 GHz, which is 1.2 ± 0.1. We assume the spectral index as 0.5 ($\alpha = 0.5$) en bloc and then compare their correlation to ours. It seems that the LMC SNRs reasonably follow the correlation of the Galactic SNRs, too.

Despite of the relatively good agreement between the ratios of Galactic and LMC SNRs, it is found that there are some differences between them. The total q_{24} ($= 0.14$) is smaller than that of the Galactic SNRs in MIPSGAL survey ($q_{24} = 0.39 \pm 0.11$ excluding objects closer to H II region, Pinheiro Gonçalves et al. 2011).

This discrepancy is directly depicted in both Figure 3.2 (*right*) and Figure 3.11. By scaling 24 μm and radio fluxes of Galactic SNRs from Pinheiro Gonçalves et al. (2011) to the distance of the LMC (50 kpc), the fluxes of the LMC SNRs can be compared to the fluxes of the Galactic SNRs. Figure 3.11 clearly shows that there are more IR faint SNRs in the LMC relative to the Galactic SNRs while radio fluxes of both SNRs are comparable. Except Cas A in Figure 3.2 (*right*), many of the ratios of the LMC SNRs are lower than those of the Galactic SNRs. The Galactic SNR, 3C396 is one of the Galactic SNRs having the lowest ratio in Pinheiro Gonçalves et al. (2011), and the majority of the LMC SNRs show lower ratios then that of 3C396. In fact, q_{24} is often measured for galaxies because MIR/radio correlation is well-known among galaxies (e.g., $q_{24} = 0.84 \pm 0.28$, Appleton et al. 2004). The q_{24} of the LMC SNRs is much smaller that that of the extragalactic galaxies. If 1.4 GHz radio emissions of galaxies mainly originate from synchrotron emission of SNRs, our result implies that only little portion of IR emission can be contributed by the SNRs $(6 - 20\%)$. Since the Galactic SNRs have higher q_{24}, however, this low q_{24} might be an intrinsic characteristic of the LMC SNRs (see §3.3.1).

3.3 Discussion

3.3.1 Characteristics of IR SNRs in the LMC

One of the remarkable results in this study is the high detection rate of IR SNRs. IR counterparts of 28 LMC SNRs out of 45 are identified in the IRAC and/or MIPS bands, which is about 62% detection rate. In the case of Galactic SNRs, 18 out of 95 SNRs were clearly detected in the GLIMPSE survey (Reach et al. 2006), and 39 out of 121 SNRs were detected in the MIPSGAL survey (Pinheiro Gonçalves et al. 2011). Their detection rates are about 20% and 32%, respectively. Even for the previous studies by using the *IRAS* all-sky survey, about 30% detection rates are obtained for the Galactic SNRs (Arendt 1989; Saken et al. 1992). In comparison with these previous results, the IR detection rate of the LMC SNRs seems to be

interestingly high.

This high detection rate could be caused by either extrinsic or intrinsic aspects. One of the apparent extrinsic effects is less IR confusion by Galactic disk. Both the GLIMPSE and the MIPSGAL surveys are restricted to the inner Galactic plane ($|b| < 1^{\circ}$), so contamination by other Galactic sources must be very severe. Even if the *IRAS* all-sky survey includes whole Galactic SNRs, back/foreground confusion is still a serious problem to disentangle IR emission associated with SNRs from other emission. Besides, due to the limited spatial resolution of *IRAS*, small and faint structures might be difficult to be identified. In fact, we compare the intensity distribution of the LMC and the MIPSGAL SNRs detected in the MIPS 24 μm band (Figure 3.12). After scaling the fluxes from the Galactic SNRs to the distance of the LMC (50 kpc), it is found that the median flux of the Galactic SNRs is higher than that of the LMC SNRs (284 mJy and 92 mJy, respectively). This might indicate that we detect more IR-faint SNRs in the LMC, and there could be missing detection of Galactic SNRs with faint IR emission.

Since there are physical and chemical differences between the Milky Way and the LMC, it would be natural to think whether those differences can intrinsically affect the IR emission from a SNR. One of the chemical differences is related to dust component. The LMC is known to have lower dust-to-gas ratio and lower metallicity than the Galaxy (Pei 1992). Moreover, dust composition (graphite to silicate ratio, $\mathrm{r}_c/\mathrm{r}_s$) of the LMC is also known to differ from the Galaxy. While $\mathrm{r}_c/\mathrm{r}_s$ of the LMC is about 0.22, $\mathrm{r}_c/\mathrm{r}_s$ of the Galaxy is about $0.9-0.95$ (Pei 1992). This chemical deviation of the dust component can affect the lifetime of dust in a postshock region. When a shock of $v = 400$ km s^{-1} is propagating into a dusty medium with a preshocked density of $n_0 = 0.1$ cm^{-3}, 21% of graphite are returned to the gas phase while 29% of silicates are returned at $N_H = 1.25 \times 10^{18}$ cm^{-2} (Dwek et al. 1996). This indicates that the silicate is more rapidly destroyed by shocks, so under the same shock conditions, the dust in the LMC is more easily destroyed than the Galactic dust. Then, this fact does not support the intrinsic effect which can make the IR

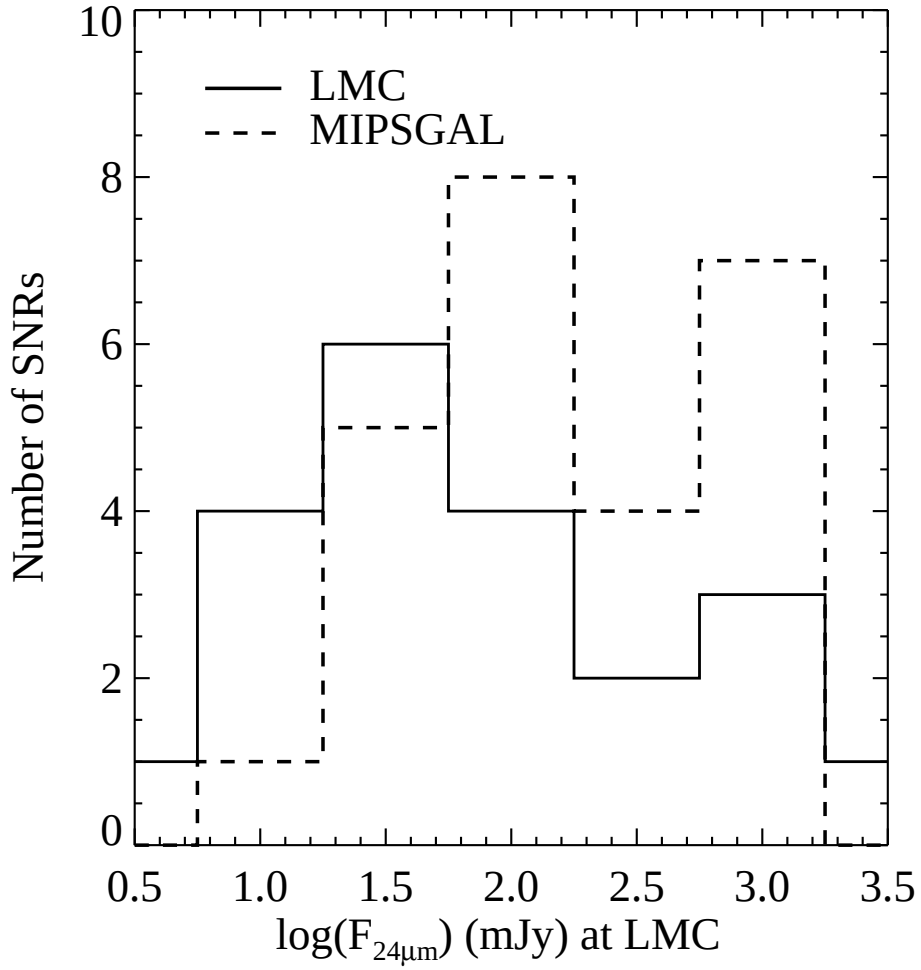

Figure 3.12 Histogram of MIPS 24 μm fluxes estimated from LMC and Galactic SNRs. Only fluxes measured from whole SNRs are used (i.e., 21 LMC SNRs and 25 Galactic SNRs). For the Galactic SNRs, their fluxes are scaled to the distance of the LMC (50 kpc) either using their known distances or assuming their distances as 3 kpc.

detection rate of the LMC increase.

If there is no intrinsic difference for the IR emission between the LMC and the Galactic SNRs, the lower slope of the IR-to-radio ratio (or lower q_{24}) for the LMC SNRs than those of the *AKARI* sample or Galactic SNRs (Pinheiro Gonçalves et al. 2011) might be explained by the additional detection of faint IR SNRs. Considerable new detection of IR SNRs in the LMC might implicate their faintness in IR bands, and faint IR emission of Galactic SNRs would be much more difficult to identify or distinguish from other IR emission of Galactic sources. As IR emission in a SNR could be severely affected by the interaction with the ambient medium (i.e., the environmental conditions), the IR brightness can be evolved differently from the radio continuum. Hence, the detection of a number of IR faint SNRs relative to their radio brightnesses can result in the lower q_24 value although we cannot rule out any subtle effects from the intrinsic differences between the LMC and the Galaxy.

3.3.2 Origin of IR emission in SNRs

As mentioned in previous sections, there are four sources of the IR emission in SNRs in general; ionic and/or molecular lines, thermal dust continuum emission, PAH bands, and non-thermal synchrotron emission (Koo et al. 2007, and references therein). Synchrotron emission is usually negligible except for a young PWN such as Crab. PAH emission has not been detected towards SNRs except N132D where it appears as a $15 - 20$ μm emission hump superposed on a strong dust continuum (Tappe et al. 2006). However, we cannot rule out the possibility that PAH features and plateau may contribute IR emission to evolved SNRs considerably. It is usually either the thermal emission from collisionally-heated dust grains in hot plasma or the forbidden lines from the elements such as Ne, O, Fe ions and pure rotational H_2 lines that dominate the emission in the IR band. Dust continuum often dominates IR emission at longer than $\sim$ 15 μm because dust temperature ranges from 40 to $\sim$ 100 K. In some cases such as SNR N49 or SNR 1E 0102.2–7219 in the Small Magellanic Cloud, however, it is known that ionic emission lines (e.g., [F II] 25.98

μm, [O IV] 25.88 μm) can significantly contribute MIR emission. Unlike the MIR bands, ionic/molecular line emission is usually a primary IR contributor in the NIR bands ($\leq$ 10 μm). Representative ionic emission lines are Brα 4.05 μm, [F II] 5.34 μm, and [Ar II] 6.99 μm, and there are various transitions of molecular hydrogen producing emission lines (e.g., pure rotational lines such as v = 0–0, S(19) 3.40 μm to S(3) 9.66 μm).

In order to distinguish between line- and dust-dominated SNRs, we can compare IR colors of a SNR to a theoretical prediction from the main emission mechanisms in a color-color diagram. Besides this, comparison of IR morphology to X-ray and optical can be an another useful means. When IR morphology is very similar to that of X-ray but optical, this might indicate that thermal dust emission is dominant in a SNR because, if the line radiation from a radiative shock is dominant, the IR morphology would be similar to the optical. However, in case of a Balmer-dominated SNR, resemblance between IR and optical often looks as good as that between IR and X-ray so that other physical conditions such as an age should be considered, too.

SNRs dominated by dust emission

Among the LMC SNRs previously detected in the IR bands, two Type Ia SNRs (0509–67.5 and 0519–69.0) and two core-collapse SNRs (N132D and SN 1987A) have been observed by the *Spitzer* IRS spectroscopy. SNR 0509–67.5 and 0519–69.0 are young, Balmer-dominated Type Ia SNRs. Their shocks are very fast ($\geq 3,000$ km/s) and non-radiative (Ghavamian et al. 2007), so that we do not expect strong IR ionic or molecular line emission. Their MIR emission is more likely to be from shock-heated dust grains, and the IRS spectra show no line emission in both SNRs (B. Williams et al. 2011). The MIR ($10 - 30$ μm) spectra of N132D and SN 1987A also show IR emission dominated by thermal dust continuum with small contribution from several ionic lines and PAH emission (Tappe et al. 2006; Bouchet et al. 2006; Dwek et al. 2008). Their *AKARI* MIR colors are consistent with these spectroscopic

results.

Three Type II SNRs, SNR 0450–68.5, N23, and N49B are middle-aged shell-type SNRs, and their MIR morphology are very similar to the X-rays whereas the Hα image hardly shows any shell structure (see Figure 2.4, and R. Williams et al. 1999; B. Williams et al. 2006). This suggests that their MIR emission are likely dominated by thermal dust emission. In the case of N49B, however, the bright portion of the southern shell and also the clump in the eastern part appear bright in Hα/[O III] emission (Mathewson et al. 1983), so there could be some contribution from ionic line emission. Also, one Type Ia SNR, DEM L71, shows good morphological correlation between IR and X-ray emission (Figure 2.4). Its optical emission is Balmer-dominated, and the IR emission from this remnant is likely to be dominated by dust emission.

Among the newly identified SNRs, DEM L238 is the only remnant that does not show any emission in the IRAC bands. This can suggest that the MIR emission is dominated by dust continuum although there could be line contribution considering its crude correlation between IR and optical morphologies. In the case of N103B, even though the IR emission of the knots originates from ionic lines, the shell seen at wavelengths longer than 24 μm is considered to be dominated by dust emission.

In summary, ten SNRs, five Type Ia (including two "prompt" Type Ia) and five core-collapse SNRs, are regarded to be dominated by thermal dust emission (Table 3.3.2. For those observed by *AKARI*, we fit their S11, L15, and L24 fluxes by a single-temperature dust emission and the results are summarized in Table 3.3. For this calculation, we first color-corrected the measured fluxes by assuming the modified blackbody curve (Equation 3.1). The correction factors range 0.8 – 1.1, 1.3 – 2.3, and 0.9 – 1.1 for the S11, L15, and L24, respectively. Note that the correction factors of the L15 band are large because the dust mass absorption coefficient, κ_ν, in the assumed model has a dip near 15 μm owing to the characteristic of the silicate. The derived temperatures vary from 86 to 185 K, which corresponds to the luminosity and mass ranges of $0.8 - 140 \times 10^{36}$ erg s^{-1} and $0.1 - 130 \times 10^{-4} M_\odot$. The

Table 3.2. Origin of dominant IR emission from SNRs

Origin	SNR	Total
Dust continuum	0453–68.5, DEM L71, N23, N103B, 0509–67.5	10
	0519–69.0, N132D, N49B, DEM L238, SN 1987A	
Ionic line	N11L, N49, N63A, DEM L241, N157B, DEM L316A/B, 0548–70.5	8
Molecular line	N86, DEM L256, SNR in N159, DEM L299	4
PAH	0450–70.9, SNR in N4, DEM L72, SNR in N206, DEM L249	5
Synchrotron	N158A	1

derived temperatures agree with the results derived from the *Spitzer* spectroscopy on the N132D and SN 1987A. For N132D, Tappe et al. (2006) applied a two-component fit to its *Spitzer* IRS spectrum of the southeastern rim to derive temperatures of 58 and 110 K. The higher temperature component contributes most of the emission at ≤ 30 μm. Our temperature (96 K) is somewhat lower than their 110 K, but this could be due to the lower-temperature component. For SN 1987A, Bouchet et al. (2006) and Dwek et al. (2008) showed that its *Spitzer* IRS spectrum is well described by a single-temperature thermal dust emission at ~ 180 K.

SNRs dominated by ionic/molecular line emission

The *Spitzer* IRS spectrum of N49 is found to be dominated by ionic lines from shocked gas without any substantial dust continuum emission (R. Williams et al. 2006). (There are some pure rotational H_2 lines too, but their contribution is relatively small.) This is interesting because the *AKARI* MIR colors of N49 is aligned close to those of thermal dust emission (Figure 3.3). We check the possibility that the MIR spectra of the positions where the spectroscopic observations were performed do not represent the spectrum of the entire SNR in N49. The spectroscopic observations were performed toward two positions, and their synthetic IRC colors

Table 3.3 Dust properties of five SNRs probably dominated by thermal dust emission

SNR	T(dust) (K)	L_{IR} (erg s^{-1})	Dust Mass ($M_\odot$)
0509–67.5	94 ± 3	8.1×10^{35}	$8.7 \pm 2.5 \times 10^{-5}$
0519–69.0	99 ± 4	4.5×10^{36}	$3.6 \pm 1.0 \times 10^{-4}$
N132D	96 ± 4	1.4×10^{38}	$1.3 \pm 0.3 \times 10^{-2}$
N49B	86 ± 3	1.6×10^{37}	$2.8 \pm 0.7 \times 10^{-3}$
SN 1987A	185 ± 15	3.6×10^{36}	$1.0 \pm 0.2 \times 10^{-5}$

are ($L15/L24$, $S11/L15$) = (0.41, 0.26) and (0.23, 0.28), respectively. For comparison, the observed IRC color of the entire SNR N49 is $\sim (0.45, 0.38)$, which is not significantly different from the synthetic ratio. The somewhat higher *S11/L15* ratio could be either due to variations of line intensities over the remnant or possibly due to dust emission. The important point is that *the SNRs dominated by ionic line emission can have colors similar to modified black bodies in the (L15/L24, S11/L15) diagram*. Important lines in these bands are [Ne II] 12.81 μm (S11), [Ne III] 15.56 μm (L15), [O IV] 25.90 μm and [Fe II] 26.00 μm (L24) lines. RCW 103 is far off from the modified black-body line apparently because its Ne lines are much stronger than O or Fe lines in contrast to N49.

For N11L and N63A are previously suggested to be ionic-line dominated based on their good spatial correlation between IR and optical emission (e.g., R. Williams et al. 2006). The IR shell morphology of N11L appears most clearly in the IRAC 4.5 μm band, which suggests Brα $\lambda 4.05 \mu$m can be relatively strong. In the case of N63A, bright IR emission is contributed by the three-lobed structure. Its IRS spectra show dominant ionic lines as well as several H_2 lines. The SNR also shows a complete shell in the 24 μm band like N49. The faint shell emission probably originates from dust emission, but the emission from the three lobes is more likely to dominate the whole

emission. As previously mentioned, N11L, N49, and N63A are known to be ionic-line dominated but have the IRAC colors for molecular shocks. Even though they are dominated by the ionic line emission, this does not mean that they are not related to molecular shocks, in other words, interacting with molecular clouds. In fact, the IRS spectra of N49 and N63A clearly show several transitional H_2 lines. Thus, we suggest that the low 3.6/5.8 ratios in the range for molecular shocks where these SNRs are located in Figure 3.4 is more likely to be mixture of ionic and molecular shocks, which is occasionally seen for SNRs interacting with molecular clouds (e.g., Chevalier 1999).

N157B is a middle-aged Crab-like SNR. As we described in §2.4, we have not detected any appreciable IR emission corresponding to the PWN, but detected IR emission corresponding to the Hα-emitting nebula in the east of the PWN both in MIR and NIR bands (Figure 2.2 and 2.3, also see R. Williams et al. 2006). The MIR emission is probably dominated by ionic lines.

Another Balmer-dominated SNR, 0548–70.4, is a mature Type Ia SNR ($\sim 7 \times 10^3$ yr, Hendrick et al. 2003). An interesting feature of this remnant is the X-ray emitting gas in the central region, where the bright MIR emission is detected by *AKARI* (Figure 2.2). It shows enhanced metal abundance and could be SN ejecta swept-up by reverse shock (Hendrick et al. 2003). On the other hand, there are bright Hα/[O III]-emitting clumps mixed with X-ray emitting gas, and they could be either dense ejecta or interstellar clumps swept up by slow, radiative shocks (e.g., Ghavamian et al. 2007). The brightness distribution of the MIR emission is considerably different from the X-rays. There are several bright clumps seen in the X-rays, and some of them are extended towards the south where there is no distinct MIR emission. Instead, the optical knots in the Hα images are mainly distributed inside of the central MIR emitting region. This remnant is also considerably off from the thermal dust-emission line in Figure 3.3. This suggests that the MIR emission in the central area is likely dominated by ionic lines from radiative shocks rather than by continuum emission from hot dusts.

For the other SNRs, the origins of the IR emission are categorized based on the IRAC color-color diagram (Figure 3.4). Since some SNRs dominated by ionic line emission are located at the low boundary of the IR color range for molecular shocks (i.e., $F_{3.6}/F_{5.8} \simeq 0.3$), SNRs showing higher $F_{3.6}/F_{5.8}$ than 0.3 are regarded to be molecular line dominated (N86, DEM L241 western region, DEM L256, north lobe of SNR in N159, and DEM L299). These SNRs usually show weak correlation with optical emission. Among SNRs with lower $F_{3.6}/F_{5.8}$ ratios, the remnants of which IR morphologies fairly correspond to the optical morphologies are classified as ionic line dominated SNRs (south shell of SNR in N159 and DEM L316A/B). Although the bright western region of DEM L241 shows the IRAC colors for molecular shocks, the entire shell-like structure seen in the 4.5 μm band well corresponds to that seen in optical (Figure A.8). This could suggest that the overall emission is dominated by ionic emission. Then, this remnant might be dominated by ionic emission and locally enhanced by molecular emission. In summary, eight SNRs are dominated by ionic line emission, and four are by molecular line emission. Also, note that there could be several SNRs possibly having both ionic and molecular line emission.

SNRs dominated by synchrotron emission

Since the flux of N158A is extracted only from its PWN, its NIR/MIR emission is expected to be dominated by synchrotron emission. Its IRS spectrum shows synchrotron emission dominating at shorter (IRAC) wavelengths as well as continuum at longer than 20 μm (B. Williams et al. 2008). The continuum is attributed to a warm dust component at a temperature of $\sim 50 - 65$ K, heated by PWN shocks. Moreover, there are several strong emission lines such as [Ne II], [Ne III], and [S III] at 12.81, 15.56, and 18.71 μm that can contribute the *AKARI* S11 and L15 bands. Then, the contribution of synchrotron and line emission could cause the difference from the blackbody line. Similarly, there are differences of its IRAC ratios from the theoretical calculation. This might result from the contribution of emission lines, for instance, [Fe II] λ5.34 μm and [Ar II] λ6.99 μm in the 5.8 and 8.0 μm bands,

respectively (see IRS spectrum in B. Williams et al. 2008), while there is no strong line contribution to the 3.6 and 4.5 μm bands.

SNRs dominated by PAH emission

The rest of the SNRs (SNR 0450–70.9, SNR in N4, DEM L72, SNR in N206, and DEM L249) are considered to be dominated by PAH emission based on the IRAC color-color diagram (Figure 3.4). These SNRs show lack of correlation to the optical images and are well defined in the 5.8 and 8.0 μm bands. DEM L249 is somewhat contentious since it has the IRAC colors expected for both ionic shocks and PAH emission. In terms of morphology, both IR and optical emissions show shell structures with the enhanced emission in the east (Figure A.9). However, the locations of the IR peaks along the eastern rim differ from those of the optical peaks, which is unlikely to be ionic line-dominated. We expect that further observations will enable us to clarify the origin of IR emission.

Application

Based on the IR origins reported previously or determined newly, their MIR colors are examined (Figure 3.5). Since the dust-dominated SNRs do not show detectable emission in the IRAC bands, they have evidently low F_8/F_{24} ratios (upper limits). On the contrary, those dominated by PAH emission have very high F_8/F_{24} ratios due to probably strong PAH features at $\sim 7-9$ μm. SNRs with ionic or molecular line emission are not clearly differentiated in this diagram, but SNRs dominated by molecular line emission tend to have higher F_8/F_{24} ratios. These trend could be related to the evolution of SNRs. As noticed in section 3.1.2, the mature SNRs are likely to have the high F_8/F_{24} ratios, whereas young SNRs are to have the low ratios. For the evolved SNRs, they become radiative and/or have interaction with ISM/CSM, so ionic/molecular line emission can be enhanced. Also, as SNR shocks become slower, PAHs could survive against destruction by shocks (see §4). The F_{24}/F_{70} ratio can be interpreted in similar way. Young SNRs can contain very

hot gas that heat dust grains by collisions. As hot gas cools down, however, the dust temperature decreases which results in a low F_{24}/F_{70} ratio.

The origin of the IR emission might be related to SN type. While core-collapse SNRs have contribution for line emission or PAH emission, Type Ia SNRs such as DEM L71, SNR 0509–67.5, and SNR 0519–69.0 are likely to be dominated by CSM/ISM dust emission. In fact, the three SNRs are Balmer-dominated Type Ia SNRs, which indicates that their shocks are fast and non-radiative. In that case, ionic and/or molecular line emission cannot be strong. Also, complete destruction of PAHs in the SNRs is expected by fast shocks. However, a Type Ia SNR that had more massive progenitor, so called a "prompt" Type Ia, might have IR emission originating from ionic/molecular emission lines. While general Type Ia SNRs are isolated from dense environments, prompt Type Ia SNRs can be located in dense ambient CSM as Kepler (Blair et al. 2007). The bright northwest filaments in Kepler are considered to be dominated by radiative emission from the shocked CSM, and a strong [Ar II] line is detected at 7.0 μm in the IRAC 8 μmband (Blair et al. 2007, and references therein). DEM L238 and DEM L249 are suggested to be evolved prompt Type Ia based on the X-ray spectral analysis (Borkowski et al. 2006a), which could be similar to Kepler. As previously mentioned, their IR morphologies show similarities with their optical morphologies in some degree, which could imply some contribution of emission lines from their ambient media. Moreover, a large amount of PAHs are known to be formed by an asymptotic giant branch star (e.g., Tielens 2008), and if dense CSM is present around DEM L249, PAH emission might be a dominant source of the observed IR emission. Further observations are required to reveal the origin of the IR emission and the existence of the dense CSM around the SNRs.

3.3.3 Dust heating & shock processing

As mentioned in the previous section, the IR emission mechanism (more precisely, dust continuum) is directly related to physical properties of the X-ray emitting gas. Dust is collisionally heated by electrons in a hot plasma and cools down radiatively.

Based on Dwek et al. (2008, and references therein), at a given size of a dust grain (a), the grain heating rate ($\mathcal{H}$) depends on electron density (n_e) and temperature (T_e) until electrons stop in the grain ($\mathcal{H} \propto n_e T_e^{3/2}$). Then, above a certain electron temperature (T_c), the heating rate only depends on the electron density ($\mathcal{H} \propto n_e$). The radiative cooling rate ($\mathcal{L}$) simply follows the Stefan-Boltzmann law, which gives $\mathcal{L} = \pi a^2 \sigma T_d^4 \langle \mathcal{Q} \rangle$, where σ is the Stefan-Boltzmann constant, T_d is dust temperature, and $\langle \mathcal{Q} \rangle$ is the averaged dust emissivity. When dust is in thermal equilibrium (i.e., $\mathcal{H} = \mathcal{L}$), dust temperature is proportional to $n_e^{0.17-0.2}$ and $T_e^{0.25-0.3}$ at $T_e \leq T_c$ and to only $n_e^{0.17-0.2}$ at $T_e \geq T_c$ (Dwek et al. 2008).

Figure 3.13 depicts the equilibrium temperature of a single-sized silicate grain ($a = 0.03$ μm) that has a critical temperature of 5×10^5. Contours in the figure are actually simplified, and the original calculation can be found in Figure 1 of Dwek et al. (2008). The positions of the LMC SNRs are superposed based on their plasma properties from literatures. To derive electron density and temperature, it is necessary to model the observed X-ray spectra, which usually requires various input parameters. Since no coherent study about plasma properties of the LMC SNRs has been done, methods of the model calculation can differ among literatures. Moreover, literatures do not always give the explicit electron density. Instead, an ionization timescale defined as $\tau = n_e \times t$ (cm^{-3} s) is often provided. In those case, we derive the density using an ionization age (or SNR age). Also, the density is sometimes given to be proportional to a volume filling factor ($\sim f^{-0.5}$). We take a f-factor from the literature if a preferential value is given, otherwise, we just assume $f = 1$. Detailed information of electron density and temperature for LMC SNRs is summarized in Table 3.4. As a comparison, four Galactic SNRs are shown in Figure 3.13. Their X-ray properties are taken from Bamba et al. (2005) for the Cas A and Kepler, Hwang & Gotthelf (1997) for Tycho (*ASCA* data), and Miceli et al. (2006) for W49B south (*XMM-Newton* data).

It is interesting to examine the correlation between IR properties and X-ray properties in the figure. We show *Spitzer* 24/70 μm ratios of LMC SNRs and Galactic

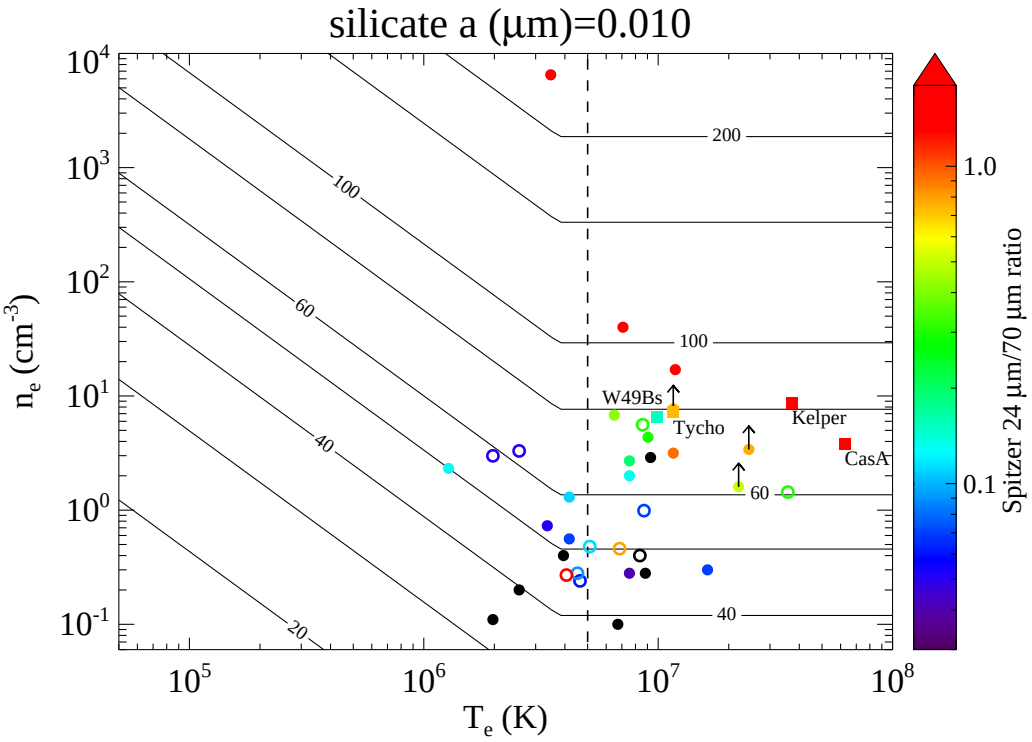

Figure 3.13 Equilibrium temperature as a function of electron density and temperature for silicate grains with a size of 0.01 μm. This figure mimics Figure 1 of Dwek et al. (2008) in a simple way. A critical temperature ($T_e \sim 5 \times 10^6$ K) where dust temperature only depends on electron density is marked (*dashed line*). Positions of LMC SNRs are overlaid based on X-ray observations. Electron densities and temperatures are listed in Table 3.4. As a comparison, four Galactic SNRs (Cas A, Kepler, Tycho, and W49B) are also plotted (*sqaure*). Filled and open symbols designate SNRs with good and bad morphological correlations between IR and X-ray emission, respectively. Black filled circles represent LMC SNRs without detected IR emission. The color of a symbol represents a ratio of *Spitzer* 24 μm to 70 μm as notified in a color bar. Note that *AKARI* 24 and 65 μm fluxes are used for the IR ratio of Tycho.

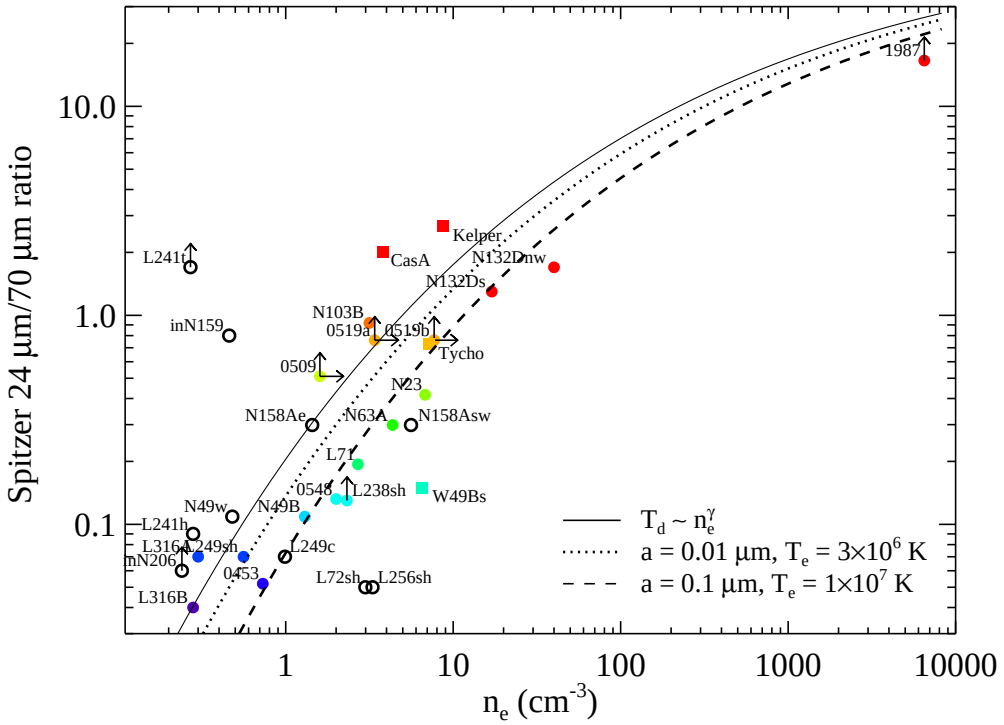

Figure 3.14 Correlation between *Spitzer* 24/70 ratios and electron densities of LMC SNRs. As a comparison, four Galactic SNRs (Cas A, Kepler, Tycho, and W49B) are also plotted (*sqaure*). Symbol designation and colors of symbols are the same as Figure 3.13, but note that only filled symbols (i.e., good spatial correlation between IR and X-ray emission) are colored for emphasis. Theoretical 24/70 ratios are also overlaid assuming $T_{dust} \sim n_e^\gamma$ (*solid line*), grain size $a = 0.01$ μm at $T_e = 3 \times 10^6$ K (*dotted line*), and grain size $a = 0.1$ μm at $T_e = 1 \times 10^7$ K (*dashed line*).

SNRs using colors of symbols. The IR fluxes of the Galactic SNRs are from Hines et al. (2004) for Cas A, Blair et al. (2007) for Kepler, Ishihara et al. (2010) for Tycho (*AKARI* 24 and 65 μm fluxes), and Pinheiro Gonçalves et al. (2011) for W49B. There is a tendency that SNRs with high 24/70 ratios have high equilibrium temperatures while those with low 24/70 ratios do low equilibrium temperatures. This is predictable because dust continuum has a peak at a shorter wavelength as dust temperature increases. In some cases that SNRs have high 24/70 ratios but low equilibrium temperatures or vice versa, their IR morphologies are inconsistent with the X-ray morphologies. This implies that their IR emission might be contributed by other IR emission mechanisms. In addition, SNRs without detectable IR emission usually have lower equilibrium temperatures ($\leq$ 50 K). Even if there is dust continuum at such a low temperature, it could be too faint to be detected currently at 24 (and 70) μm. Although electron densities have some uncertainties depending on the model calculations and their assumptions, it is suggested that the plasma properties can be a good indicator of IR visibility.

We directly compare 24/70 ratios with electron densities (Figure 3.14). It is found that the ratios are well correlated with the electron densities, particularly for the SNRs showing good spatial association between IR and X-ray emission. As predicted in §3.2.1, this correlation indicates the dependency of dust emission to gas density even more clearly than Figure 3.8. Using the relation between dust temperature and X-ray properties, the 24/70 ratio can be theoretically calculated using Equation 3.1 as $F_{24}/F_{70} = \kappa_{24}B_{24}(T_d)/\kappa_{70}B_{70}(T_d)$. When electrons go through grain (i.e., sufficiently hot gas), dust temperature only depends on electron density ($T_{dust} \simeq 57 \times n_e^{0.17}$, *solid line* in Figure 3.14). When electrons stop in grain, dust temperature depends on electron density as well as grain size and electron temperature. We examine two cases ($a = 0.01$ μm at $T_e = 3 \times 10^6$ K and grain size $a = 0.1$ μm at $T_e = 1 \times 10^7$ K). The three analytical relations indeed well describe the observed trend, and it seems that grain size of 0.1 μm can explain the observation most similarly.

Table 3.4. Properties of X-ray emitting plasma in LMC SNRs

SNR	n_e[a] (cm^{-3})	T_e (keV)	IR[b] correlation	Note	Refs.
0453–68.5	0.73	0.29	0		1
SNR in N9	0.40	0.34	2	Average n_e of several regions	2
N186D	0.1	0.58	2		3
DEM L71	2.7	0.65	0		4
N23	6.8	0.56	0		1
DEM L72sh	2.99	0.17	1	Shell	5
DEM L72h	0.11	0.17	2	Hot center	5
N103B	3.16	1.0	0	Overall value of kT and n_e	6
0509–67.5	1.6	1.9	0		4
0519–69.0a	3.4	2.1	0	Fainter portion of SNR	4
0519–69.0b	7.7	1.0	0	Three bright knots	4
N132D NW	40	0.61	0		1
N132D S	17	1.02	0		1
N49B	1.3	0.36	0		1
N49 E	0.48	0.44	0	Average of eastern region	7
SNR in N206	0.24	0.4	1	Hot gas region	8
0534–69.9	0.28	0.76	2	Average of central region	9
DEM L238sh	2.32	0.11	0	Shell	10
DEM L238c	2.89	0.8	2	Central region	10
SNR 1987	6500	0.3	0		11
N63A	4.35	0.78	0		12
DEM L241h	0.28	0.39	1	Head region of diffuse emission	13
DEM L241t	0.27	0.35	1	Tail region of diffuse emission	13
DEM L249sh	0.56	0.36	0	Shell	10
DEM L249c	0.99	0.75	1	Central region	10
DEM L256sh	3.30	0.22	1	Shell	5
DEM L256c	0.2	0.22	2	Hot center	5
N157B	0.40	0.72	1		14

Table 3.4 (cont'd)

SNR	n_e[a] (cm^{-3})	T_e (keV)	IR[b] correlation	Note	Refs.
SNR in N159	0.46	0.59	1		15
N158A E	1.44	3.08	1	Eastern region	16
N158A SW	5.6	0.74	1	Bright southwestern region	16
DEM L316B	0.28	0.65	0		17
DEM L316A	0.30	1.4	0		17
0548–70.4	2.0	0.65	0		4

[a]In some literatures, an ionization timescale (τ) is given instead of an explicit electron density. In those cases, n_e is derived from $\tau = n_e \times t$ in this work. The value of t used for the estimation is explained in each reference. Also, some literatures give an expression of n_e proportional to a volume filling factor (f). If a preferential f is given, we adopt it or, otherwise, assume $f = 1$.

[b]Morphological correlation between IR emission and X-ray emission (0: consistent, 1: inconsistent, 2: no IR emission detected)

References. — [1] B. Williams et al. (2006, and references therein); [2] Seward et al. (2006); [3] Jaskot et al. (2011): using an ionization age of 11,000 yr; [4] Borkowski et al. (2006a, and references therein); [5] Klimek et al. (2010): *XMM-Newton* data; [6] Lewis et al. (2003): using $t \sim 1000$ yr; [7] Park et al. (2003): using a dynamical age of 6,600 yr ; [8] R. Williams et al. (2005): assuming a volume filling factor as unity ($f_{hot} = 1$); [9] Hendrick et al. (2003): with maximum mixing; [10] Borkowski et al. (2006b): using the SNR ages ($t_{\rm SNR}$, DEM L238: 13,500 yr, DEM L249: 12,500 yr); [11] Dwek et al. (2008); [12] Warren et al. (2003): using the SNR age of 3,500 yr; [13] Bamba et al. (2006): *XMM-Newton* data; [14] Chen et al. (2006): using an ionization age of 2,000 yr with $f = 1$; [15] Seward et al. (2010): adopting $f = 0.3$; [16] Park et al. (2010): assuming $f = 1$; [17] R. Williams & Chu (2005)

SNR shocks are the main source of dust destruction. Dust grains are destroyed by sputtering and grain-grain collisions behind the shock (Jones 2004). Recently, Borkowski et al. (2006a) and B. Williams et al. (2006) observed Type Ia and core-collapse SNRs using *Spitzer*, respectively. They found that the dust destruction by sputtering is necessary to reproduce the observed 70/24 μm ratios according to their shock model calculation. They concluded that about 40% of the mass in dust grains has been destroyed and smaller grains ($\leq$ 0.04 μm) has been shattered up to 90% in both types of SNRs.

We note that the dust temperatures derived from the *AKARI* S11, L15, and L24 fluxes are considerably higher than those of Borkowski et al. (2006a) and B. Williams et al. (2006). If we calculate the 70/24 μm flux ratios using our dust temperature, the ratios are significantly smaller than the *Spitzer* results. This is shown in Figure 3.15 which is a color-color diagram of *AKARI L15/L24* versus *Spitzer* 24/70 μm. *Spitzer* 24/70 μm ratios are adopted from literatures (Borkowski et al. 2006a; B. Williams et al. 2006; R. Williams et al. 2006). It is clear that a single temperature cannot describe the full spectral energy distribution (SED) of these SNRs including the ones probably dominated by thermal dust emission. It is interesting that N49 and 0548–70.4, two SNRs thought to be line-dominated, deviate more largely from the dust-continuum curve. From previous studies, it is known that the SED of SNRs usually requires two components, cold and warm dusts. We can also explain the color of SNRs in Figure 3.15 with an extra cold component at $20-40$ K and with the mass ratio to the warm component of $50-1000$. The lines in the figure show the cases when the temperature of the cold component is 30 and 40 K and the mass ratio is 500. The colors of the line-dominated SNRs, however, cannot be easily described by an extra cold component. We can fit their colors using a cold component ($30-40$ K) plus a warm component ($100-150$ K) with a mass ratio of $\sim$ 10000. But, since both SNRs are middle-aged, the temperature of the warm component appears too high for them. This supports our conclusion that these SNRs are line-dominated. The strong ionic lines around 70 μm are [O I] 63 μm and [O III] 88 μm which might

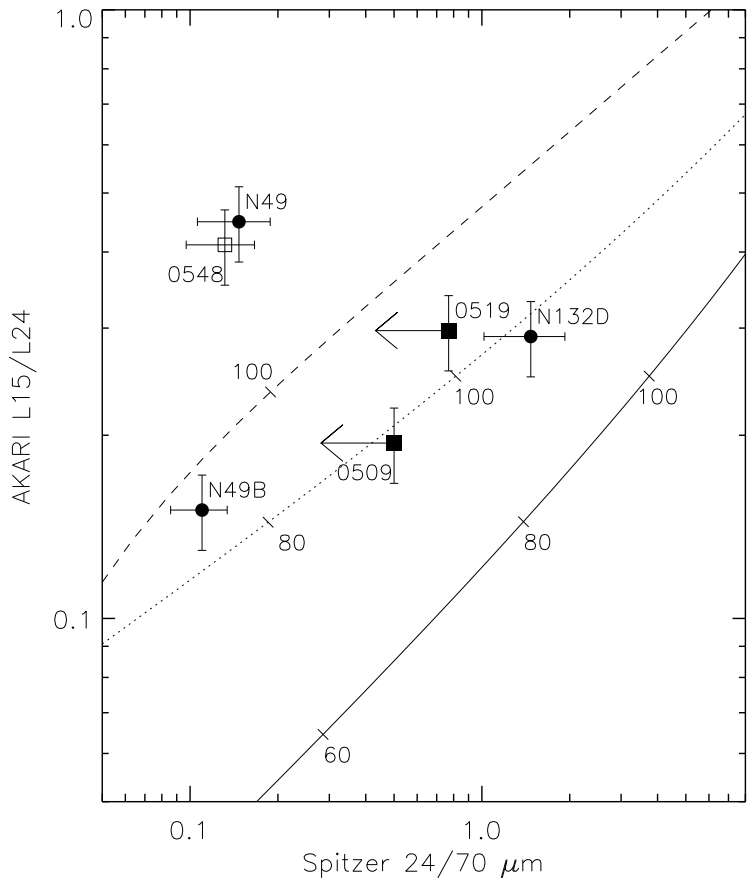

Figure 3.15 *AKARI L15/L24* flux ratio versus *Spitzer* 24/70 μm flux ratio. Solid line represents the expected ratios from modified black body curve of thermal dust emission with a single component. Dotted and dashed lines show the ratios of two-component dust emission with T_{cold} = 30 and 40 K, respectively when $M_{cold}/M_{warm} = 500$ (see text for detail).

have led the 24/70 μm ratio to decrease. This might indicate that the discrepancy is to some extent due to the line emission.

Multiple dust temperatures could happen if the ambient ISM is clumpy, so that the shock velocities and therefore dust temperatures differ for the clump and inter-clump medium as suggested by Tappe et al. (2006) in N132D. It can also happen if the grains size distribution does not follow a simple power law. In this regard, it is worth to note that previous IRAS studies showed that the IR emission from SNRs usually require two components; cold components dominating $\geq$ 70 μm and warm component dominating $\leq$ 25 μm (Arendt 1989; Saken et al. 1992). Figure 3.15 is consistent with previous IRAS results, and suggests that the 70 μm fluxes in these SNRs might be dominated by cold dust component. This result implies that the destruction rate of grains in these SNRs may not be as high as previously estimated from the 24/70 μm flux ratios.

Bibliography

Appleton, P. N., Fadda, D. T., Marleau, F. R., et al. 2004, ApJS, 154, 147

Arendt, R. G. 1989, ApJS, 70, 181

Banas, K. R., Hughes, J. P., Bronfman, L., & Nyman, L.-A. 1997, ApJ, 480, 607

Bamba, A., Ueno, M., Nakajima, H., Mori, K., & Koyama, K. 2006, A&A, 450, 585

Bamba, A., Yamazaki, R., Yoshida, T., Terasawa, T., & Koyama, K. 2005, ApJ, 621, 793

Blair, W. P., Ghavamian, P., Long, K. S., et al. 2007, ApJ, 662, 998

Borkowski, K. J., Williams, B. J., Reynolds, S. P., et al. 2006, ApJ, 642, L141

Boyle, B. J., Cornwell, T. J., Middelberg, E., et al. 2007, MNRAS, 376, 1182

Bouchet, P., Dwek, E., Danziger, J., et al. 2006, ApJ, 650, 212

Chen, Y., Wang, Q. D., Gotthelf, E. V., et al. 2006, ApJ, 651, 237

Chevalier, R. A. 1999, ApJ, 511, 798

Desai, K. M., Chu, Y.-H., Gruendl, R. A., et al. 2010, AJ, 140, 584

Dickel, J., McIntyre, V., Gruendl, R., & Milne, D. 2005, AJ, 129, 790

Dwek, E., Arendt, R. G., Bouchet, P., et al. 2008, ApJ, 676, 1029

Dwek, E., Foster, S. M., & Vancura, O. 1996, ApJ, 457, 244

Dwek, E. 1987, ApJ, 322, 812

Dwek, E., Petre, R., Szymkowiak, A., & Rice, W. L. 1987, ApJ, 320, L27

Fukui, Y., Mizuno, N., Yamaguchi, R., Mizuno, A., & Onishi, T. 2001, PASJ, 53, L41

Ghavamian, P., Blair, W. P., Sankrit, R., Raymond, J. C., & Hughes, J. P. 2007, ApJ, 664, 304

Ghavamian, P., Long, K. S., Blair, W. P., et al. 2012, ApJ, 750, 39

Green, D. A. 2009, Bulletin of the Astronomical Society of India, 37, 45

Hendrick, S. P., Borkowski, K. J., & Reynolds, S. P. 2003, ApJ, 593, 370

Hines, D. C., Rieke, G. H., Gordon, K. D., et al. 2004, ApJS, 154, 290

Hwang, U., & Gotthelf, E. V. 1997, ApJ, 475, 665

Ishihara, D., Kaneda, H., Furuzawa, A., et al. 2010, A&A, 521, L61

Jones, A. P. 2004, in ASP Conf. Ser. 309, Astrophysics of Dust, ed. A. N. Witt, G. C. Clayton and B. T. Draine. (San Fransisco:ASP), 347

Koo, B.-C., Lee, H.-G., Moon, D.-S., et al. 2007, PASJ, 59S, 455

Manchester, R. N., Gaensler, B. M., Wheaton, V. C., et al. 2002, PASA, 19, 207

Mathewson, D. S., Ford, V. L., Dopita, M. A., et al. 1983, ApJS, 51, 345

Miceli, M., Decourchelle, A., Ballet, J., et al. 2006, A&A, 453, 567

Micelotta, E. R., Jones, A. P., & Tielens, A. G. G. M. 2010a, A&A, 510, A36

Neufeld, D. A., Hollenbach, D. J., Kaufman, M. J., et al. 2007, ApJ, 664, 890

Oliva, E., Moorwood, A. F. M., Drapatz, S., Lutz, D., & Sturm, E. 1999, A&A, 343, 943

Panagia 1999, in IAU Symp. 190, New Views of the Magellanic Clouds, ed. Y.-H. Chu, N. Suntzeff, J. Hesser, and D. Bohlender (San Francisco: ASP), 549

Park, S., Burrows, D. N., Garmire, G. P., et al. 2007, AIPC, 937, 43

Park, S., Hughes, J. P., Slane, P. O., et al. 2003, ApJ, 592L, 41

Pinheiro Gonçalves, D., Noriega-Crespo, A., Paladini, R., Martin, P. G., & Carey, S. J. 2011, AJ, 142, 47

Pei, Y. C. 1992, ApJ, 395, 130

Reach, W. T., Rho, J., Tappe, A., et al. 2006, AJ, 131, 1479

Saken, J. M., Fesen, R. A., & Shull, J. M. 1992, ApJS, 81, 715

Tappe, A., Rho, J., & Reach, W. T. 2006, ApJ, 653, 267

Tielens, A. G. G. M. 2008, ARA&A, 46, 289

Weingartner, J. C., & Draine, B. T. 2001, ApJ, 548, 296

Welty, D. E., Frisch, P. C., Sonneborn, G., & York, D. G. 1999, ApJ, 512, 636

Williams, B. J., Borkowski, K. J., Reynolds, S. P., et al. 2011, ApJ, 729, 65

Williams, B. J., Borkowski, K. J., Reynolds, S. P., et al. 2006, ApJ, 652, 33

Williams, R. M., Chu, Y.-H., & Gruendl, R. 2006, AJ, 132, 1877

Williams, R. M., Chu, Y.-H., Dickel, J., et al. 1999, ApJ, 514, 798

Wong, T., Hughes, A., Ott, J., et al. 2011, ApJS, 197, 16

Chapter 4

PAH emission in the SNR N49

4.1 Introduction

Over the past 20 years, various researches on polycyclic aromatic hydrocarbon (PAH) in interstellar medium (ISM) have been conducted both observationally and theoretically. PAHs are revealed as abundant, ubiquitous, and dominant in the ISM of galaxies (Tielens 2008, and references therein), and one of the main resources of infrared (IR) emission from near- to mid- IR wavebands. There have been a number of observations to show a variety of PAH features at different wavelengths. Several major emission features are usually detected in diverse objects such as the 3.3 μm C–H stretching band, the 6.2 and 7.7 μm C–C stretching bands, and the 8.6 and 11.3 μm C–H in- and out-of-plane bending bands.

In PAH processing, interstellar shocks are known to play a crucial role. It is largely accepted that PAHs could be either the remaining dust condensation nuclei that escaped the grain growth process in asymptotic giant branch ejecta or the fragmentation of dust grains through shattering collision in fast interstellar shocks (e.g., Tielens 2008; Jones et al. 1996). Also, interstellar shock waves have been considered as one of the main mechanisms to destroy PAH molecules. In spite of plentiful observations of PAH features, however, there are still unanswerable questions on the role

of interstellar shocks in the evolution of PAHs. Particularly, how supernova shocks affect PAH molecules is barely explored. Detection of PAH features in supernova remnants (SNRs) is unexpectedly rare, recalling that the one of their formation process is related to interstellar shocks.

There have been considerable literatures dealing with the survivability of PAH molecules in shocked environments. In particular, since PAH emission has been categorized as one of the IR emission components expected for SNRs based on the *Spitzer* imaging data (Reach et al. 2006), substantial efforts have been made in order to search for observational evidence of PAH emission in SNRs. By using *Spitzer* Infrared Spectrograph (IRS) observations, Tappe et al. (2006) firstly reported the detection of $15-20$ μm hump attributed to C–C–C bending modes of large PAHs ($\sim$ 4000 C-atoms) with the weakly detected 11.3 μm PAH feature in SNR N132D, which is located in the Large Magellanic Cloud (LMC). Based on the lack of PAH features at $6-9$ μm and the large ratio of the $15-20$ μm hump to the 11.3 μm feature, they interpret that small PAHs are rapidly destroyed by thermal sputtering in the supernova blast wave. Among the *Spitzer* IRS spectra of several galactic SNRs, some in Neufeld et al. (2007) and Hewitt et al. (2009) also show the major PAH features with strong ionic and/or molecular lines, yet both authors have not mentioned the association of the features with the SNRs in the papers. In most cases that PAH emission is observed in SNRs, no convincing evidence for the PAH emission intrinsic to the SNRs has been reported. This lack of detection of PAH features in SNRs results from the difficulty of discrimination between PAH emission from SNRs and that from other back/foreground sources.

In this respect, the LMC staying away from the galactic disk, could be the best place to observe PAH emission from SNRs. Moreover, since PAH molecules in shock regions are supposed to be able to survive only in those with dense clumps (Micelotta et al. 2010a), SNRs interacting with dense circumstellar or interstellar material would be good candidates for detecting PAH emission. Thus, we have targeted an IR-bright SNR, N49 with *AKARI* infrared space telescope (Murakami et

al. 2007). SNR N49 (SNR 0525–66.1) is one of the SNRs interacting with ambient molecular clouds in the LMC. It is a middle-aged SNR ($\sim$ 6600 yr, Park et al. 2003), and the surrounding dense ambient medium including complex filamentary structures suggests that the progenitor of the SNR is a B-type star without a strong stellar wind (Shull 1983). Thanks to its sufficient brightness at almost all wavelengths, this remnant has been studied by various observations at multi wavelengths; X-ray (Park et al. 2003), ultraviolet (UV) (Blair et al. 2000), optical (Vancura et al. 1992; Bilikova et al. 2007), IR (R. Williams et al. 2006; Seok et al. 2008), and radio (Dickel & Milne 1998; Dickel et al. 1995). The observational results have shown not only complex filamentary morphology in both optical and IR wavebands, but also a complete shell-type structure in X-ray and radio. By CO observations (Banas et al. 1997), N49 is suggested to be interacting with its nearby molecular cloud at southeast, which is thought to be responsible for mostly asymmetric morphology and brightness enhancement toward southeast seen at all wavelengths. We present the near-IR (NIR) spectra of N49 in the unprecedented wavelength range ($\sim 2.5 - 5$ μm) and report the first detection of an aromatic feature at 3.3 μm in SNRs.

4.2 Observations

We performed spectroscopic observations of N49 using the Infrared Camera (IRC; Onaka et al. 2007) on board *AKARI*. These observations are part of the several *AKARI* mission programs, and the details of the observations are listed in Table 4.1. The data were taken with a grism in the IRC NIR channel, NG ($2.5 - 5$ μm), in the common mode of slit spectroscopy (Ns) during the post He phase (cooled by the onboard cryocooler). The dispersion (wavelength increment per pixel) is ~ 0.01 μm, and the slit width is $5''$, which gives a spectral resolution of $R \sim 100$ at 3 μm (Onaka et al. 2007). As a coarse spectral mapping, we made fourteen pointed observations to N49 covering a bright wedge-shaped feature in the east as well as relatively IR faint region at west. In order to obtain a background spectrum, we also

carried out two independent observations toward neighbor regions avoiding diffuse emission from the remnant. Figure 4.1 shows the positions of the IRC NG/Ns slits superposed on the IRC N3 band ($2.7 - 3.8$ μm) image that was taken in part of the *AKARI* large-scale survey of the LMC (PI: T. Onaka, Ita et al. 2008). The total integration time is ~ 396 s for each pointed observation.

The data were reduced by using the standard IDL package for the IRC spectroscopy data reduction (toolkit version 20090211, Ohyama et al. 2007). General preprocesses such as dark subtraction and linearity correction were applied during the pipeline. For N49, the extraction apertures of the final spectra are determined for areas observed with more than one slit positions, and finally five regions, named "P1" to "P5" from east to west, are chosen as marked in Figure 4.1 (white rectangles). To extract each spectrum, we integrated 21 pixels along the slit for source spectra (except P5) and 17 pixels for background spectra, corresponding to about $31''$ and $25''$, respectively. For the P5 spectrum, we extracted it from a shorter aperture (13 pixels corresponding to $19''$) in order to avoid low surface brightness regions. The center and the length of extraction were determined to maximize the signal-to-noize ratio (S/N), to avoid contamination from any point sources, and to average the resultant spectra in the overlapping region for the final spectra. The final spectra including the background spectrum are shown in Figure 4.2. Since the background spectrum does not show any line or continuum emission, we did not subtract it from the final spectra to not degrade the S/N.

4.3 IR spectrum of N49

4.3.1 *AKARI* IRC NG spectrum

We examined the IRC NG spectra for the SNR N49, and the detected lines are given in Table 4.2. The MIR emission in N49 is dominated by ionic line emission (R. Williams et al. 2006). However, there is no strong ionic line within this IRC NG wavelength coverage, so that we could not detect any ionic lines except marginal

Table 4.1. Summary of Observations for N49

Obs. ID	Sub. ID	Program[a]	Date	Field center R.A. (J2000)	Field center Dec. (J2000)	Note[b]
			<N49>			
1420813	1	ISMGN	2008 Jun 12	05:26:12.1	-66:05:26.8	BG
1420813	2	ISMGN	2008 Jun 23	05:26:12.2	-66:05:27.3	BG
1420925	1	ISMGN	2008 Jul 10	05:26:04.9	-66:05:12.2	P2
1420926	1	ISMGN	2008 Jul 08	05:26:03.8	-66:05:00.9	P3
1420926	2	ISMGN	2008 Jul 08	05:26:04.0	-66:04:56.7	P3
1421925	1	ISMGN	2008 Jul 10	05:26:05.7	-66:05:16.6	P1
1421925	2	ISMGN	2008 Jul 10	05:26:05.5	-66:05:14.7	P1
1421926	1	ISMGN	2008 Dec 20	05:26:02.6	-66:05:04.5	P4
1900451	1	P3LMC	2008 Jun 25	05:26:04.6	-66:05:13.8	P2
1900452	1	P3LMC	2008 Dec 25	05:26:03.4	-66:05:12.1	P3
1910233	1	LMCNG	2009 Dec 11	05:25:58.9	-66:05:16.1	N
1910233	2	LMCNG	2009 Dec 12	05:25:56.8	-66:06:15.4	N
1910233	3	LMCNG	2009 Dec 12	05:26:00.6	-66:05:08.7	P5
1910234	1	LMCNG	2009 Dec 13	05:26:00.3	-66:05:13.4	P5
1910234	2	LMCNG	2009 Dec 13	05:26:00.5	-66:05:18.9	P5
1910234	3	LMCNG	2009 Dec 15	05:26:00.6	-66:05:11.1	P5

[a]Name of the *AKARI* mission programs: "ISM in our Galaxy and nearby galaxies" (ISMGN, PI: H. Kaneda), "Observations of the Magellanic Cloud" (P3LMC, PI: T. Onaka), and "Near infrared spectroscopic observations of red objects in the Large Magellanic Cloud" (LMCNG, PI: T. Onaka).

[b]Classification of the final spectra after averaging separate spectra extracted from overlapping region in N49. Spectra with the same note are used for one final spectrum. BG: background spectrum, P1–P5: source spectra extracted from five different regions, respectively (see Figure 4.1). N: spectrum not used for the final spectra owing to either a single observation under a poor detector condition or a wrong pointing.

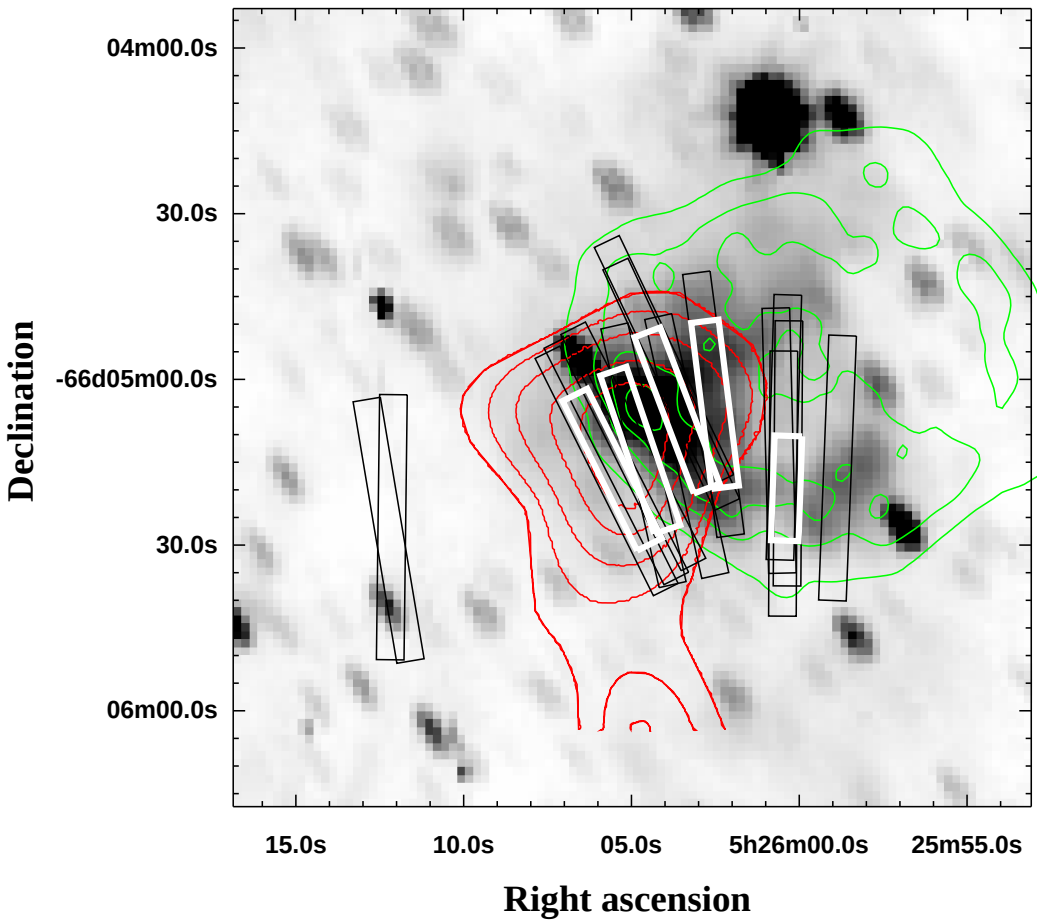

Figure 4.1 Positions of the IRC NG/Ns slits superposed on the *AKARI* N3 image of N49. Thirteen on-positions and two background positions are observed (*black*). We also mark where final averaged spectra are extracted (*white*). The five final spectra are referred to as "P1" to "P5" from east to west, respectively (see Figure 4.2). For comparison, contours showing 6-cm radio continuum (*green*) and CO emission (*red*) are superposed. The radio data are from Dickel & Milne (1998); the levels are at 2, 4, 6, 8, and 10 mJy beam^{-1}. The CO contours are taken from Figure 5 of Banas et al. (1997); the levels are at 1.0, 1.3, 1.7, 2.0, 2.3, and 2.7 K km s^{-1}.

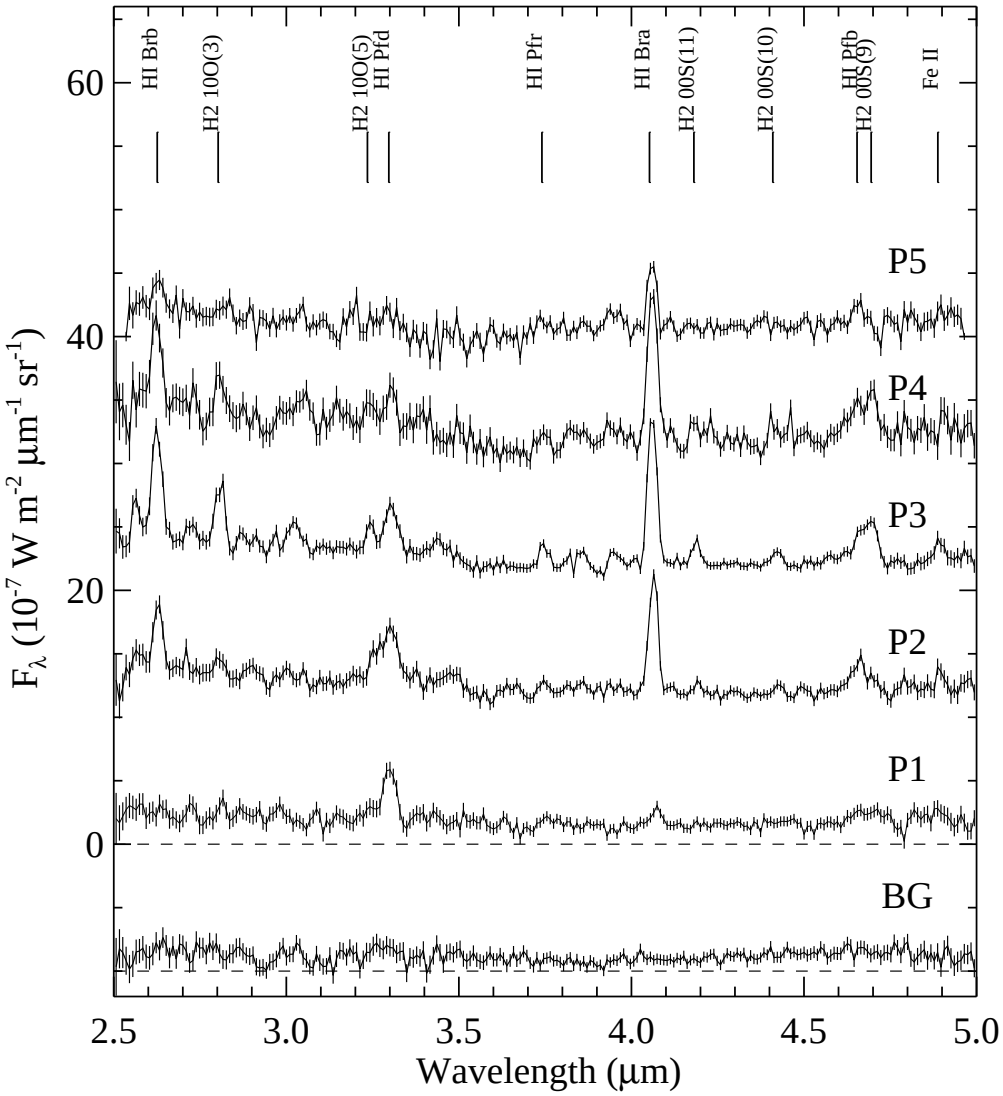

Figure 4.2 Final spectra of N49 together with the background spectrum. For convenience, the spectra are shifted by 1, 2, 3, and 4 $\times 10^{-6}$ W m^{-2} μm^{-1} sr^{-1} for P2 to P5, respectively. Background spectrum is shown in the bottom (shifted by -1 $\times 10^{-6}$ W m^{-2} μm^{-1} sr^{-1}). Noticeable lines are labeled at their vacuum wavelengths.

detection of [Fe II] λ 4.889 μm. The most prominent lines are hydrogen recombination lines such as Brα λ 4.052 μm and Brβ λ 2.626 μm, which are seen at all spectra except spectrum P1 (Figure. 4.2). Since P1 is extracted from just outside of the bright Hα region, there is no strong recombination line emission but only an interesting feature at 3.3 μm (see next). Although H_2 molecular lines are not as distinct as the recombination lines, several rotational lines such as H_2 1-0 O(3) and 0-0 S(11) lines are also clearly detected.

For the lines detected in most spectra, we measured their intensities by fitting Gaussians with linear baselines. The intensities with uncertainties are given in Table 4.2. The uncertainties are the 1 σ errors from the line fits, and the upper limits at 2 σ level are given if the line emission is not apparent. Most lines in Table 4.2 are not blended with others, yet there are two cases (i.e. H_2 1-0 O(5), Pfδ at 3.235, 3.297 μm and Pfβ, H_2 0-0 S(9) at 4.654, 4.695 μm) that two lines are located close to each other. For those cases, we applied two Gaussian fits to estimate their intensities together with either the peak wavelength or the full width at half maximum (FWHM) fixed if necessary. In addition, we fixed peak wavelengths or FWHMs for a few relatively weak lines.

In the case of P1 to P3 spectra, we notice that the feature at 3.3 μm could largely originate from the well-known aromatic C-H stretching transition at 3.3 μm rather than Pfδ at 3.297 μm. In order to be attributable to Pfδ emission, its intensity is abnormally stronger than theoretical value ($\leq$ 10% of Brα intensity in Case B) while the other Brβ and Pf lines are generally consistent with the expected values (see Table 4.2). Moreover, the intensities of the 3.3 μm feature do not vary with Brα intensities (see Fig. 4.2), and the measured widths of the feature appear to be wider (FWHM $\sim 0.04 - 0.05$ μm) than those of other ionic/molecular lines (FWHM $\sim$ 0.03 μm on average) that corresponds to the instrumental width (Onaka et al. 2007). These widths are consistent with the typical width ($\sim$ 0.04 μm) of the 3.3 μm aromatic emission (van Diedenhoven et al. 2004). Hence, we consider that the 3.3 μm feature mainly arises from the aromatic hydrocarbon emission due to

Table 4.2. Detected lines and their intensities from *AKARI* Data for N49

		Intensity (10^{-8} W m^{-2} sr^{-1})				
Line ID	λ_{ref}[a]	P1	P2	P3	P4	P5
Brβ	2.626	$\leq$0.34	1.58±0.30	2.73±0.27	2.47±0.53	0.77±0.34
H_2 1-0 O(3)	2.803	0.27±0.15[b]	0.31±0.25	1.38±0.23	0.85±0.40	$\leq$0.47
H_2 1-0 O(5)	3.235	0.32±0.15[b]	0.75±0.38	0.58±0.12[b]	0.42±0.24[b]	$\leq$0.57
Pfδ+PAH[c]	3.297	1.72±0.31[d]	2.16±0.51	1.42±0.25[d]	0.79±0.37[d]	$\leq$0.73
PAH[e]	3.300	1.67±0.35	1.87±0.53	1.04±0.28	0.39±0.45	—
PAH[f]	3.400	—	0.61±0.36[f]	0.80±0.34[f]	—	—
Pfγ	3.741	$\leq$0.24	0.22±0.09[b]	0.51±0.13	$\leq$0.44	$\leq$0.45
Brα	4.052	0.50±0.16	2.94±0.15	3.83±0.13	4.03±0.25	1.52±0.17
H_2 0-0 S(11)	4.181	$\leq$0.09	0.23±0.08[b]	0.50±0.11	0.42±0.14[b]	$\leq$0.48
H_2 0-0 S(10)	4.410	$\leq$0.20	0.20±0.09[b]	0.35±0.14	$\leq$0.51	$\leq$0.29
Pfβ	4.654	$\leq$0.57	0.84±0.11[b]	0.79±0.11[b]	0.88±0.17[b]	0.64±0.24
H_2 0-0 S(9)	4.695	$\leq$0.44	0.26±0.20[d]	1.29±0.23[d]	1.17±0.35[d]	$\leq$0.55
[Fe II]	4.889	$\leq$0.35	0.40±0.16[b]	0.53±0.23	$\leq$0.48	0.49±0.18[b]
		Ratio				
	Case B[g]	P1	P2	P3	P4	P5
Brβ/Brα	0.60	$\leq$0.68	0.54±0.11	0.71±0.07	0.61±0.14	0.51±0.23
Pfδ?Brα	0.10	3.44±1.26	0.73±0.18	0.37±0.07	0.20±0.09	$\leq$0.48
Pfγ/Brα	0.135	$\leq$0.48	0.07±0.03	0.13±0.03	$\leq$0.11	$\leq$0.30
Pfβ/Brα	0.20	$\leq$0.57	0.29±0.04	0.21±0.03	0.22±0.04	0.42±0.16

Note. — Intensities with errors of detected lines are given. Upper limits are at the 2σ level.

[a]Vacuum wavelength of a line in μm.

[b]FWHM fixed to the instrumental width ($\sim$ 0.03 μm) for a gaussian fit.

[c]Total intensity of the feature at 3.3 μm, which can be mainly contributed by either 3.3 μm PAH or Pfδ emission.

[d]Central wavelength fixed for a gaussian fit.

[e]Estimation of PAH intensity by subtracting the total intensity of the 3.3 μm feature by the scaled Brα intensity (i.e. 10% of the Brα intensity).

[f]Intensity of a minor PAH feature at 3.4 μm. Because of the curvature around the feature, the baseline is fitted by using a second order polynomial. Due to the ambiguous identification, the measured intensities can be regarded as an upper limit of the 3.4 μm feature intensity.

[g]Theoretical recombination line ratio in the case of "On-the-spot" approximation (so called "Case B") with $n_e \sim 10^2 - 10^7$ cm^{-3} and $T_e \sim 5 - 30 \times 10^3$ K (Hummer & Storey 1987).

C–H stretching mode, which is the first time that we detect this aromatic feature associated with a SNR. Although this 3.3 μm feature does not require a polycyclic molecular structure, it is referred to as a 3.3 μm PAH feature en bloc hereafter.

There are several minor PAH features near the 3.3 μm feature such as the weak 3.4 μm band, or the broad plateau at $3.2 - 3.6$ μm (e.g., Tielens 2008). In the IRC spectra, these minor PAH features are not obvious (Fig. 4.2). We could only find features at $3.4 - 3.5$ μm range from P2 and P3, but they do not look similar to each other (i.e., have different peak positions), and there seems no such feature at P1. We measured their intensities which may be regarded as an upper limit of the minor 3.4 μm PAH feature intensity considering that other minor features and/or the underlying plateau might be included (Table 4.2). Despite of our ambiguous detection, the presence/absence of the 3.4 μm feature could be an interesting issue, because this feature can give a constraint on the band carriers, which is still controversial. There are two interpretations for this feature; overtones (i.e., anharmonicity of hot bands; Allamandola et al. 1989; Geballe et al. 1989) and the C–H stretching emission from aliphatic side groups attached to PAHs (Joblin et al. 1996; Tielens 2008, and references therein). Excited PAH bands of C–H stretch transition can be shifted to longer wavelengths due to anharmonicity. In that case, the 3.4 μm intensity increases if excitation gets higher. Besides, smaller PAHs tend to have a higher ratio of the 3.4 to 3.3 μm bands for the same internal excitation energy (Geballe et al. 1989). Meanwhile, the presence of aliphatic bonds may delineate a balance between reactions with C, C^+, and H producing aliphatic groups and photodissociation of these peripheral groups. When the UV radiation is strong, the dehydrogenation of PAHs severely proceeds so that the 3.4 μm emission becomes weak. However, Tielens et al. (1994) suggested that ion bombardment can form the aliphatic bonds by hydrogenation of an amorphitized graphite surface in interstellar shocks. Although its detection is tentative, the possible presence of the 3.4 μm feature at P2 and P3 but P1 may indicate that the PAHs inside the SNR are generally smaller with a strong UV field or that aliphatic bonds are more abundant due to shock processing

compare to a preshock region. Further investigation with a higher sensitivity and spectral resolution would be needed to understand this point more clearly.

4.3.2 Brightness distribution of PAH, Hα, and H_2 emission

Although the 3.3 μm feature can be attributed to PAH emission, it is important to confirm whether the PAH emission is really associated with the SNR. For this purpose, maps of H_2, PAH, and Brα emissions are constructed from all spectra covering the PAH-bright area in the east (Figure. 4.3). The pixel size of the map is the same as the original pixel size of the slit ($1.46'' \times 1.46''$), and the intensity at each pixel is calculated by resampling them with a *nearest-neighbour interpolation* method[1] and averaging the data values that fall on the pixel. Then, the line maps are smoothed with a three-pixel Gaussian. The resultant line maps reveal the distribution of 3.3 μm PAH emission together with Brα and H_2 1-0 O(3). In order to remove the contamination by Pfδ line emission, the PAH map is subtracted by the scaled ($\times$0.1) Brα map. The morphology of PAH emission seemingly has association with those of other emission. The peak of PAH emission is found to be located at the tip of the bright wedge-shaped emission region, and the overall shape also shows enhanced emission along the wedge-shaped region. This strongly supports that the PAH emission is indeed related to the SNR.

All line maps in Figure 4.3 show the enhanced emission at the eastern region. Previous observations at the other wavelengths similarly show the brightness enhancement, which is interpreted as the effect of interaction between the SNR and the nearby molecular cloud at the southeast (Banas et al. 1997; Bilikova et al. 2007). The morphology of the PAH emission, however, has similarities and differences in details with respect to those of H_2 O(3) and Brα emission. The eastern boundaries of both H_2 and PAH emission are indented with respect to the Hα boundary (e.g., a gap at the east side between the two white crosses), while the Brα emission shows a

[1]The resampling uses a kernel extending a single input pixel. See https://www.astromatic.net/pubsvn/software/swarp/trunk/doc/swarp.pdf

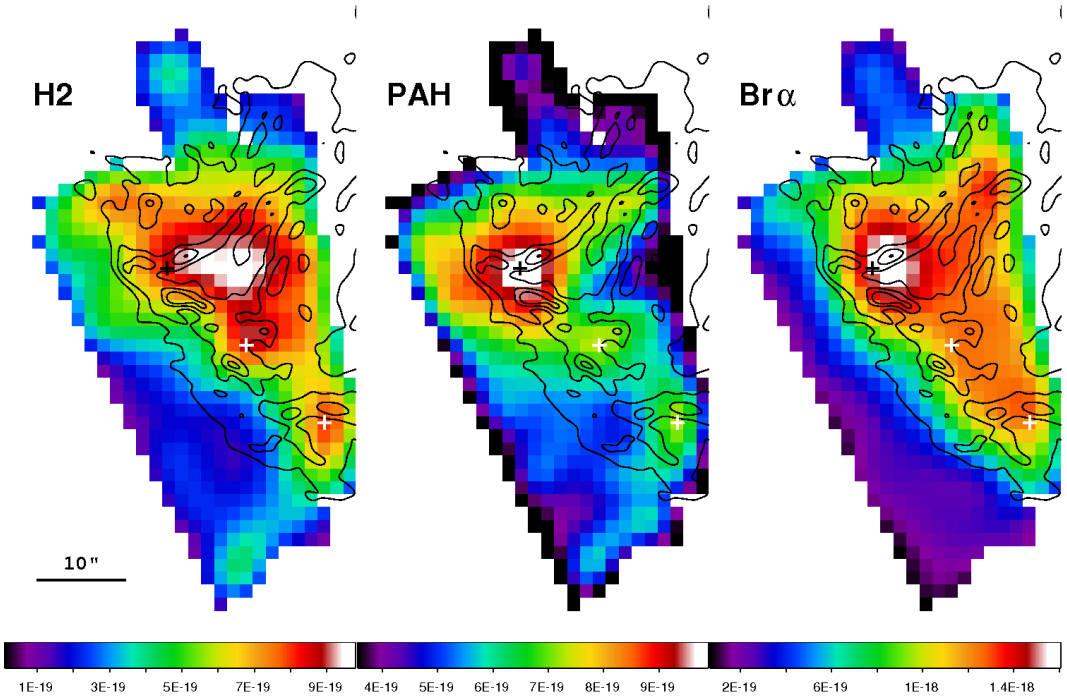

Figure 4.3 H_2 1-0 O(3), PAH, and Brα line maps of N49 by using *AKARI* IRC spectra. For comparison, contours (*black*) are taken from an Hα image of the *HST* WFPC2 (Bilikova et al. 2007); these contours are 10, 30, 50, and 70 % of the peak. The black cross marks the peak of PAH emission at (α_{2000}, δ_{2000}) = ($05^h26^m05.14^s, -66°05'03''$). The white crosses denote two clumps seen in the PAH line map. The scale bar represents $10''$ or 2.4 pc at 50 kpc. The color bars are given in units of W m^{-2} arcsec^{-2}. North is up, and east is to the left.

good agreement with it (also see Fig. 4.5,(a) and (c)). In particular, it is noticeable that both H_2 and PAH exceed the Hα boundary around the tip of the wedge-shape region, which is at the center of the interacting molecular cloud (i.e. P1 and P2 in Fig. 4.1). The two clumps of the PAH emission in the south (white crosses in Fig. 4.3) could be seen at the coincident positions in the H_2 map. Meanwhile, the peak position of the PAH emission is not matched with that of the H_2 but rather closer to that of the Brα. In addition, it is interesting that relatively weak PAH emission is observed where H_2 emission is the strongest.

Figure 4.4 compares the *average* intensities of the representative emission lines in individual slits from P1 (east) to P4 (west). Since the intensities (listed in Table 4.2) are those averaged over the slits, they may not directly describe the spatial variation but quantitatively show their trend. The peak intensity of PAH emission appears at P2 (more eastward) unlike others, and the emission at P1 (outside the shock boundary) still has a comparable intensity to that of the PAH emission at P2. We could not see any tight correlations of the PAH emission with either H recombination or H_2 molecular line emission, but it is notable that the recombination line intensity rapidly increases over the boundary (P2) whereas the molecular line intensity is steady at the east (even inside the boundary) and becomes stronger at P3.

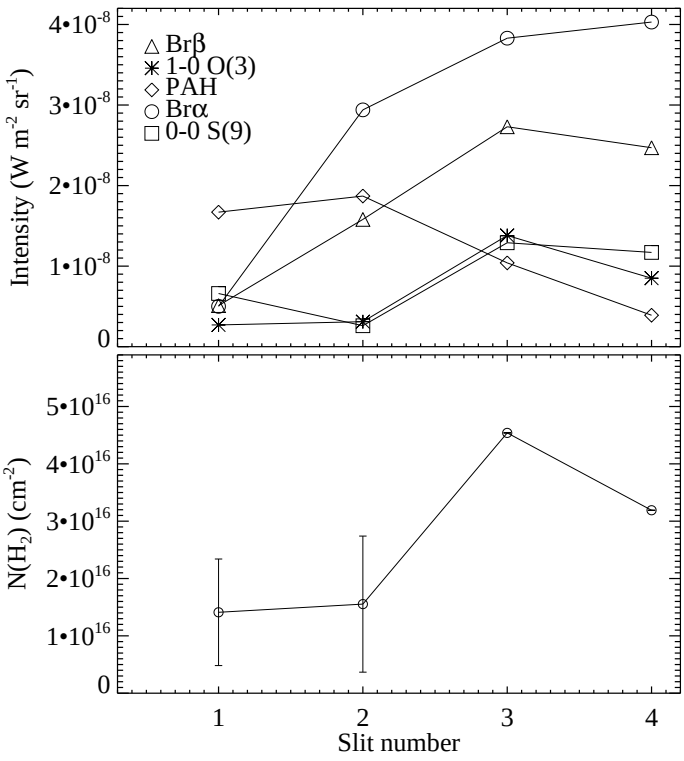

Figure 4.4 Variation of line intensities and H_2 column densities with respect to the different positions (from P1 to P4). The estimation of the column densities are described in §4.3.2. P5 spectrum is excluded due to non-detection of any H_2 lines.

Besides the emission intensities, we examined the variation of physical quantities such as the column densities, $N(H_2)$ and the gas temperatures, T_{gas} with respect to the four spectra, assuming local thermodynamic equilibrium (LTE) estimated from the intensities of H_2 molecular lines. H_2 line intensities can directly provide the column density, $N(J_u)$ of each upper state of the transitions, J_u. An extinction correction is not applied because the extinction toward N49 is negligible according to the measured $E(B-V) = 0.37$ (Vancura et al. 1992) and the extinction curve of the "average" LMC model (Weingartner & Draine 2001). Performing one-temperature LTE fits to the observed H_2 transitional lines with a given ortho-to-para ratio (OPR = 3), it is found that $N(H_2)$ varies from ~ 1 to $5{\times}10^{16}$ cm^{-2} (Fig. 4.4), while T_{gas} steadily remains at ~ 2000 K. The column densities we derived are much lower than the typical total column densities for SNRs ($\sim 10^{20}$ cm^{-2}, e.g., Hewitt et al. 2009). This is probably because only H_2 lines of high upper state transition are used for our estimation. In the case for SNRs, an *ankle-like curve* is representatively seen in the H_2 level populations (e.g., Shinn et al. 2010), so that H_2 pure rotational lines with low upper states such as H_2 S(0)$-$S(2) transitional lines mainly determine the total column density. Then, what we derived is likely to be the column density of a hot component ($T_{gas} \sim 2000$ K) within the SNR. Therefore, with the current observations, we cannot explore the relation between total H_2 and PAH.

The morphological characteristics of PAH emission with respect to molecular and ionic gas would be reconfirmed and clarified by comparing to narrow filter images with a higher spatial resolution. As complement, we use preexisting data, the H_2 1-0 S(0) at 2.12 μm taken with the *Anglo − Australian Telescope* (*AAT*) (Dickel et al. 1995), the *Spitzer* IRAC 8 μm (R. Williams et al. 2006), and the *Hubble Space Telescope* (*HST*) Hα image (Bilikova et al. 2007). The 2.12 μm and the Hα images generally show consistent distribution with the H_2 O(3) and Brα maps in Figure 4.3, respectively. In Figure 4.5, we can confirm the features described above. The eastern boundaries of the 2.12 μm and the PAH emission show a good agreement, and both emission are almost absent in the western part of the SNR

where the optical filaments are comparably bright as seen in P5 spectrum (Fig. 4.2). The peak of the PAH emission, however, shows better correspondence to that of Hα emission rather than that of 2.12 μm. It is certain that the PAH emission exists beyond the Hα boundary in east. Thus, the other observations of N49 similarly show the same morphological characteristics as our *AKARI* line maps.

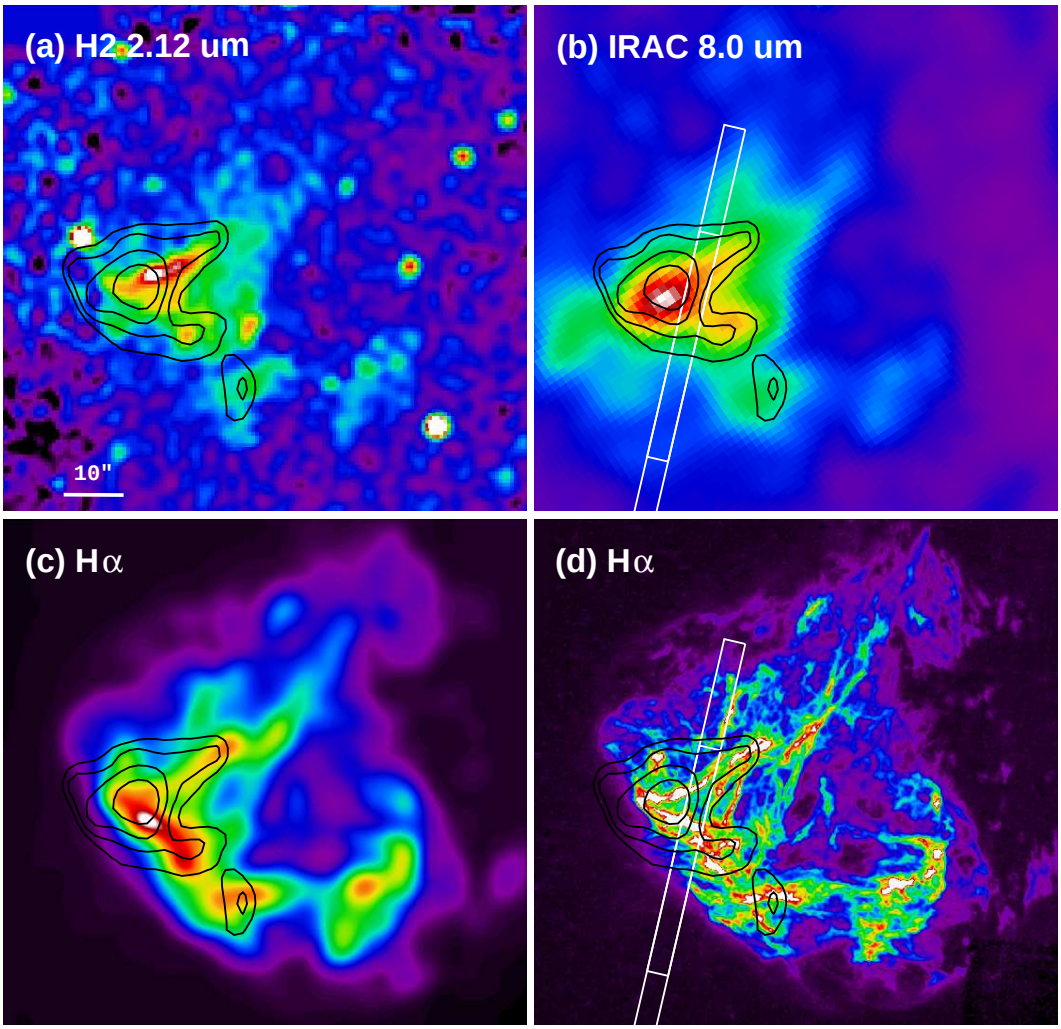

Figure 4.5 Images of N49 in (*a*) H_2 2.12 μm (Dickel et al. 1995), (*b*) IRAC 8.0 μm, (*c*) and (*d*) smoothed and original Hα (Bilikova et al. 2007). (*c*) Hα image is convolved to the spatial resolution of *AKARI* N3 image (FWHM $\sim 4.0''$). Contours overlaid in all images are from the PAH 3.3 μm map of Figure 4.3, of which levels are at 6, 7, 8, and 9 $\times 10^{-19}$ W m^{-2} arcsec^{-2}. North is up, and east is to the left. Positions of the *Spitzer* IRS SL resolution slits are marked in (*b*) and (*d*).

The characteristics of the PAH emission in N49 may be summarized as follows: (1) The overall morphology of the 3.3 μm PAH emission has the similarity to that of the H_2 emission in the sense that both are spatially confined. In contrast, the peak of the PAH emission is located rather closer to that of the Brα emission. (2) Toward the region with the brightest H_2 emission, however, the PAH emission is relatively faint. (3) There is PAH emission beyond the shock front in the east i.e., beyond the east boundary in optical, and its peak position is near the center of the interacting molecular cloud (Figure. 4.1). In addition, it is interesting that the distribution of PAHs shows a good agreement with the bright emission seen in the IRAC 8 μm image. A noticeable feature in the 8 μm image, not covered by our *AKARI* observation, is the bright emission beyond the eastern boundary. The nature of this feature is described in more detail in §4.3.3.

4.3.3 *Spitzer* IRS spectrum

The detection of the PAH emission at 3.3 μm implies the possibility of other major PAH band emission such as 6.2, 7.7, and 11.3 μm features. We examined the *Spitzer* IRS archival data for PAH emission (AOR 6586112, R. Williams et al. 2006). The IRS slits are centered on the brightest tip of the wedge-shape region (Fig. 4.5, (*b*)), and partially overlap with the IRC slits (P2 and P3). Retrieving the IRS low-resolution (SL: $5.2 - 14.5$ μm) Post-Basic Calibrated Data (PBCD) from the *Spitzer* archive, we have extracted spectra by using the standard SPICE package with a full aperture for an extended source (slit width: $3.7''$, aperture length: $50.4''$ (28 pixels)). We have applied background subtraction by using different order spectra. One of the benefits from the background subtraction is that the residual of the instrumental pattern (so called "jail-bar" pattern[2]) seen weakly in the PBCD data can be efficiently removed without much loss of S/N. The final IRS spectrum is shown in Figure 4.6. It is almost the same as the one published by R. Williams et al. (2006), but shows small differences probably due to background subtraction. The strong ionic lines such as

[2]See http://ssc.spitzer.caltech.edu/IRS/irsinstrumenthandbook/61/

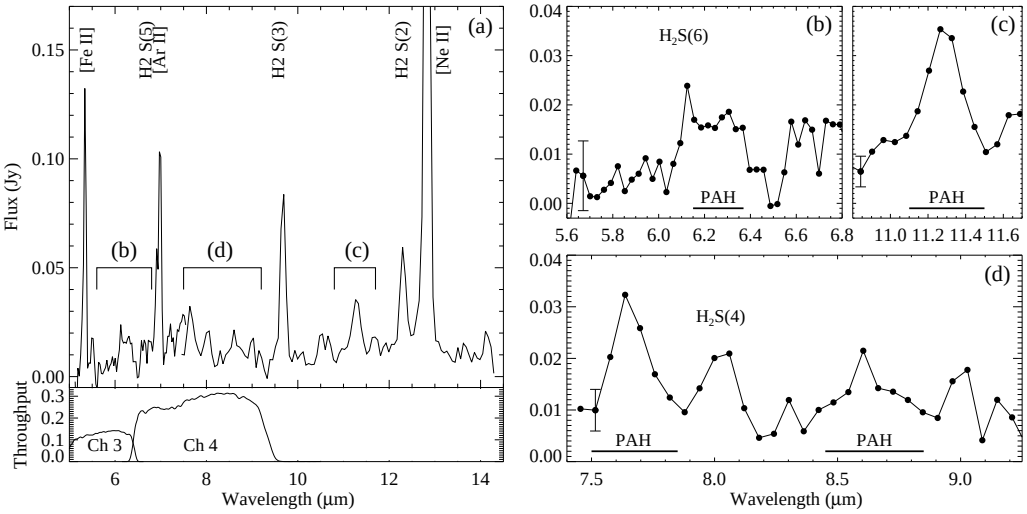

Figure 4.6 (a): IRS SL spectra of N49 with *Spitzer* IRAC spectral response curves. "Nod 1" position spectra are used only. The [Ne II] line at 12.8 μm is truncated for clarity. Dominant emission lines are labeled. $(b) - (d)$: Profiles of the PAH band emission features at 6.2, 11.3, and $7 - 9$ μm extracted from the IRS spectra. The extracted ranges are overplotted in (a). Detected PAH bands with H_2 emission lines are also marked. Error bars at the left bottom of each panel represent the typical error for the spectra.

[Fe II] and [Ne II] at $\lambda\lambda$ 5.32 μm and 12.83 μm, are detected together with several H_2 transitional lines up to 0-0 S(2) λ 12.30 μm (Fig. 4.6, (a)). As in R. Williams et al. (2006), a non-zero background level is seen, presumably because the background level varies. Taking a close look at the PAH bands in the spectra, we could identify several PAH features (Fig. 4.6, $(b) - (d)$). PAH emission of C–H out-of-plane bending mode at 11.3 μm is clearly detected, and weak C–C stretching features at 6.2 μm and 7.7 μm with ambiguous 8.6 μm emission of C–H in-plane bending mode can be seen. We derive the intensities of the PAH band features by simple summations with a linear baseline fit over the entire order. The intensities of the 6.2, 7.7, and 11.3 μm PAH features are estimated as 1.0 ± 0.5, 2.0 ± 0.4, and 1.6 ± 0.1 in units of 10^{-16} W m^{-2}, respectively. The quoted errors include the calibration uncertainty and 1 σ fluctuation in the baseline spectra.

For the clearly detected 11.3 μm PAH feature, we compare its spatial distribution to those of H_2 0-0 S(2) λ 12.3 μm and [Ne II] λ 12.8 μm along the slit (Fig. 4.7). For comparison, the spatial profile of Hα emission extracted from the *HST* image is also shown. Although a sharp jump in the Hα intensity is not seen, a shock front might be located near the place where the Hα intensity rapidly increases. A dashed line in Figure 4.7 can be regarded as the SNR boundary. The emission outside the shock front could originate from ambient gas heated by radiative precursors, and the hint of the radiative precursor can be found in Hα emission in the zoomed profile at lower intensity level (Fig. 4.7, *Bottom*). Beyond the SNR boundary, continuous decreases of 11.3 μm PAH and H_2 S(2) emission are seen up to the position around the pixel zero. The bump of the PAH emission at -4 pixel in the preshock area is more likely due to a background fluctuation (the bump is located outside of the southern boundary of Fig. 4.5 (*b*)). The profile of PAHs shows smooth decrease near the shock front like that of H_2, but shows better agreement with that of [Ne II] beyond the peak to the downstream. This is consistent with the morphological characteristics of PAH emission seen in the line maps. Similar distribution between the 11.3 μm PAH emission and [Ne II] has been observed toward several objects. For example, in the planetary nebula, BD +30 3639, Matsumoto et al. (2008) detected the coexistence of PAHs and ionized gas, which has been attributed to a slow destruction of PAHs in the ionized region with the high electron density. Then, the good agreement between the 11.3 μm emission and [Ne II] in N49 might imply that destruction of small PAHs slowly proceeds in the shocked region (see more § 4.2).

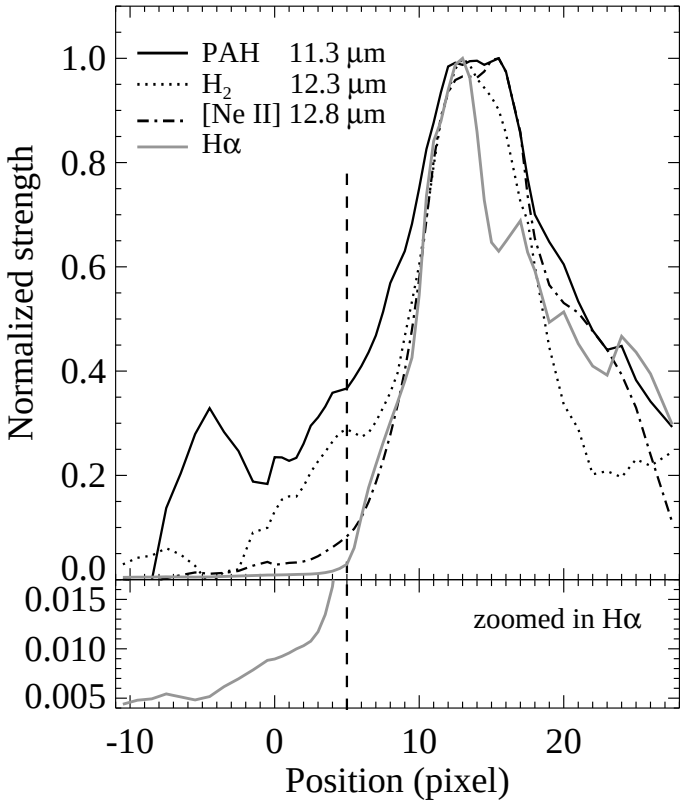

Figure 4.7 *Top*: IRS SL line profiles of PAH λ 11.3 μm (black solid), H_2 0-0 S(2) λ 12.3 μm (dotted), and [Ne II] λ 12.8 μm (dash dot). For comparison, an one-dimensional cut of Hα emission along the IRS slits (gray solid) is extracted from the *HST* image smoothed to the pixel scale of the IRS. *Bottom*: The same profile of Hα, but zoomed in for the variation at lower levels. The dashed line represents the SNR boundary (the probable location of the shock front). One pixel corresponds to 1.8″, and the coordinate of the position for the zero pixel is (α, δ) = ($05^h26^m05^s, -66°05'28''$; J2000.0). The negative and the positive correspond to south and north, respectively.

As mentioned in the previous section, the *Spitzer* IRAC 8 μm image is quite similar to the 3.3 μm PAH emission image (Fig. 4.5, (*b*)). In addition, the structure protruding from the bright tip at east is only seen in the 8 μm image among the IRAC images, which infers that the $7-9$ μm PAH bands possibly account for the feature. In the IRS spectra, [Ar II] line at 6.98 μm is the strongest emission line within the IRAC channel 4 band. However, it is necessary to consider other contributors such as H_2 0-0 S(5), S(4) at 6.9, 8.0 μm as well as possible $7-9$ μm PAH emissions. In order to examine their relative contributions to the IRAC 8 μm band, we measure the intensities of H_2 S(5) and [Ar II] lines. Since they are resolvable enough to estimate their intensities by using two Gaussian fits, we can obtain 1.76 ± 0.34 and 3.78 ± 0.36 in unit of 10^{-16} W m^{-2} for H_2 S(5) and [Ar II], respectively. Then, the intensity of H_2 emission together with the 7.7 μm PAH feature intensity ($3.76 \pm 0.52 \times 10^{-16}$ W m^{-2} in total) seems to be comparable to that of [Ar II], so that the emission seen in the IRAC 8 μm image is dominated by not only the [Ar II] but also the H_2 lines with the $7-9$ μm PAH features. Therefore, the similarity between the 3.3 μm PAH emission image and the 8 μm image could arise from $7-9$ μm PAH emission with H_2 line emission, although we cannot rule out that the PAHs emitting the feature can coexist with the ionized gas. There is non-zero continuum level in the IRS spectrum in Figure 6 that we attributed to the residual of the background subtraction. The dust emission and synchrotron (or free-free) emission from the SNR should be negligible at this wavelength, so that even if the non-zero continuum is real, it should come from unrelated object. Therefore, we conclude that, although we cannot completely exclude the contamination from the general ISM, the good spatial correspondence is mainly due to the $7-9$ μm PAH emission in the IRAC 8 μm band.

4.4 Discussion

4.4.1 Physical properties of PAHs in N49

The PAH emission features are expected to reflect the local physical conditions. In particular, the relative strength variations among the PAH features at different wavelengths are mainly attributed to their different charge states (e.g., Bakes et al. 2001). PAH emission from C–H modes such as 3.3 and 11.3 μm features becomes stronger in a neutral state, whereas others from C–C modes such as 6.2 and 7.7 μm features become stronger in an ionic state. Generally, comparisons of the intensities of 3.3 μm and 11.3 μm, both normalized to that of 6.2 μm, are regarded as an indicator for the degree of ionization of PAHs (e.g., Tielens 2008, and references therein). Similarly, the intensity ratios of 6.2 μm to 11.3 μm and 7.7 μm to 11.3 μm are often used as well. In our observations, the intensities of 3.3 μm bands cannot be directly compared with those of other PAH bands in the IRS spectra, but from the IRS spectra, we calculate band ratios among 6.2, 7.7, and 11.3 μm PAH emission; $I_{6.2}/I_{11.3} = 0.63 \pm 0.31,\ I_{7.7}/I_{11.3} = 1.25 \pm 0.26$.

Our ratios show unusually weak $6-8$ μm PAH features relative to a 11.3 μm feature in comparison with the median of the ratios from the star-forming galaxies ($I_{7.7}/I_{11.3} \simeq 3.6$ in Smith et al. 2007) or those for Galactic diffuse emission ($I_{7.7}/I_{11.3} \simeq 2.0-3.3$ in Sakon et al. 2004). Such low PAH 7.7/11.3 ratios have been reported in some of elliptical galaxies, which is reasonably interpreted as a result of a larger fraction of neutral PAHs due to soft radiation field from evolved stars (e.g., $I_{7.7}/I_{11.3} \simeq 1-2$ in Kaneda et al. 2008). Similarly, our ratios can indicate that the PAHs in N49 are dominantly neutral even though the environmental cause is different. Figure 4.8 is a diagram of PAH band ratios ($I_{6.2}/I_{11.3}$ versus $I_{7.7}/I_{11.3}$) from various objects in literatures, which shows that these PAH band ratios are linearly correlated regardless of object type. Note that the PAHs are mainly neutral in the lower left and mainly ionized in the upper right. Interestingly, it is found that our ratios also follow the universal linear correlation between the two ratios.

As far as we know, N49 is the only SNR where both $I_{6.2}/I_{11.3}$ and $I_{7.7}/I_{11.3}$ ratios are obtained. In N132D, which is another SNR with PAH emission, only an upper limit of $I_{6.2}/I_{11.3}$ ratio could have been derived (Tappe et al. 2006), and is marked in Figure 4.8. This upper limit suggests that the ionization fraction of PAHs in N132D is not high, which is consistent with the theoretical expectation that PAHs can become neutral within a short time scale in the postshock layer (see Figure 5 in Micelotta et al. 2010a). It is known that the charge states of PAHs are determined by the balance between the photoionization and the electron/ion collisions. The charge state is proportional to the quantity $\sim G_0\sqrt{T}/n_e$ (for a review, see Tielens 2008), where G_0 is the intensity of radiation field in units of the Habing field (1.6×10^{-6} W m^{-2}), T is the gas temperature, and n_e is the electron density. The ones with small $I_{6.2}/I_{11.3}$ ratio (or with neutral PAHs) represent a region where $G_0\sqrt{T}/n_e$ is small. For a few well-studied photodissociation regions (PDRs), Galliano et al. (2008) have empirically interpreted the PAH band ratio with the above physical properties, $I_{6.2}/I_{11.3} \simeq [G_0/3040\ n_e(\mathrm{cm}^{-3})](T_{gas}/10^3\ \mathrm{K})^{1/2}+0.53$ valid in the range $400 \leq G_0/(n_e/1\ \mathrm{cm}^{-3})(T_{gas}/10^3\ \mathrm{K})^{1/2} \leq 4000$.

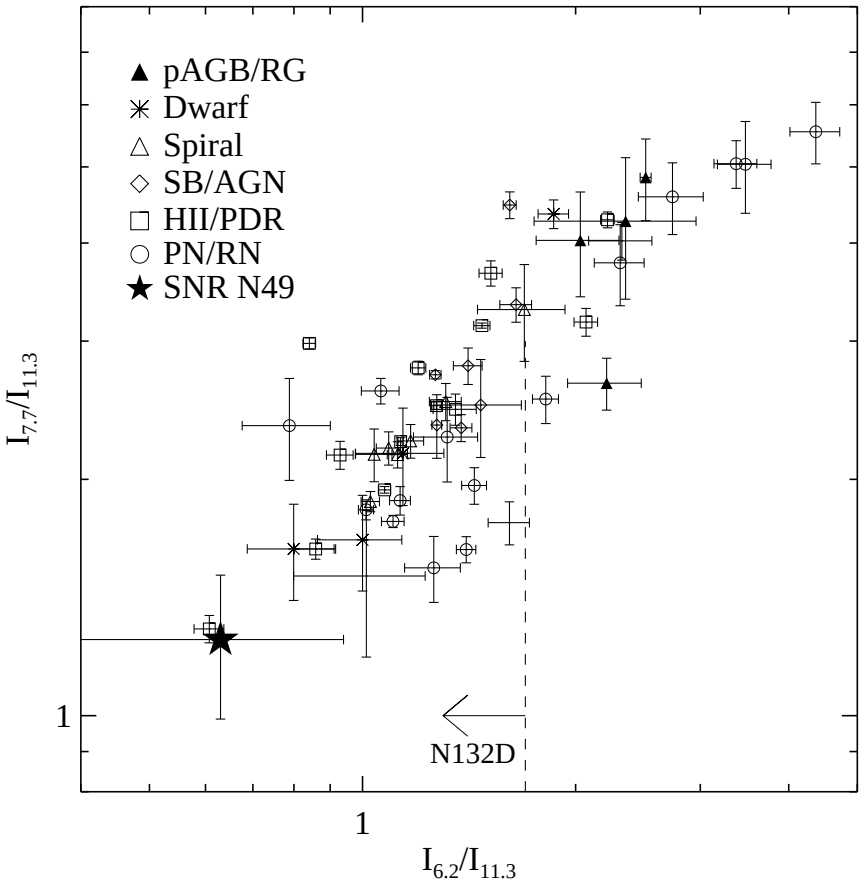

Figure 4.8 PAH band ratios of SNR N49 as well as various objects from literatures (Vermeij et al. 2002; Sloan et al. 2007; Galliano et al. 2008; Bernard-Salas et al. 2009). The ratio in N49 is derived from the *Spitzer* IRS spectrum (§ 3.3). The upper limit of $I_{6.2}/I_{11.3}$ from the SNR N132D is marked as a dashed line (Tappe et al. 2006). Different symbols denote different types of objects. Few objects without any symbols are either Herbig Ae/Be or T Tauri stars or a Magellanic object.

As we will discuss in the next section, the detected PAH emission is probably either from the PAHs in the shocked molecular gas and/or from the PAHs in the preshock gas heated by radiative precursor. In dense molecular clouds, PAHs usually exist in a neutral (and anionic) state. Even after they experience continuous (C-type) shock waves, neutral PAHs predominate in all charged states because photo-ionization is not significant in these circumstances (Flower & Pineau des Forêts 2003). The PAH emission could be also from PAHs in preshock gas heated by radiative precursor. In N49, by modeling the UV and optical spectrum, Vancura et al. (1992) find that preshock densities of $20 - 940$ cm^{-3} in the velocity range, 40 to 270 km s^{-1}, are required for the denser regions with radiative emission. The strength of the UV precursor in radiative shocks (30 km s^{-1} $\leq v_s \leq$ 200 km s^{-1}) is calculated that $G_0 \approx 1.6 n_0 v_{s7}$, where v_{s7} is the shock velocity per 100 km s^{-1} and n_0 is the preshock hydrogen nucleus density (McKee et al. 1987, and references therein). The coefficient varies with the shock velocity, and it is 1.6 when $v_s = 100$ km s^{-1}. Then adopting a preshock density as 150 cm^{-3} at $v_s = 100$ km s^{-1} under the requirement that $\rho_0 v_s^2$ remains constant (Vancura et al. 1992), G_0 becomes 240. This UV radiation heats a column of 10^{19} cm^{-2} hydrogen nuclei to $\sim$ 5000 K and fully ionizes it (e.g., the case of $n_0 = 100$ cm^{-3} and $v_s = 100$ km s^{-1} in Allen et al. 2008). In this radiative precursor region, the ratio $G_0\sqrt{T}/n_e$ will be small ($\sim$ 110), so that the PAHs will be neutral. If we extrapolate the empirical relation of Galliano et al. (2008), we obtain $I_{6.2}/I_{11.3} \simeq 0.53$ which is consistent with the observed ratio.

Meanwhile, the observed band ratio can be compared with theoretical studies by Draine & Li (2001), which show how the charge state and size of PAHs affect relative strengths of three band emission, 6.2 μm/7.7 μm versus 11.3 μm/7.7 μm (see Figure 16 in their paper). Our observed fluxes give $I_{6.2}/I_{7.7} \simeq 0.50 \pm 0.27$ and $I_{11.3}/I_{7.7} \simeq 0.80 \pm 0.15$ which are located near the line for neutral PAHs. More interestingly, our high $I_{6.2}/I_{7.7}$ ratio indicates that small PAHs are dominant in N49 although the error is large. The existence of small PAHs can also be verified by $I_{3.3}/I_{11.3}$ ratio since larger PAHs produce relatively a strong 11.3 μm feature

while the 3.3 μm emission is enhanced by small PAHs (e.g., Schutte et al. 1993). It is not simple to directly derive the $I_{3.3}/I_{11.3}$ ratio from our data because the 3.3 μm and 11.3 μm fluxes are observed by different telescopes and positions. However, we make a rough estimation to obtain both the surface brightness at the peak and the integrated intensity with the full aperture (50.4″) along the IRS slit from the *AKARI* 3.3 μm line map (Fig. 4.3) and the *Spitzer* spectrum (see the slit position in Fig. 4.5). The $I_{3.3}/I_{11.3}$ ratios of the peak brightness and the total intensity are measured as ~ 0.43 and ~ 0.30, respectively. These ratios are in a high end of the observed range (in general, $0.2 - 0.3$), which can be accounted for by small PAHs unless the radiation is hard enough to excite large PAHs (Mori et al. 2012). For 100 km s^{-1} radiative shocks, the UV radiation from the shock is mostly in Lyα photons (McKee et al. 1987), so it might be difficult to directly compare the shock radiation to the radiation from a central source. However, no detectable PAH feature at longer wavelengths easily produced by large PAHs (e.g., 16.2 or 17.4 μm features) is more likely to support a small contribution of large PAHs to the 3.3 μm feature (see Figure 9 of R. Williams et al. 2006). Therefore, the observed $I_{6.2}/I_{7.7}$ and $I_{3.3}/I_{11.3}$ ratios indicate the presence of small PAHs, which is consistent with the PAH formation by fragmentation from larger carbonaceous grains but not with the preferential destruction of small PAHs in shocked gas.

4.4.2 Origin of PAH emission

PAH emission has been detected toward few shock-associated regions. Due to the limited observational evidence, it is poorly understood how shocks play a role in PAH processing. Generally, there are two sides to SNR shocks in terms of PAH processing, i.e., shocks can produce PAH molecules by shattering larger dust grains (e.g., Jones et al. 1996), but shocks can also destroy them by collisions with energetic particles in shocked gas (e.g., Micelotta et al. 2010a). Micelotta et al. (2010b) show that the destruction mechanism in a hot gas ($T \geq 3 \times 10^4$ K) is dominated by electron collision for small/medium size PAHs ($50 - 200$ C-atom). They describe a

PAH lifetime in a hot gas as $\tau_0 = N_{\rm C}/Jn_{\rm H/e}$, where $N_{\rm C}$ is the initial PAH size, J is the rate constant for electrons, nuclear and electronic interactions, and $n_{\rm H/e}$ is the hydrogen/electron density. At a fixed PAH size, a PAH lifetime can be determined by the gas density and temperature. In a rarefied gas with fast shocks ($v_s \geq 300$ km s^{-1}), no PAH formation is expected, and most PAHs are completely destroyed soon after being swept up by shocks. In particular, smaller PAHs are eroded more easily for $T \leq 10^6$ K. Nevertheless, if we see the emission from PAHs just swept up, the PAH emission should be confined to the shock front. In a dense medium, however, as shocks become slower ($v_s \leq 100 - 150$ km s^{-1}), PAHs might survive and/or be formed in those shocked environments (Micelotta et al. 2010a). Then, the detection of PAH emission in the shocked regions requires either efficient formation of PAHs or shielded condition against complete destruction. Currently, observational difference between newly formed and survived PAHs is not obvious, but it is supposed that the newly formed PAHs undergo the same processing as the survived ones soon after. Meanwhile, PAH emission could be also produced outside the shocked region by radiative precursors of shocks. Hence, it is necessary to separately examine the dominant mechanism for PAH emission depending on the local shock condition.

The complex structures of N49 imply that physical conditions inside the remnant should significantly vary in localities. This remnant can be largely divided up into three kinds of environments related to the characteristics of the medium from which different emission arises. The hot gas with X-ray emission is generated by the fast shock propagating in the diffuse intercloud medium (preshock density $n_0 = 0.9$ cm^{-3}, $n_e = 27 - 2300$ cm^{-3}, $T \geq 7 \times 10^6$ K, and $v_s \sim 730$ km s^{-1} in Park et al. 2003). The dense ambient medium produces the bright optical filaments (i.e., ionic line emission) by shocks of $v \leq 140$ km s^{-1} ($n_0 = 20 - 940$ cm^{-3}, $T \sim 10^4$ K in Vancura et al. 1992). The electron densities of the filaments vary from $n_e \simeq 70$ to 515 cm^{-3}, and the densest regions have the densities of $1000 - 1800$ cm^{-3} (Bilikova et al. 2007; Vancura et al. 1992). Lastly, the molecular line emission such as H_2 lines can arise from the dense clumps where slow (nondissociative) shocks are impinging on

(in general, $n_0 \geq 30$ cm^{-3}, $v_s \leq 50$ km s^{-1} in Draine & McKee 1993). In N49, both shocked molecular and ionic gases interestingly show analogous distributions, and the PAH emission is likely to be associated with both gases. This is not surprising in the sense that N49 is known to be interacting with a nearby molecular cloud (Banas et al. 1997). The coexistence of both molecular and ionic shocks in a single SNR is occasionally seen in SNRs interacting with molecular clouds, since the shocked dense clumps emitting H_2 transitional line emission are immersed in a less dense medium that emits various ionic line emission after swept up by shocks (e.g., Chevalier 1999).

In the hot diffuse medium of N49 ($n_e = 27$ cm^{-3}, $T = 7 \times 10^6$ K), the lifetime of PAHs with $N_C = 200$ is ~ 1 month by adopting the analytical fits to the rate constant ($J \sim 2.7 \times 10^{-6}$ cm^3 s^{-1}; Table 2 in Micelotta et al. 2010b). Even for large-sized PAHs or PAH clusters, the lifetime is not long enough to be detected (e.g., $\sim$ 20 months for $N_C = 1000$, Fig. 8 in Micelotta et al. 2010b). To explain the observed PAH emission, protective environments in N49 are necessary, which have already been noticed in optical spectroscopic observations (Vancura et al. 1992; Bilikova et al. 2007). By using the echelle observations with the *HST* image (see Fig. 3 in Bilikova et al. 2007), some broad emission features in the echellegrams reveal a "head-tail" structure, of which the bright emission at the head has a smaller radial velocity offset from the systemic velocity than the fainter emission in the tail. This type of the structure could originate from shocks encountering the dense gas. While a shock is propagating through the preshock gas in the inner part of the dense bright regions, the shock velocity drops so that the gas deep inside the dense filament can avoid to be swept up by shocks, staying unshocked. The observed Hα recombination lines at the systemic velocity in the optical spectrum support this.

Based on the above discussion, we propose a schematic model of the PAH emitting condition in N49 in Figure 4.9. As a shock is retarded by a dense gas (Region II and shocked Region III), the temperature of the postshock gas can substantially decrease ($T_{\rm gas} \propto v_s^2$). The PAH lifetime under these circumstances can significantly increase because the rate constant rapidly declines below 10^5 K (Micelotta et al.

2010b). Vancura et al. (1992) have measured electron densities and electron temperatures for the bright optical filament of N49 as $\sim 1 \times 10^3$ cm^{-3} and $\sim 1 \times 10^4$ K, respectively. These quantities lead to the lifetime of 1.2×10^6 yr for 200 C-atom PAHs (c.f., $J \sim 5.2 \times 10^{-15}$ cm^3 s^{-1}), which is much longer than the age of the SNR. PAHs in the central region (unshocked Region III) of the molecular clumps (and the dense filaments) can be heated by UV photons that mainly originate from the radiative shell, more precisely in this case, the knotty optical filaments around the clumps. In the case of the PAH emission observed outside the shock front (seen eastward at the tip in Fig. 4.3), it is most likely that the preexisting PAH molecules are heated by the radiative precursors and produce the emission features. When the shock velocity is greater than 80 km s^{-1}, the ionizing UV fluxes produced by the precursor become effective (Shull & McKee 1979). The bulk range of the shock velocity in N49 is measured as $\leq$ 140 km s^{-1} (Vancura et al. 1992), and we indeed see the hint of the radiative precursor in the zoomed Hα line profile (Fig. 4.7). In summary, PAH emission can be associated with shocked ionic gas (Region II) or (shocked) molecular gas (Region III) when the shock is sufficiently retarded with existence of heating source such as UV photons (Fig. 4.9). Also, as a shock is propagating and retarded inside the dense region, shocked ionic and molecular gas can hierarchically exist together with PAH emission. Then, the morphological correlation of the PAH emission to other emission would depend on the shock velocity and the preshock density.

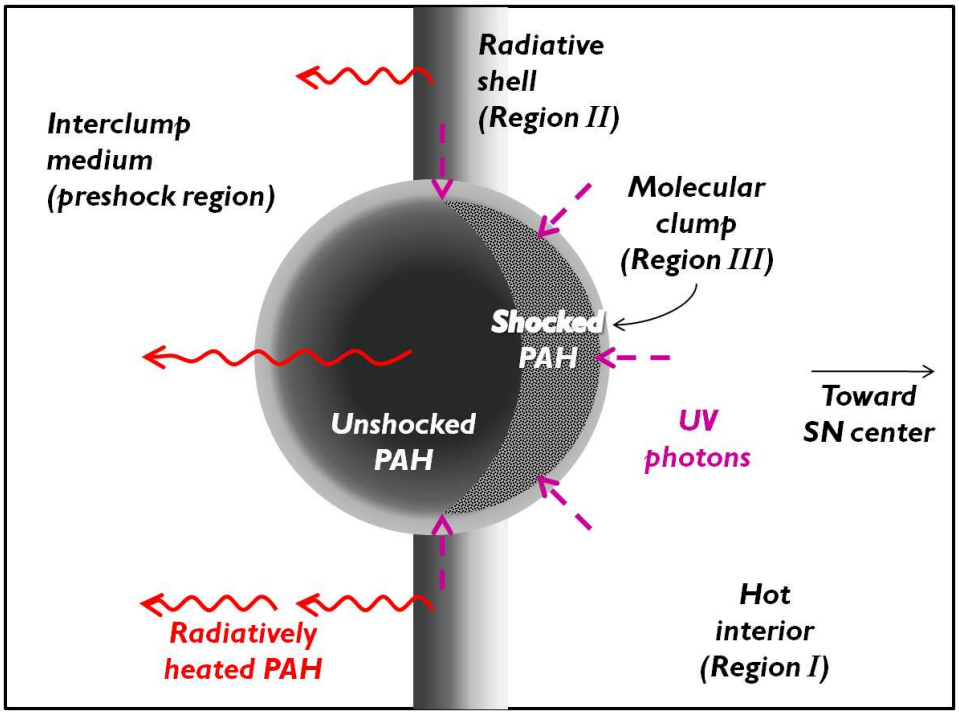

Figure 4.9 Schematic diagram of local medium structures in N49. There are largely three kinds of medium; the hot interior, the radiative shell, and the molecular clumps emitting X-ray, ionic line emission, and molecular emission, respetively. Darker color indicates the higher survivability of PAH molecules. In the case of a dense molecular clump, its inner layer can remain unshocked. UV photons mainly originate from the radiative shell, more precisely, neighboring optical filaments around the molecular clump in N49. Survived PAHs associated either the radiative shell or the molecular clump can be heated by UV photons and produce detectable emission features.

The absence of PAH emission at the peak of the H_2 emission is interesting. In Figure 4.5, the region with the brightest H_2 emission seems to coincide with one of the bright Hα filaments, and it is found that the filament particularly shows the most extreme difference among Hα, [S II], and [O III] emissions in optical; the [O III] emission is absent while the [S II] emission is relatively stronger than Hα (see Fig. 1 in Bilikova et al. 2007; Vancura et al. 1992). According to shock models in Vancura et al. (1992), [O III] emission is generally produced by faster shocks and cannot be produced for shocks with velocities ≤ 80 km s^{-1}. Meanwhile, as the shock velocity decreases, the intensities of [S II] show an increasing tendency with respect to that of Hβ in the model calculation. In this context, it is likely that relatively slow shocks (≤ 80 km s^{-1}) have reached the filament and have resulted in these differences in the optical spectra. If so, the faint PAH emission can be explained, because the shocks with $v_s \leq 80$ km s^{-1} cannot produce sufficient UV radiation (Shull & McKee 1979) at the outer layer of the filament which is necessary to heat PAH molecules. For H_2 emission, however, hydrogen molecules can be collisionally excited by shocks with those velocity ranges, and produce bright emission. For $v_s \geq 25 - 30$ km s^{-1}, the line intensity is sensitive to the preshock density, not to the shock velocity (Burton et al. 1992). Hence, even if PAHs can survive, they might not generate detectable emission due to the lack of heating sources, while it is possible to produce bright H_2 emission in the same environment. This may also explain the IRS spectra of the Galactic SNRs interacting with molecular clouds, where H_2 emission is prominent but the PAH emission is absent (e.g., Hewitt et al. 2009).

The detection of 3.3 μm PAH band feature from N49 is surprising in a sense that only small PAHs with < 100 C-atoms or a size < 6 Å can notably produce the feature (Draine & Li 2007) while small PAHs can be easily destroyed by strong shocks. Even elliptical galaxies showing low PAH 7.7/11.3 μm ratios (i.e., mainly neutral PAHs) seem to have no significant 3.3 μm PAH emission due to the lack of small PAHs (Kaneda et al. 2007). Meanwhile, the comparison between our PAH band ratios ($I_{6.2}/I_{7.7}$ and $I_{3.3}/I_{11.3}$) and the numerical studies (Draine & Li 2001; Mori

et al. 2012) support that small PAHs are dominant in N49. In addition, there is no indication of the $15-20$ μm feature in the IRS spectrum by R. Williams et al. (2006) (see their Fig. 9), which is a signature of large PAHs. In the case of N132D, however, the relatively strong $15-20$ μm hump compared to $6-11.3$ μm PAH features suggests that the large PAHs are dominant, which was interpreted as evidence for the survival of large PAHs behind fast shock (Tappe et al. 2006). Thus, PAH processing in N49 and N132D is likely to differ from each other. This difference in PAH sizes can be explained by the different environments and evolutionary stages of the two SNRs: N49 is a middle-aged SNR ($\sim$ 6600 yr, Park et al. 2003) and is interacting with a nearby molecular cloud with a radiative shock ($v_s \simeq 100$ km s^{-1}), while N132D is relatively young ($\sim$ 2500 yr, Morse et al. 1995) and still has a fast shock in less dense environment ($\bar{v}_s \simeq 800$ km s^{-1}, Morse et al. 1995). In a dense gas with a moderately low temperature ($\leq 3 \times 10^4$ K), PAHs would survive regardless of the size. This is because the nuclear interaction with helium is the dominant process of destruction in that situation, which does not significantly depend on the size of PAHs (see Fig. 5 in Micelotta et al. 2010b). Hence, small PAHs are *NOT* preferentially destroyed in N49, which can reasonably explain our detection of the 3.3 μm PAH feature in the postshock region with the relatively low temperature. This might imply that a wide range of PAH properties can be found in SNRs.

Based on our observations, it might be difficult to understand in detail, for example, what is the dominant heating mechanism for emitting PAH features in the SNR, and whether the PAHs are newly formed or not. Nevertheless, it seems obvious that one of the essential conditions for the survival/(re)formation of PAHs is the existence of dense ambient medium around a SNR which directly influences the evolution of shocks such as the shock velocity. In addition to this, the sufficient heating source such as UV radiation is necessary for survived PAHs to produce observable PAH emission from a SNR.

Bibliography

Allamandola, L. J., Tielens, A. G. G. M., & Barker, J. R. 1989, ApJS, 71, 733

Allen, M. G., Groves, B. A., Dopita, M. A., et al. 2008, ApJS, 178, 20

Bakes, E. L. O., Tielens, A. G. G. M., & Bauschlicher, Jr. C. W. 2001, ApJ, 556, 501

Banas, K. R., Hughes, J. P., Bronfman, L., & Nyman, L.-A. 1997, ApJ, 480, 607

Bernard-Salas, J., Peeters, E., Sloan, G., et al. 2009, ApJ, 699, 1541

Bilikova, J., Williams, R., Chu, Y., et al. 2007, AJ, 134, 2308

Blair, W. P., Sankrit, R., Shelton, R., et al. 2000, ApJ, 538, 61

Burton, M. G., Hollenbach, D. J., & Tielens A. G. G. M. 1992, ApJ, 399, 563

Chevalier, R. A. 1999, ApJ, 511, 798

Dickel, J. R. & Milne, D. K. 1998, AJ, 115, 1057

Dickel, J. R., et al. 1995, ApJ, 448, 623

Draine, B. T. & Li, A. 2001, ApJ, 551, 807

Draine, B. T. & Li, A. 2007, ApJ, 657, 810

Draine, B. T. & McKee, C. 1993, ARA&A, 31, 373

Flower, D. R. & Pineau des Forêts, G. 2003, MNRAS, 343, 390

Galliano, F., Madden, S. C., Tielens, A. G. G. M., Peeters, E., & Jones, A. P. 2008, ApJ, 679, 310

Geballe, T. R., Tielens, A. G. G. M., Allamandola, L. J., Moorhouse, A., & Brand, P. W. J. L. 1989, ApJ, 341, 278

Hewitt, J. W., Rho, J., Andersen, M., & Reach, W. T. 2009, ApJ, 694, 1266

Hollenbach, D. & McKee, C. F. 1989, ApJ, 342, 306

Hummer, D. G. & Storey, P. J. 1987, MNRAS, 224, 801

Ita, Y., Onaka, T., Kato, D., et al. 2008, PASJ, 60S, 435

Joblin, C., Tielens, A. G. G. M., Allamandola, L. J., & Geballe, T. R. 1996, ApJ, 458, 610

Jones, A. P., Tielens, A. G. G. M., & Hollenbach, D. J. 1996, ApJ, 469, 740

Kaneda, H., Onaka, T., & Sakon, I. 2007, ApJ, 666, L21

Kaneda, H., Onaka, T., Sakon, I., et al. 2008, ApJ, 684, 270

Matsumoto, H., Sakon, I., Onaka, T., et al. 2008, ApJ, 677, 1120

McKee, C. F., Hollenbach, D. J., Seab, G. C., & Tielens, A. G. G. M. 1987, ApJ, 318, 674

Micelotta, E. R., Jones, A. P., & Tielens, A. G. G. M. 2010a, A&A, 510, A36

Micelotta, E. R., Jones, A. P., & Tielens, A. G. G. M. 2010b, A&A, 510, A37

Mori, R, et al. 2012, ApJ, 744, 68

Morse, J. A., Blair, W. P., Dopita, M. A., et al. 1996, AJ, 112, 509

Murakami, H., Baba, H., Barthel, P., et al. 2007, PASJ, 59S, 369

Neufeld, D. A., Hollenbach, D. J., Kaufman, M. J., et al. 2007, ApJ, 664, 890

Onaka, T., Matsuhara, H., Wada, T., et al. 2007, PASJ, 59S, 401

Ohyama, Y., Onaka, T., Matsuhara, H., et al. 2007, PASJ, 59S, 411

Park, S., Burrows, D. N., Garmire, G. P., et al. 2003, ApJ, 586, 210

Reach, W. T., Rho, J., Jarrett, T. H., et al. 2002, ApJ, 564, 302

Reach, W. T., Rho, J., Tappe, A., et al. 2006, AJ, 131, 1479

Sakon, I., Onaka, T., Ishihara, D., et al. 2004, ApJ, 609, 203

Schutte, W. A., Tielens, A. G. G. M., & Allamandola, L. J. 1993, ApJ, 415, 397

Seok, J. Y., Koo, B.-C., Onaka, T., et al. 2008, PASJ, 60S, 453

Shinn, J.-H., Koo, B.-C., Burton, M., Lee, H.-G., & Moon, D.-S. 2010, AdSpR, 45, 445

Shull, J. M. & McKee, C. F. 1979, ApJ, 227, 131

Shull, P., Jr. 1983, ApJ, 275, 592

Shull, J. M. 1983, ApJ, 275, 611

Sloan, G. C., Jura, M., Duley, W. W., et al. 2007, ApJ, 664, 1144

Smith, J. D. T., Draine, B. T., Dale, D. A., et al. 2007, ApJ, 656, 770

Tappe, A., Rho, J., & Reach, W. T. 2006, ApJ, 653, 267

Tielens, A. G. G. M. 2008, ARA&A, 46, 289

Tielens, A. G. G. M., McKee, C. F., Seab, C. G., & Hollenbach, D. J. 1994, ApJ, 431, 321

Warren, J. S., Hughes, J. P., & Slane, P. O. 2003, ApJ, 583, 260

Weingartner, J. C. and Draine, B. T. 2001, ApJ, 548, 296

Williams, R. M., Chu, Y.-H., & Gruendl, R. 2006, AJ, 132, 1877

van Diedenhoven, B., Peeters, E., Van Kerckhoven, C., et al., 2004, ApJ, 611, 928

Vancura, O., Blair, W. P., Long, K. S., & Raymond, J. C. 1992, ApJ, 394, 158

Vermeij, R., Peeters, E., Tielens, A. G. G. M., & van der Hulst, J. M. 2002, A&A, 382, 1042

Chapter 5

Conclusions

As summarized below, in this thesis, I have presented a statistical study of infrared (IR) supernova remnants (SNRs) in the Large Magellanic Cloud (LMC). In addition, toward a specific SNR, N49, I have carried out studies about PAH emission in the SNR. For the statistical study, a large amount of survey data from two IR space telescopes, *AKARI* and *Spitzer*, are used, which enables us to examine the IR characteristics of all LMC SNRs coherently and to compare the IR emission to other wavelength emission from previous multi-wavelength surveys. 28 out of 45 SNRs in the LMC show detectable IR emission, and their properties are investigated. By comparison with X-ray and radio, dust heating process by hot plasma and the IR-radio correlation can be studied. The origin of the IR emission can be inferred by their IR band ratios, but note that it is necessary to confirm the origins by using more direct evidence such as IR spectra or narrow filter images. We can confirm that the current theory on dust heating by hot plasma can well explain the dust temperature inferred by the observed MIR band ratios.

Although PAH emission is regarded as a one of the primary origins for the IR emission from SNRs, only few observational evidence has been reported so far. Our detection of the 3.3 μm PAH feature in N49 is the first case to show that the PAH feature exists in a SNR, and the detection of this feature can be accomplished by

using *AKARI* NIR spectroscopic observations. Combined with other PAH features at longer wavelengths, characteristics of PAHs inside a SNR can be investigated, which turns out that they are mainly neutral and small in size. This is interesting because it is thought that small dust/grains are preferentially destroyed after they are swept up by SNR shocks. Thus, this can suggest that the PAHs can survive where dense medium can protect them against complete destruction. Also, we can find that sufficient heating sources such as UV photons around the dense medium is essentially required to produce the PAH emission. Finally, the LMC where the IR confusion from back/foreground sources is relatively inconsiderable, is an ideal place for the above studies. I expect that the current results could be useful to interpret IR characteristics of extragalactic SNRs in more distant galaxies.

5.1 Statistical study of IR SNRs

All 45 confirmed SNRs in the LMC are observed by the *Spitzer* SAGE survey, and 21 SNRs are included in the *AKARI* LMC survey (Table 2.1). We have systematically examined the *AKARI* images in 3 (N3), 7 (S7), 11 (S11), 15 (L15), and 24 (L24) μm bands, and detected nine SNRs with associated IR emission (Table 2.2). All over the LMC, 28 SNRs out of 45 show IR emission in the *Spitzer* IRAC (3.6, 4.5, 5.8, and 8.0 μm) and/or MIPS (24 and 70 μm) bands. Among them, IR emissions of 13 SNRs in the *Spitzer* bands are firstly identified by this study.

All 28 SNRs detected in the IR bands show emission features in the MIPS 24 μm band, and most of them also have similar morphologies at 70 μm. 19 SNRs show NIR emission in one or more IRAC bands. Some SNRs have different morphologies between the IRAC and the MIPS bands, which might arise from different emission mechanisms. For the nine sources detected in the *AKARI* survey, we see clear MIR emission features in the S11, L15, and L24 bands. The *AKARI* L24 images are consistent with the corresponding *Spitzer* 24 μm images. The S11 and L15 images are new in these wavebands and show that individual SNRs have compatible

morphologies with those of the L24 bands. This suggests that the MIR emissions in these three bands are of the same origin.

There is a linear correlation between the MIR fluxes (i.e., *AKARI* L15 and L24, *Spitzer* 24 and 70 μm). Adopting the modified blackbody, the 24 and 70 μm fluxes can be described by a dust component with temperature of 40 to 100 K and mass of 0.1 to 200 $M_{\odot}$ regardless of the emission mechanisms. In the $S11/L15$ flux ratio versus $L15/L24$ flux ratio diagram, the SNRs are well aligned along a track of thermal dust emission. Type Ia SNRs are located in the lower left with low ratios while Type II SNRs are spread from low to high ratios. The alignment along the dust emission line does not necessarily imply that the origin of the MIR emission is thermal dust continuum because the SNRs dominated by ionic lines (or synchrotron emission) can have colors similar to modified blackbodies in this diagram. However, the diagram is still helpful to distinguish between line-dominated and dust-dominated SNRs taking account of their physical contexts. For those detected in the IRAC bands, their IRAC colors are examined, which is useful to interpret the origin of the IR emission. More than half of the remnants have colors expected for a SNR associated with molecular shocks whereas a few have similar colors of either PAH emission or ionic shocks. Here, again, some SNRs dominated by ionic line emission show IRAC colors for molecular shocks, which suggests careful interpretation of the IR origin based on the IRAC colors only. Meanwhile, in the MIR color-color diagram, young SNRs and old SNRs are likely to show a different tendency, and this might reflect the association between the evolution of a SNR and the IR emission mechanism.

The 24 μm fluxes (both *AKARI* L24 and *Spitzer* MIPS 24 μm) have a good correlation with X-ray fluxes. This is indeed predictable because the two emission mechanisms are physically related. Dust continuum is considered as a primary origin of MIR emission, which arises from collisional heating by hot plasma emitting X-ray emission. The *Spitzer* 70/24 μm flux ratios tend to decrease while the X-ray brightness incerease. This trend can be explained by the fact that a higher dust temperature arises from a higher gas density in a bright X-ray emission region.

The relative strength of IR and X-ray flux (IRX ratio) can be an indicator of the dominant cooling mechanism of SNRs, and the IRXs of the SNRs mostly suggest that the IR cooling is dominant. The MIR fluxes also show a correlation with radio fluxes. The *AKARI* samples show a tight correlation between the MIR and radio. This correlation is remarkable considering that there is no direct physical connection between the two. The correlations might be due to their common dependence on the physical parameters of SNRs, particularly the density of the ambient medium. However, the correlation becomes weaker using more samples from the *Spitzer* data. This reflects that the newly detected IR SNRs have fainter IR emission with respect to their radio brightness, and the correlation might be valid to only IR bright SNRs. With more samples, the correlation yields the ratio of 24 μm to 21 cm radio fluxes (q_{24}) of 0.14, which is lower than those measured in other galaxies. This might indicate that the contribution of SNRs to the 24 μm emission in the LMC would be very small.

The detection rate of IR SNRs in the LMC is remarkably high ($\sim 62\%$) compared to that of Galactic SNRs ($\sim 30\%$). The major reason is more likely to be less IR confusion by Galactic disk, and we cannot find any intrinsic differences between the LMC and the Galaxy that augment the detection rate. Based on the IR colors and their morphological comparison to X-ray, optical, and radio, we classify the origin of the IR emission into five groups; Eleven SNRs are dominated by dust continuum, seven by ionic line emission, four by molecular line emission, five by PAH emission, and one by synchrotron emission. Some ionic-line dominated SNRs could have contribution of molecular line emission, too.

We could not detect IR emission from SNRs that have low equilibrium temperature (≤ 50 K), which suggest that the plasma properties can be good indicators of the IR visibility. Dust heating and cooling physics can be examined by using dust temperature and plasma properties. There is a trend between the equilibrium temperatures and the *Spitzer* 24/70 ratios, and the 24/70 ratios clearly show the dependency on the electron density. We derive dust temperatures of $\sim 90-190$ K for

the SNRs dominated by dust emission by fitting spectral energy distribution (SED) with the *AKARI* MIR fluxes (S11, L15, and L24). Their L15/L24 color temperatures are generally higher than the *Spitzer* 24/70 μm color temperatures, which suggests that the dust emission model at single equilibrium temperature cannot describe the full SED of these SNRs. It also implies that understanding of the full SED is essential in estimating the dust destruction rate of grains by SNR shocks.

5.2 PAH emission in a SNR

Using the *AKARI* spectroscopy, we obtain IR spectra from most of the bright eastern regions including distinct filaments in N49. For N49, we are able to make its spectral line maps and have compared the distribution of different emission features in N49. In the *AKARI* IRC spectra ($2.5 - 5$ μm), we detect 3.3 μm polycyclic aromatic hydrocarbon (PAH) band features with several strong hydrogen recombination lines and moderate H_2 molecular lines. *To our knowledge, this is the first time that we observe the presence of the 3.3 μm PAH feature related to a SNR.*

The 3.3 μm PAH feature in the spectra are clearly distinguished from other shocked ionic/molecular lines in terms of the line width and the intensity variation with position. In the *AKARI* line maps of N49, the distribution of the 3.3 μm PAH emission shows overall association with those of other emissions such as Brα and H_2 1-0 O(3), which indicates that the PAH emission indeed originates from the SNR and is associated with both ionic and molecular emission. In addition, there are morphological dissimilarities among the line maps in a local scale probably reflecting the different physical conditions such as shock velocity, and preshock density in each region. The morphological characteristics of PAH emission in N49 are also clarified and confirmed by comparison to archival *Spitzer* 8 μm, *HST* Hα, and H_2 2.12 μm images obtained at *AAT*.

Overall distribution of the 3.3 μm PAH emission in N49 is more similar to that of the H_2 emission in a sense that the H_2 emission is spatially confined but the

Brα emission is extended over a large area. In addition, the 3.3 μm PAH emission is extended beyond the eastern shock boundary with the intensity comparable to those in the inner regions. These indicate that the PAH emission is possibly associated with the interacting molecular cloud, the center of which nearly coincides with the bright PAH emission region. Meanwhile, the peak position of the PAH emission is not matched with that of the H_2 emission but rather close to that of the Brα emission. In addition, the PAH emission is relatively faint at the peak of the H_2 emission.

We find signatures of other PAH features, C-C stretching modes at 6.2 and 7.7 μm and C-H out-of-plain bending mode at 11.3 μm in the archival *Spitzer* IRS SL spectra ($5.2 - 14.5$ μm) of N49. We derive the band ratios of PAHs, $I_{6.2}/I_{11.3}$ and $I_{7.7}/I_{11.3}$ from the IRS spectra ($I_{6.2}/I_{11.3} = 0.63 \pm 0.31,\ I_{7.7}/I_{11.3} = 1.25 \pm 0.26$), which implies that the PAHs in N49 are dominantly neutral. This is consistent with the theoretical expectation for shocked PAHs in dense molecular clouds. It is found that the ratios follow the universal linear correlation between the two ratios in literatures. We try to associate the $I_{6.2}/I_{11.3}$ ratio with the physical quantity $G_0\sqrt{T}/n_e$ by using the empirical relation in Galliano et al. (2008) under the assumption that the shock radiation is the dominant heating mechanism of PAHs in a very dense clump. In addition, the relatively high $I_{6.2}/I_{7.7}$ and $I_{3.3}/I_{11.3}$ ratios (0.50 ± 0.27 and ~ 0.36, respectively) indicate the existence of small PAHs according to the numerical studies (Draine & Li 2001; Mori et al. 2012). These results are consistent with the PAH formation by fragmentation from larger carbonaceous grains but not with the preferential destruction of small PAHs in shocked gas.

The morphological features of the PAH emission can be attributed to the different mechanisms of SNR shocks in terms of PAH processing. For the PAH emission associated with either shocked H_2 gas or (shocked) ionic gas, or both, PAHs must exist in dense gas where the shocks have been sufficiently retarded (even terminated) to avoid the complete destruction. Depending on the shock velocity and the preshock density, the PAH emission can be associated with either the ionic gas or the molecular

gas. Although PAHs can survive a slow shock, detectable PAH emission may not arise due to the lack of UV radiation in a certain condition. For the PAH emission outside the SNR, the radiative precursor could be responsible for the excitation. For PAHs to exist and radiate in SNRs, an ambient dense medium and a sufficient heating source around the medium are most likely to be required.

Appendix A

Brief descriptions on IR SNRs in the LMC

A.1 SNR 0450–70.9 (Figure A.1)

SNR 0450–70.9 is one of the largest SNR in the LMC. Its optical extent is $6'.5 \times 4'.7$ (98×70 pc at 50 kpc, R. Williams et al. 2004), and its IR size is seen even larger than those seen in optical or radio. The IR emission well corresponds to the rim of the radio emission and can be detected in all IRAC and MIPS bands. The overall morphology shows an elliptical shell. While the IR emission in the west is continuous, only patchy emission is identified in the east. The brightest region in the northwest contains a point source, which was identified as a source of IR cirrus (IRAS 04505–7052, Strauss et al. 1992). To avoid any contamination by this IR source, the area near the source is excluded for the flux estimation of the SNR (see Figure 2.6).

In optical, outer shell and interior filaments are shown, and a high [S II]/Hα ratio is detected (R. Williams et al. 2004, and references therein). It is found that most phenomena of the remnant observed at various wavelengths can be understood by the evolved stage of the SNR (R. Williams et al. 2004). Using theoretical models for thermal X-ray emission of the SNR, a lower limit of the SNR age is derived as

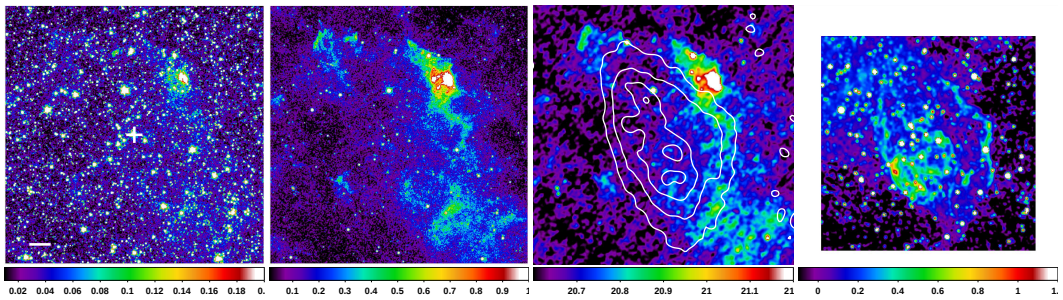

Figure A.1 *Spitzer* 3.6, 8.0, and 24 μm images of SNR 0450–70.9. For comparison, its flux-calibrated MCELS Hα image is also shown. The contours in the 24 μm image are from *ATCA* 4.8 GHz image, and the levels are 1, 3, 5, and 7 mJy beam^{-1}. Hereafter (to Figure A.13), the cross in the first image marks the center position of the SNR listed in Table 2.1, and the scale bar corresponds 1 $'$ (i.e., 15 pc at 50 kpc). All images are smoothed with a three-pixel Gaussian. The units on the colorbar of the *Spitzer* images are MJy sr^{-1}, and the MCELS is 10^{-5} erg cm^{-2} s^{-1}. North is up, and east is to the left.

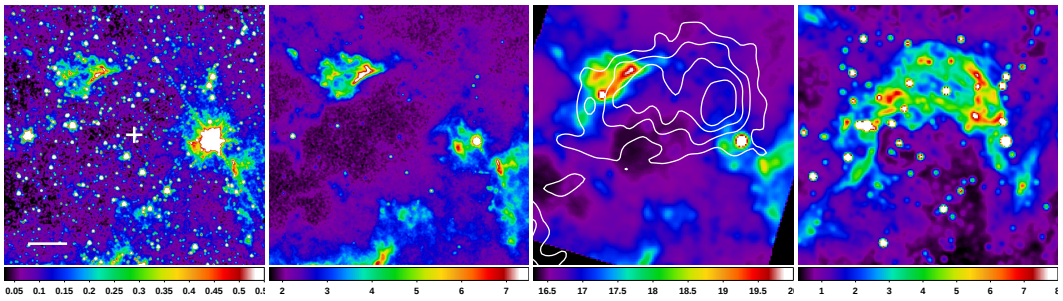

Figure A.2 *Spitzer* 3.6, 8.0, and 24 μm and flux-calibrated MCELS Hα images of SNR in N4 (SNR 0453–66.9). The contours in the 24 μm image are from *ATCA* 4.8 GHz image, and the levels are 1.5, 2, 2.5, and 3 mJy beam^{-1}.

$\sim 45,000$ yr. No evidence of a pulsar/PWN has been detected at X-ray nor radio, and there is no H II region or OB stars near this SNR (Chu & Kennicutt 1988). These facts might prefer the origin of Type Ia SN, but more direct evidences are required to confirm the origin of the remnant.

A.2 SNR in N4 (Figure A.2)

The IR images of SNR in N4 show a bright northeast region and patchy emission at south. A shell-like morphology is seen at 24 μm. An inward boundary of the northeast region is noticeably sharp, which adjoins the boundary of the optical emission. The IR emission of this region is distributed along the rim of the radio emission. In optical, a incomplete shell with filaments is seen, but no emission related to the SNR is identified at south. Also, no radio continuum is detected at south.

A.3 SNR 0453–68.5 (Figure 2.4, *top first*)

This middle-aged SNR ($\sim 13,000$ yr) shows a clear shell structure that well corresponds to the X-ray morphology. There are several bright knots along the rim, and the shell is filled with diffuse emission. Inside the shell, some bright emission is also seen at the center. Recently, Gaensler et al. (2003) find the presence of a PWN at the center based on the radio and X-ray observations. The PWN properties most closely resemble those of the Galactic SNR Vela, and the elongated morphology of the PWN can indicate compression by the SNR reverse shock. The enhanced IR emission at the center might be associated with the PWN, but it is necessary to confirm it further. The bright emission seen at the southwest of the SNR is not related to the SNR.

A.4 N11L (Figure A.3)

The IR emission of N11L at 4.5 μm with no emission at 8.0 μm is detected by R. Williams et al. (2006), and the IR morphology is similar to that seen in optical. Due to the partial coverage, IR emission in the 3.6 and 5.8 μm IRAC bands and all MIPS bands could not be distinguished. Using the SAGE data, all IRAC and MIPS images can be investigated, and the IR emissions with similar morphology to that seen at 4.5 μm are detected in all bands except 8.0 μm.

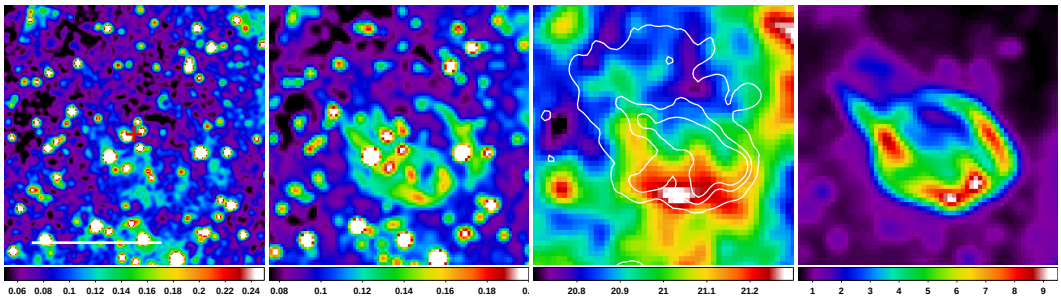

Figure A.3 *Spitzer* 3.6, 4.5, and 24 μm and flux-calibrated MCELS Hα images of SNR N11L (SNR 0454–66.5). The contours in the 24 μm image are from *Chandra* X-ray image ($0.3-2.1$ keV), and the levels are 2, 6, and 10 $\times 10^{-8}$ counts cm^{-2} s^{-1}.

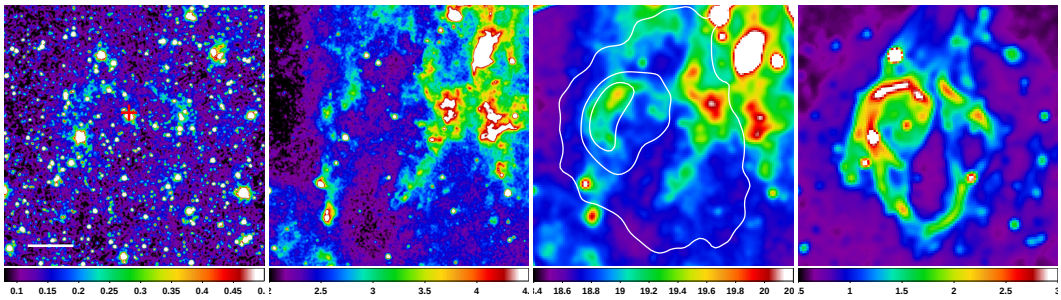

Figure A.4 *Spitzer* 4.5, 8.0, and 24 μm and MCELS Hα images of SNR N86 (SNR 0455–68.7). The contours in the 24 μm image are from *ATCA* 4.8 GHz image, and the levels are 1.3, 4.65, and 8 mJy beam^{-1}. The units on the colorbar of the MCELS is ADU s^{-1}.

This SNR shows a shell morphology with signatures of a breakout toward north-east. Filamentary emissions protruding from the shell are seen in optical and IR bands while diffuse emission is distributed on the north of the shell in X-ray and radio. Besides the morphological structures, optical echelle spectra of N11L suggest kinematic evidences that velocity profiles through the shell and filamentary loops seen in optical show rapidly moving material along the filaments (R. Williams et al. 1999). The breakout in N11L can implicate a low-density cavity outside the SNR surrounded by a structure on the western periphery of the N11 H II complex.

A.5 N86 (Figure A.4)

N86 shows faint IR emission in all *Spitzer* bands, but the emission in the west of the SNR is difficult to be discriminated from the emission of other sources. However, hook-shaped IR emission in the east is discernible and shows good correlation with optical and radio emission. Similarly to N11L, N86 has a large breakout to the north as well as smaller outflow structures around the SNR, which can be seen in optical images (R. Williams et al. 1999). However, these features are not detected in the IR bands.

R. Williams et al. (1999) found that a well-defined spherical expansion pattern and faint diffuse X-ray emission in the breakout. The expending velocity of the material breaking out to the north is measured up to 100 km s^{-1} based on the optical spectroscopy. The existence of hot gas and the faster expending velocity indicate that material from the SNR is moving to less dense medium through the breakout. Although N86 is relatively away from H II complexes or superbubbles, the presence of the breakout could imply a complicated structure of its local surrounding medium.

A.6 DEM L71 (Figure 2.4, *top second*)

DEM L71 is one of the Balmer-dominated SNRs in the LMC. It has a well-defined shell morphology with the bright emission at the east and west limb. The IR morphology is in good agreement with that of X-ray. This SNR shows very faint emission at radio wavelengths relative to the IR emission unlike the other Type Ia Balmer-dominated SNRs (Table 2.1). *Chandra* X-ray observations reveal a double-shock morphology consisting of a blast-wave interacting with the surrounding ISM and a reverse shock heating ejecta at the central region (Hughes et al. 2003). By optical spectroscopy, broad and narrow components of Hα emission have been confirmed, which is a characteristic of nonradiative shocks in partially neutral gas (Ghavamian et al. 2003).

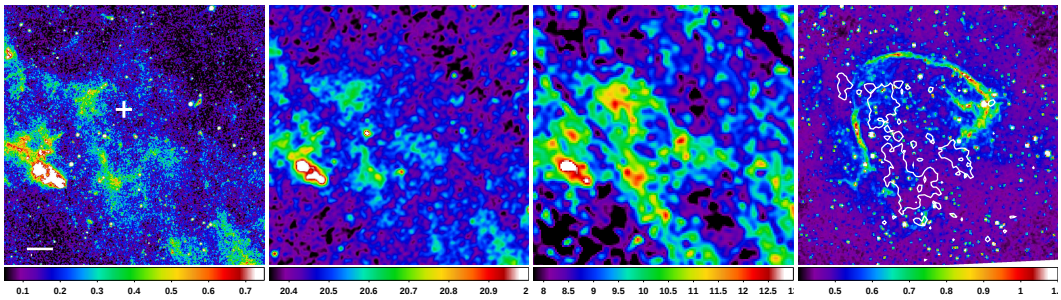

Figure A.5 *Spitzer* 8.0, 24, and 70 μm and MCELS Hα images of SNR DEM L72 (SNR 0506–65.8). This SNR has neither X-ray nor radio data, so no contour can be overlaid. Contours in the Hα image represent 0.2 MJy sr^{-1} level of star-subtracted 8.0 μm image.

A.7 N23 (Figure 2.4, *top third*)

The IR emission seen at 24 μm is highly asymmetric showing bright emission in the southeast but faint (or no) emission in the northwest. Such morphology is also seen in X-ray and optical bands. This can be explained by a considerable gradient of the ambient medium density probably due to the proximity to the open cluster HS114 which is located toward the southeastern side of the SNR (see Hughes et al. 2006, and references therein). Recent *Chandra* observations reveal the existence of a compact source detected in the hard X-ray band ($>$ 2 keV, Hughes et al. 2006; Hayato et al. 2006). The position of the source is nearly the center of the remnant, which makes its association with the SNR more plausible. This object can be a pulsar (or PWN) or a neutron star related to the remnant although any observational evidence at different wavelengths including IR cannot clarify the origin of the source.

A.8 DEM L72 (Figure A.5)

IR images of DEM L72 show the emission of "L" shape in 8, 24, and 70 μm bands. The IR emission is well enclosed with an optical shell. Since this SNR is outside of the *ATCA* survey, and the morphology of the IR emission cannot be compared to that of radio continuum. Besides, although Klimek et al. (2010) found that optical

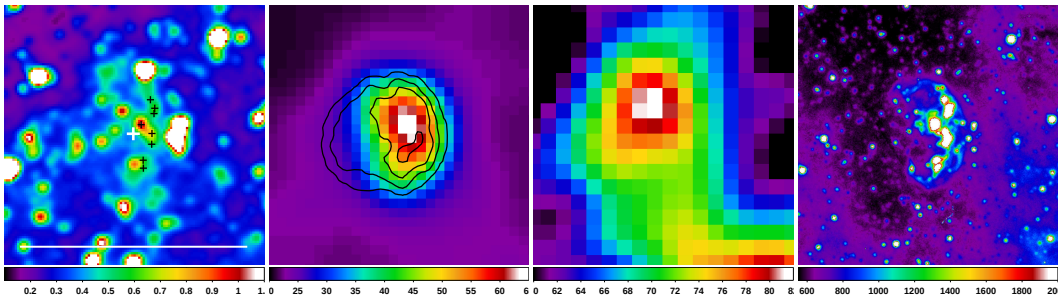

Figure A.6 *Spitzer* 4.5, 24, and 70 μm and VLT (Very Large Telescope) Hα images of SNR N103B (SNR 0509–68.7). Black crosses in the 4.5 μm image are marked on the positions of knots discernible in Hα. The contours in the 24 μm image are from *Chandra* X-ray image ($0.3 - 10$ keV), and the levels are 0.1, 1.2, 4.5, and 10 $\times 10^{-6}$ counts cm^{-2} s^{-1}.

shell is filled with diffuse X-ray emission by using *XMM-Newton* data, however, the distribution of the X-ray emission is more enhanced in the northwest where there is no IR emission detected. DEM L72 is one of the largest SNR in the LMC, and faint filaments extending to the northeast from the bright optical shell are visible, especially in [O III]. Taking them into account, the angular size of this SNR can reach up to $9'$ (or 135 pc at the distance of 50 kpc). Its age is estimated to $\sim$ 100 kyr, well into the relatively late stage of SNR evolution. This SNR seems to have similarities to another evolved object, SNR 0450–70.9 (see §A.1), and further studies on these mature SNRs could improve our knowledge about the last stage of SNR evolution.

A.9 N103B (Figure A.6)

IR emission of N103B at 24 μm has a well-defined shell morphology, which shows good correlation to that seen in X-ray. The IR emission is enhanced in the west, which can be seen in X-ray and Hα, too. The 70 μm image of the SNR also shows a shell-like structure, but the distribution of the emission is somewhat different from that of the emission in 24 μm. In shorter wavelength bands, only IR knots are detected above the background level (denoted by black crosses in Figure A.6). The

locations of the knots are well coincident with those of knots seen in Hα. In addition to the knotty emission, filamentary emissions along the western rim are visible with diffuse emission in Hα.

N103B is a young SNR ($\sim$ 860 yr based on the light echo Rest et al. 2005) and is one of the interesting objects among the LMC SNRs. Its proximity to the young star cluster NGC 1850 ($\sim$ 40 pc) led that the progenitor of the SNR was a massive star from the cluster (Chu & Kennicutt 1988). Moreover, overabundance of O, Ne, and Mg seen in the $XMM-Newton$ emission-line spectra also supports the Type II SN origin (van der Heyden et al. 2002). However, a *Chandra* ACIS observation reveals the distribution of the ejecta and the large mass of Fe (0.34 $M_{\odot}$) that are in favor of a Type Ia SN than of a Type II SN (Lewis et al. 2003). More recently, Badenes et al. (2009) suggest that N103B is associated with recent star formation and could be a "prompt" Type Ia SN of which progenitor is relatively younger and more massive before the explosion. It is expected that more detailed investigation on the IR emission could provide convincing evidence for its progenitor.

A.10 SNR 0509–67.5 (Figure 2.1, *top row*)

This Balmer-dominated remnant is one of the youngest SNRs in the LMC, and its X-ray spectra indicate that it originated from Type Ia SN explosion (Hughes et al. 1995). There is a bright, elongated feature in the southwest of the SNR in the MIR-L bands, and it coincides with the brightest portion of the shell structure seen in both the X-ray and optical images (Borkowski et al. 2006a). S11 and S11-S7 images also show emission at the same position. Because it is faint, the morphologies in the S11 and S11-S7 are not clear. In addition to the bright southwestern limb, in the L24, the faint emission from the rest of the SNR is visible as seen in the X-ray and optical. The bright point-like source just outside the southwestern boundary of the contour in the S11 is a background source (2MASSJ 05092882-6731307).

A.11 SNR 0519–69.0 (Figure 2.1, *second row*)

This is another young Balmer-dominated SNR probably originating from Type Ia SN explosion (Hughes et al. 1995; Ghavamian et al. 2007). The shell structure well-defined in Hα and X-ray is clearly seen in the MIR-L bands. Also, it shows three bright knots in the north (N), east (E), and southwest (SW) along the limb. While only the N and the E knots are visible in the S11 image, all three knots are clearly visible in the S11-S7 image with the morphology nearly identical to those of the MIR-L. The N and the E knots spatially correspond to the relatively bright region in X-ray and Hα, whereas the SW knot does not have specific counterpart in those bands. This discrepancy of the knots indicates the different characteristics among them.

A.12 N132D (Figure 2.1, *third row*)

This SNR belongs to young oxygen-rich SNRs that are the product of the core-collapse SNe (Morse et al. 1995). The remnant is one of the brightest LMC SNRs and shows a well-defined shell structure in the MIR bands as in the X-rays. The southeastern (SE) rim contains enhanced IR emission which might be caused by the interaction with a molecular cloud in this area (Banas et al. 1997; Tappe et al. 2006). Only the bright SE shell is visible in the S11 band together with the northwestern knot named "West Complex" by the previous optical observation (Tappe et al. 2006). However, the S11-S7 image shows the morphology just same as that of the MIR-L bands. The central bright emission in the S11 band, showing weak correlation with X-ray, might be mainly attributed to background emission. The IR morphology is somewhat different from that of the optical which shows relatively fainter shell compared to the bright ejecta region at the center (Borkowski et al. 2007). Using the *Spitzer* IRS observations, Tappe et al. (2006) reveal the dominant dust continuum with the first detected PAH emission.

A.13 N49B (Figure 2.1, *bottom row*)

This is a middle-aged SNR of core-collapse SN origin (Hughes et al. 1998; Park et al. 2003). The SNR shell is clearly seen in the MIR-L bands, and its morphology is similar to that in X-ray. The SNR has several patchy emission along the limb including the particularly bright southern rim in the MIR-L bands. There is some diffuse IR emission in the inner region with a belt-like feature crossing the shell. Even though the S11 image does not show prominent emission related to the SNR, the S11-S7 image reveals some emission such as the southern rim, the belt-like feature, and the northwest shell similar to the features in the MIR-L bands.

A.14 N49 (Figure 2.2, *top row*)

This Type II SNR is unique in showing very strong emission in all IRC bands. Previous X-rays and radio observations show fairly clear emission over the entire shell of the SNR with the peak in the east (R. Williams et al. 2006). While the IRC images also show the similar morphology, the IR peak has a different position from the X-rays/radio. Besides, the SNR has a lack of IR emission in the northwest unlike the X-rays/radio although the complete shell of the X-rays/radio is marginally detected in the MIR-L bands. A bright wedge-shaped feature in the east is clearly visible in all IRC bands, which is quite similar to that seen in the *HST* observations (Bilikova et al. 2007). Also, the overall IR morphology has good correspondence to that of optical. In the *S7* band, there appears a protrusion that extends to east from the wedge-shaped filament. Since the structure extends beyond the SNR boundary, it is not likely to be physically associated with the SNR. But it is worth to note that it is spatially coincident with the ambient molecular cloud possibly interacting with the SNR (Banas et al. 1997).

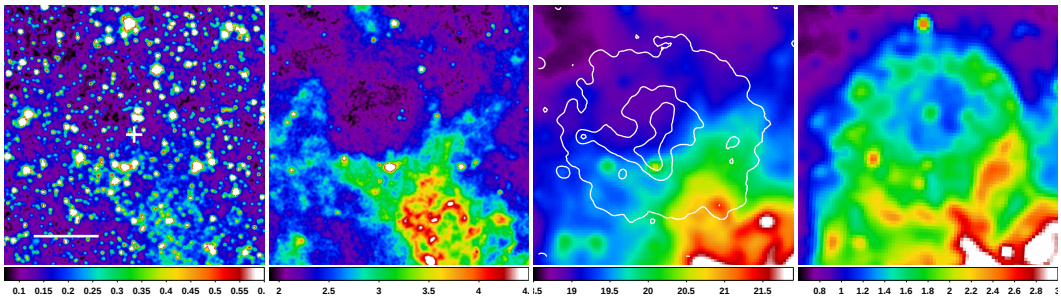

Figure A.7 *Spitzer* 3.6, 8.0, and 24 μm and MCELS Hα images of SNR in N206 (SNR 0532–71.0). The contours in the 24 μm image are from *Chandra* X-ray image ($0.3 - 10$ keV), and the levels are 5, 9, and 13 $\times 10^{-8}$ counts cm^{-2} s^{-1}.

A.15 SNR in N206 (Figure A.7)

IR emission of SNR in N206 is not isolated from that of its surrounding medium, which makes it difficult to disentangle IR emission associated with the SNR from other emission. While no IR emission associated with the SNR is detected in the north, patchy shell-like emission is identified, which spatially corresponds to the well-defined optical shell. The southern areas are confused by the bright ambient medium (possibly periphery structures of N206 H II region), so the eastern rim is only used for its flux estimation. While bright X-ray emission is observed at the center of the SNR, IR and optical (and radio) emissions show largely shell-like morphology. This fact makes the SNR categorized as "mixed morphology" SNR. Recently, R. Williams et al. (2005) performed new radio observations by using the *ATCA* and found an elongated, radially oriented features across the SNR. In the *Chandra* images, X-ray emission associated with this radio feature is also detected, which suggests that this feature originates from a PWN.

A.16 DEM L238 (Figure 2.4)

We could detect distinct IR emission of this SNR in only 24 μm. Although the emission at 24 μm is somewhat confused by surrounding emission, the southeastern

shell and the northwestern shell are distinctly identified showing good correlation to a shell seen in optical. As the northern shell in optical is brighter than the southern, the IR shell also shows the same tendency. This enhancement might be explained by that SNR shocks encounter denser medium in the north. Besides, the IR shell is in moderate agreement with the faint X-ray shell, but the X-ray emission has a bright central region unlike the IR.

This SNR is moderately old ($\sim 10^4$) yr, of which Fe abundances in X-ray spectra are interestingly high (Borkowski et al. 2006b). This Fe overabundance suggests that DEM L241 is a result of Type Ia explosion. In view of a Type Ia SN, the presence of Fe-rich ejecta at the center of this SNR is unexpected, because usual Type Ia SNRs have faint ejecta emission in the middle stage of their evolution. This fact might indicate that a dense CSM is present around the progenitor, which is one of the characteristics for more massive Type Ia progenitors ("prompt" Type Ia).

A.17 SN 1987A (Figure 2.2, *second row*)

This newly formed SNR has just started its interaction with dense circumstellar material around the inner ring (e.g., Park et al. 2005)). The effect of this encounter has been detected as a rapid brightness change at various wavelengths including IR (Bouchet et al. 2006). *AKARI* observed this SNR at Oct. 31 – Nov. 4, 2006 (day 7190–7194) and the estimated flux agrees with the IR flux variation found by the recent *Spitzer* study (Dwek et al. 2008). The remnant appears point-like in all IRC bands, but the previous observation with higher resolution shows the resemblance with X-rays rather than optical in terms of the brightness distribution (e.g., see Figure 3 and 16 in Bouchet et al. 2006). The ring-like feature around the SNR in the MIR-L bands is the shape of point-spread-function (PSF) of the IRC.

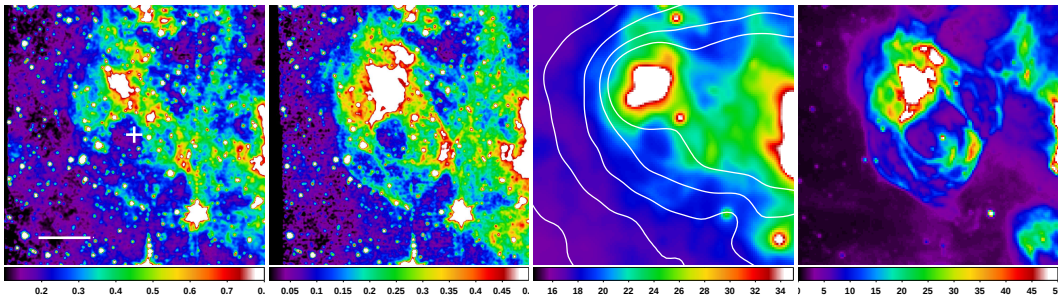

Figure A.8 *Spitzer* 3.6, 4.5, and 24 μm and flux-calibrated MCELS Hα images of SNR DEM L241 (SNR 0536–67.6). The contours in the 24 μm image are from *ATCA* 4.8 GHz image, and the levels are 3, 4.75, 6.5, 8.25, and 10 mJy beam^{-1}. The bright extended source at North is H II region.

A.18 N63A (Figure 2.5, *second row*)

N63A is located in the periphery of a lager H II region, N63, and it is a relatively young SNR (2000–5000 yr, Hughes et al. 1998). In all *Spitzer* bands, a three-lobed structure is seen, which is also observed in optical (e.g., R. Williams et al. 2006). In the 24 μm band, the remnant also shows a complete shell structure that well corresponds to the morphologies seen in radio or X-ray (e.g., Dickel et al. 1993; Warren et al. 2003). In particular, crescent features seen in X-ray faintly but apparently appear at 24 μm. Characteristics of the three lobes are interesting, because the two eastern lobes show evidence of shock ionization (e.g., high [S II]/Hα ratio) while the western lobe shows that of photoionization (Levenson et al. 1995). However, the IR spectral energy distribution (SED) of the western lobe is unexpectedly similar to the SED of the eastern lobe, and the northeastern lobe shows the most different SED from the others (R. Williams et al. 2006).

A.19 DEM L241 (Figure A.8)

IR images of DEM L241 show a shell-like structure with interior looped filaments. In particular, the 4.5 μm image depicts the IR shell most clearly. The IR morphology is similar to that seen in optical. The enhanced emission in the western rim is visible

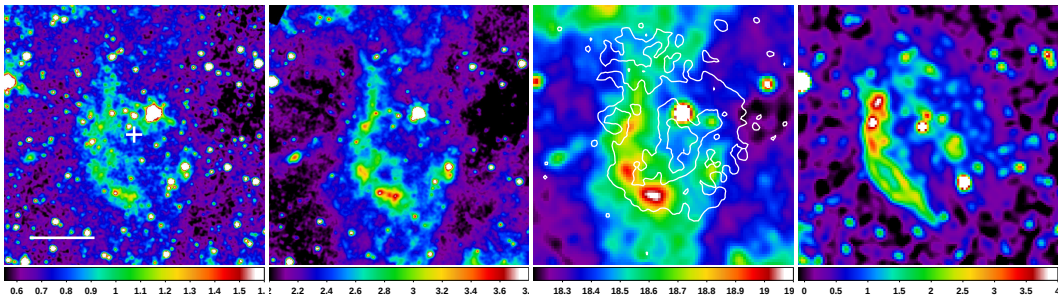

Figure A.9 *Spitzer* 5.8, 8.0, and 24 μm and flux-calibrated MCELS Hα images of SNR DEM L249 (SNR 0536–70.6). The contours in the 24 μm image are from *Chandra* X-ray image ($0.3-10$ keV), and the levels are 2, 8.5, and 15 $\times 10^{-8}$ counts cm^{-2} s^{-1}.

in all *Spitzer* bands, while other structures are distinct in only few bands. The western rim is largely brighter than the eastern rim, which might result from the denser medium in the west. The bright emission region in the north is an H II region, so that area is excluded for the flux estimation.

Recent *XMM-Newton* data reveal the head-tail structure of X-ray emission with a point source in it (Bamba et al. 2006). The luminosity and spectrum of the source indicates that the source could be a PWN of DEM L241. Moreover, overabundance in O and Ne with the existence of a nearby OB association (LH 88) implies a very massive progenitor of the SNR with more than 20 $M_{\odot}$.

A.20 DEM L249 (Figure A.9)

DEM L249 shows a circular shell morphology with some extended emission to the north from the shell in all *Spitzer* bands. In the 3.6 and 4.5 μm images, faint diffuse emission can be identified after subtracting emission from point sources. The eastern rim is brighter than the western rim, and several bright knots are present along the eastern rim. Asymmetric brightness between the east and the west is also seen in the optical morphology, but the locations of IR peaks on the rim are different from those of optical peaks. Although overall distribution of X-ray emission shows similar

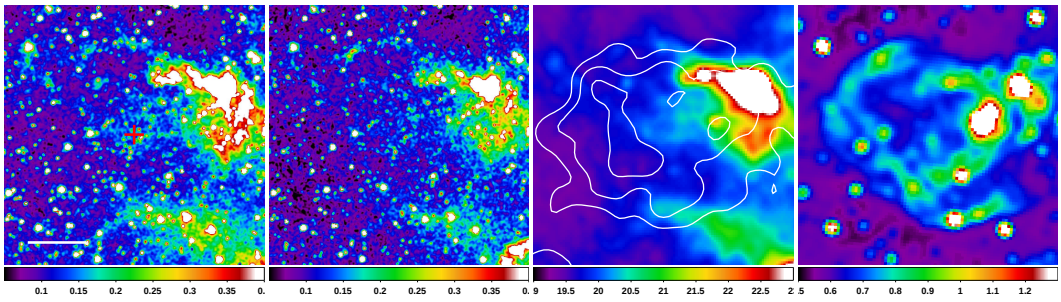

Figure A.10 *Spitzer* 5.8, 8.0, and 24 μm and MCELS Hα images of SNR DEM L256 (SNR 0536–70.6). The contours in the 24 μm image are from *ATCA* 4.8 GHz image, and the levels are 1.3, 2, and 2.7 mJy beam^{-1}.

extent to the IR shell, bright central emission surrounded by diffuse emission is observed.

This SNR has similar features in X-ray emission to DEM L238 such as bright central emission with high Fe abundances (Borkowski et al. 2006b, and see §A.16). These facts suggest that DEM L241 is a result of Type Ia explosion with a relatively massive progenitor. Further investigation is required to convince the origin of this SNR, and studies of DEM L249 together with N103B and DEM L238 could disclose the evolution of "prompt" Type Ia SNR and their influences to ambient media.

A.21 DEM L256 (Figure A.10)

Since there are several H II regions (DEM L251, 253, and 264) in the vicinity of DEM L256, the IR emission associated with the SNR is somehow confusing. This SNR has well-defined double shell morphology in optical, and the IR emission corresponding to the northern part of the outer shell can be designated in all *Spitzer* bands. In the IR images, a bright clump lies on the extended emission in the west, which has a counterpart in optical. This clump is located just outside of the inner shell and is along an extension of the outer shell. In fact, the clump is known to have lower [S II]/Hα ratio (< 0.4) unlike the other filamentary shells have much higher values (> 0.7, Klimek et al. 2010). This indicates that the clumpy emission is not associated

with the SNR, so the bright emission seen in IR bands also originates from other sources. Although the norther tip of the extended emission in the west has a good coincidence with the inner optical shell, we only used the northern shell for the flux estimation to avoid any contamination from the bright source in the west.

The two nested shells of DEM L256 invoke the bilobed structure for this SNR. Moreover, two expansion velocities observed in an echelle spectrum supports this scenario Klimek et al. (2010). X-ray images taken by *XMM-Newton* show much enhanced emission toward the outer half-shell (the eastern shell). The X-ray emission generally trace the Hα filaments. The edge where strong Hα emissions at the systemic velocity are seen together with corresponding X-ray emission, which might indicate that the SNR is encountering a dense materials.

A.22 N157B (Figure 2.2, *third row*)

This remnant is one of the two known Crab-like SNRs in the LMC. No appreciable IR emission related to the pulsar or PWN has been detected. The bright emission is mostly originated not from the SNR but from nearby sources including a small molecular cloud in the south (Johansson et al. 1998), possibly undergoing star-forming activities in progress. However, it is found that there are some features such as the horseshoe-shaped one and the arm-like emission towards the northeast in all IRC bands except the S7. These features correspond well to the Hα emission of the SNR observed by Chu et al. (1992). This indicates they are associated with N157B.

A.23 SNR in N159 (Figure A.11)

SNR in N159 is located in the H II complex N159 that contains several bright emission regions, which makes it difficult to define the SNR emission. The optical morphology of the H II complex is similar the the figure "8" consisting of northern (N) and southern (S) lobes, and the SNR emission only in the N lobe was previously known by detecting the fast expending shell (Chu et al. 1997). Recent *Chandra*

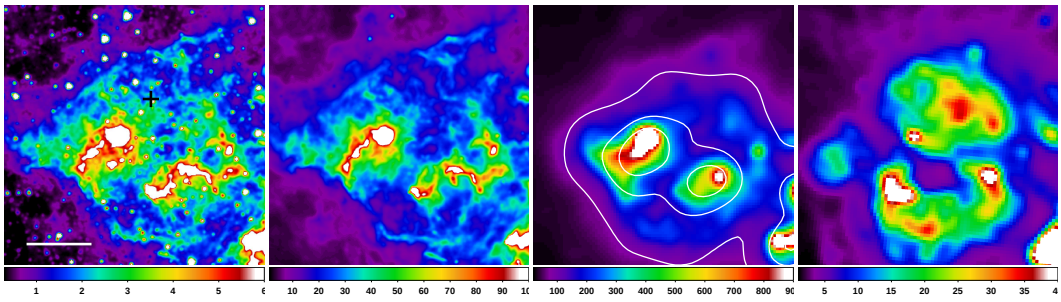

Figure A.11 *Spitzer* 3.6, 8.0, and 24 μm and MCELS Hα images of SNR in N159 (SNR 0540–69.7). The contours in the 24 μm image are from *ATCA* 4.8 GHz image, and the levels are 25, 87.5, and 150 mJy beam^{-1}. Two bright regions in the middle are not associated with the SNR, and the eastern clump is Papillon Nebula, H II blob (Seward et al. 2010, and reference therein).

observations with the MCELS data, Seward et al. (2010) can define larger SNR emission including the emission in the S lobe. After removing scattered emission from the nearby bright source LMC X-1, X-ray emissions overlapping with the N and the S lobes are identified.

IR emission in N159 shows very complicated morphology; It largely has a circular shape with several sharp filaments and some bright clumps in the middle. The two bright regions in the middle are not associated with this SNR, which are well defined by radio continuum and no X-ray emission (Seward et al. 2010). The clump in the east is a bright H II region called Papillon Nebula. A thin filament correlated with the S lobe is shown in all *Spitzer* bands, and a small shell-like structure with several filaments are found in the N lobe. For the flux estimation, we masked out the two bright regions in the middle and measured fluxes from the N lobe and the filament in the S lobe separately (see Figure 2.6).

A.24 N158A (Figure 2.2, *forth row*)

N158A is one of the well-knwon Crab-like SNRs in the LMC. There is a PWN at the center of the remnant, which is detected as a point source in the all bands of *AKARI* and *Spitzer*. No distinct emission from the shell is found unlike that seen

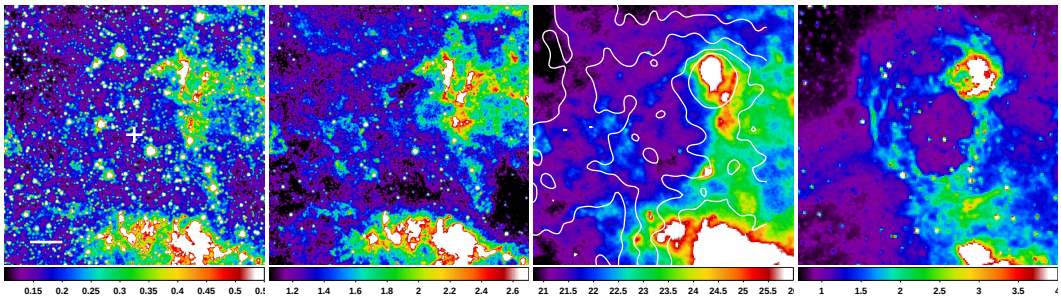

Figure A.12 *Spitzer* 3.6, 5.8, and 24 μm and MCELS Hα images of SNR DEM L299 (SNR 0543–68.9). The contours in the 24 μm image are from *ATCA* 4.8 GHz image, and the levels are 3, 4, 5, and 6 mJy beam^{-1}.

in X-ray or radio, but some diffuse emission might exist along the southern rim of the X-ray shell (see Figure 2.5). The *Spitzer* IRS spectroscopy to the PWN reveals an excess of IR emission from synchrotron emission expected from the radio and optical power laws B. Williams et al. (2008). The origin of the excess is more likely to SN synthesized dust heated by shocks generated by the PWN. Moreover, several emission lines such as [S III] λ18.71 μm and [Si II] λ34.82 μm, are detected in the spectra as the Crab nebula shows. The origin of line emission is most likely dense clumps of ejecta swept up by highly radiative shocks.

A.25 DEM L299 (Figure A.12)

SNR DEM L299 is located on the northwestern periphery of the ringshaped nebula, DEM L299. IR emissions of DEM L299 in the IRAC bands are sporadic, and extended emissions from other sources in the west possibly obscure the emission from the SNR. The cavity seen in the 24 μm image is well confined by the shell seen in Hα. The patchy emission in the east has correspondence with the eastern rim in optical, which leads us to regard the emission as associated with the SNR. The bright extended emission in the northwest originates from a H II region photoionized by a star, Sk–68 155 and a young stellar object (Desai et al. 2010, and references therein). Since this emission is not associated with the SNR and might be extended

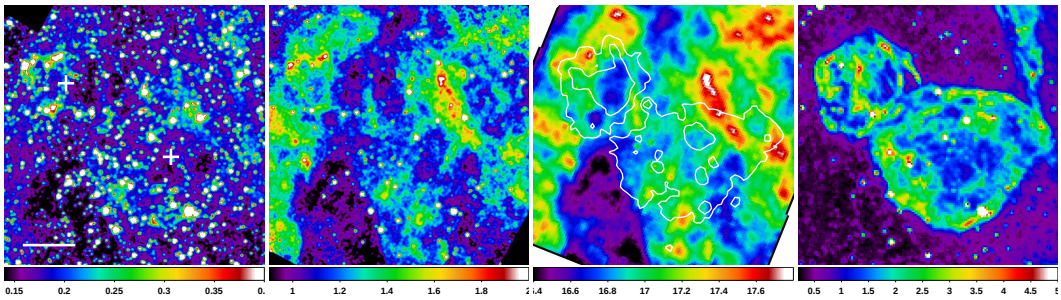

Figure A.13 *Spitzer* 4.5, 5.8, and 24 μm and flux-calibrated MCELS Hα images of SNR DEM L316A&B (SNR 0547–69.7). The contours in the 24 μm image are from *Chandra* X-ray image (0.3 – 10 keV), and the levels are 3 and 10 $\times 10^{-8}$ counts cm^{-2} s^{-1}.

to the south, we only measure fluxes from the eastern rim.

A.26 DEM L316A/B (Figure A.13)

The DEM L316 system shows an interesting double shell structure. Both SNRs show clear shell-type morphologies in optical, while they are centrally brightened with diffuse emission and several clumps in X-ray. Their IR emissions are quite confusing; L316A (the northeastern shell) shows a wedge-shape structure in the east with some confusion in the north. In the case of L316B (the southwestern shell), the southern rim has good correspondence with the optical shell while the northern region of L316B is hardly discriminated from contamination by other emissions.

DEM L316A and DEM L316B were firstly thought to be colliding each other because of their spatial adjacency (R. Williams et al. 1997). Later, their progenitor types are, however, suggested to be different based on the spectral X-ray features (L316A: Type Ia and L316B: Type II, R. Williams & Chu 2005), which makes the collision between two SNRs doubtful. Toledo-Roy et al. (2009) performed hydrodynamic simulations to delineate the observed X-ray features. They found that a non-colliding condition including thermal conduction can reproduce X-ray emission in good agreement with observational results. Their results are also in favor of

the non-colliding case, then it would be one of remaining questions that how two different types of SNRs can be formed in vicinity.

A.27 0548–70.4 (Figure 2.2, *bottom row*)

This middle aged (∼7,000 yr), Balmer-dominated SNR has been categorized into a Type Ia remnant because its observed ratio of oxygen to iron is much lower than that from typical core-collapse SNe (Hendrick et al. 2003). The shell structure detected in Hα and X-rays is not clearly seen in the IRC images while the *Spitzer* image shows the outer shell similar to the Hα/X-ray owing to its higher resolution (Borkowski et al. 2006a). Nevertheless, there is a distinct emission in MIR bands that has a spatial correspondence to the central region with X-ray emission. While the overall shape of the IR emission is similar to that of the X-rays, its brightness distribution is quite different from the X-rays. Instead, the brightness distribution of MIR emission seems closer to the Hα including the bright knot at the center.

Bibliography

Badenes, C., Harris, J., Zaritsky, D., & Prieto, J. L. 2009, ApJ, 700, 727

Bamba, A., Ueno, M., Nakajima, H., Mori, K., & Koyama, K. 2006, A&A, 450, 585

Banas, K. R., Hughes, J. P., Bronfman, L., & Nyman, L.-A. 1997, ApJ, 480, 607

Bilikova, J., Williams, R. N. M., Chu, Y.-H., Gruendl, R. A., & Lundgren, B. F. 2007, AJ, 134, 2308

Borkowski, K. J., Hendrick, S. P., & Reynolds, S. P. 2007, ApJ, 671, L45

Borkowski, K. J., Williams, B. J., Reynolds, S. P., et al. 2006, ApJ, 642, L141

Borkowski, K. J., Hendrick, S. P., & Reynolds, S. P. 2006, ApJ, 652, 1259

Bouchet, P., Dwek, E., Danziger, J., et al. 2006, ApJ, 650, 212

Chu, Y.-H., Kennicutt, R. C., Snowden, S. L., Smith, R. C., Williams, R. M., & Bomans, D. J. 1997, PASP, 109, 554

Chu, Y.-H., Kennicutt, R. C., Jr., Schommer, R. A., & Laff, J. 1992, AJ, 103, 1545

Chu, Y.-H., & Kennicutt, R. C., Jr. 1988, AJ, 96, 1874

Desai, K. M., Chu, Y.-H., Gruendl, R. A., et al. 2010, AJ, 140, 584

Dickel, J. R., Milne, D. K., Junkes, N., & Klein, U. 1993, A&A, 275, 265

Dwek, E., Arendt, R. G., Bouchet, P., et al. 2008, ApJ, 676, 1029

Gaensler, B. M., Hendrick, S. P., Reynolds, S. P., & Borkowski, K. J. 2003, ApJ, 594, L111

Ghavamian, P., Blair, W. P., Sankrit, R., Raymond, J. C., & Hughes, J. P. 2007, ApJ, 664, 304

Ghavamian, P., Rakowski, C. E., Hughes, J. P., & Williams, T. B. 2003, ApJ, 590, 833

Hayato, A., Bamba, A., Tamagawa, T., & Kawabata, K. 2006, ApJ, 653, 280

Hendrick, S. P., Borkowski, K. J., & Reynolds, S. P. 2003, ApJ, 593, 370

Hughes, J. P., Ghavamian, P., Rakowski, C. E., & Slane, P. O. 2003, ApJ, 582, L95

Hughes, J. P., Hayashi, I., & Koyama, K. 1998, ApJ, 505, 732

Hughes, J. P., Hayashi, I., Helfand, D., et al. 1995, ApJ, 444, L81

Hughes, J. P., Rafelski, M., Warren, J. S., et al. 2006, ApJ, 645, L117

Johansson, L. E. B., Greve, A., Booth, R. S., et al. 1998, A&A, 331, 857

Klimek, M. D., Points, S. D., Smith, R. C., Shelton, R. L., & Williams, R. 2010, ApJ, 725, 2281

Levenson, N. A., Kirshner, R. P., Blair, W. P., & Winkler, P. F. 1995, AJ, 110, 739

Lewis, K. T., Burrows, D. N., Hughes, J. P., et al. 2003, ApJ, 582, 770

Morse, J. A., Winkler, P. F., & Kirshner, R. P. 1995, AJ, 109, 2104

Park, S., Hughes, J. P., Slane, P. O., et al. 2003, ApJ, 592, L41

Park, S., Zhekov, S. A., Burrows, D. N., & McCray, R. 2005, ApJ, 634, L73

Rest, A., Suntzeff, N. B., Olsen, K., et al. 2005, Nature, 438, 1132

Seward, F. D., Williams, R. M., Chu, Y.-H., et al. 2010, AJ, 140, 177

Strauss, M. A., Huchra, J. P., Davis, M., et al. 1992, ApJS, 83, 29

Tappe, A., Rho, J., & Reach, W. T. 2006, ApJ, 653, 267

Toledo-Roy, J. C., Velázquez, P. F., de Colle, F., et al. 2009, MNRAS, 395, 351

van der Heyden, K. J., Behar, E., Vink, J., et al. 2002, A&A, 392, 955

Warren, J. S., Hughes, J. P., & Slane, P. O. 2003, ApJ, 583, 260

Williams, B. J., Borkowski, K. J., Reynolds, S. P., et al. 2008, ApJ, 687, 1054

Williams, R. M., Chu, Y.-H., & Gruendl, R. 2006, AJ, 132, 1877

Williams, R. M., Chu, Y.-H., Dickel, J. R., et al. 2005, ApJ, 628, 704

Williams, R. M. & Chu, Y.-H. 2005, ApJ, 635, 1077

Williams, R. M., Chu, Y.-H., Dickel, J., et al. 2004, ApJ, 613, 948

Williams, R. M., Chu, Y.-H., Dickel, J., et al. 1999, ApJ, 514, 798

Williams, R. M., Chu, Y.-H., Dickel, J. R., et al. 1997, ApJ, 480, 618

요 약

초신성 잔해는 초신성 충격파에 의한 성간물질의 물리적, 화학적 진화를 연구할 수 있는 특별한 장소이다. 특히, 충격파에 의한 성간 먼지의 공정(processing)은 초신성 잔해를 적외선 파장영역에서 관측함으로써 직접적으로 조사할 수 있다. 이 논문에서는 아카리(AKARI)와 스피쳐(Spitzer) 적외선 우주 망원경으로 수행된 대마젤란운의 관측 자료를 이용하여 근적외선부터 중적외선 파장대의 초신성 잔해 연구를 수행하였다.

우리은하와 비해 대마젤란운은 적외선 성간 소광이 적기 때문에 초신성 잔해로부터 나오는 적외선 방출을 연구하는데 매우 큰 이점을 지니고 있다. 본 연구에서는 지금까지 알려진 45개의 대마젤란운 초신성 잔해에 대하여 이들의 아카리와 스피쳐 영상들을 체계적으로 조사한 결과, 28개의 초신성 잔해로부터 식별각능한 적외선 방출을 확인할 수 있었다. 이 중, 13개의 초신성 잔해는 이 연구에 의해 처음으로 적외선 파장대에서 확인되었다. 후속 연구를 위하여 28개의 초신성 잔해들에 대한 플럭스를 측정하여 그 결과를 일반적인 정보들과 더불어 카탈로그로 정리하였다. 적외선 플럭스들 사이의 상관 관계와 적외선 색(color)을 이용하여 초신성 잔해에서 관측된 적외선 방출의 기원에 대하여 살펴보았다. 관측된 상관관계나 적외선 색이 적외선 방출의 기원을 제안해 줄 수는 있으나 보다 직접적인 근거로 지배적인 적외선 방출 기작을 확인할 필요가 있음을 알 수 있었다. 또한, 엑스레이(X-ray)나 전파 영역에서의 방출과 적외선 방출을 비교하여 그들 사이에도 상관관계가 있음이 확인되었다. 스피쳐 24/70 플럭스비와 플라즈마의 물리량(가스 온도나 밀도) 사이의 좋은 상관관계는 성간 먼지의 가열과 냉각 과정에 대한 기존의 이론을 직접적으로 검증할 수 있었다. 전파에서의 밝기에 비해 상대적으로 적외선 밝기가 약한 초신성 잔해들을 새로이 발견할 수 있었는데, 이것은 은하에서의 전체 적외선 광도에 초신성 잔해가 기여하는 정도가 적음을 암시한다. 우리은하 초신성 잔해의 적외선 탐지 비율(detection rate)과 비교하여 대마젤란운 초신성 잔해의 적외선 탐지 비율은 현저히 높은데, 이는 낮은 성간 소광이 주된 원인일 것으로 여겨진다. 본 연구는 충격파에 의한 공정과 초신성 잔해의 진화를 바르게 이해하는데 중요한 역할을 하는, 초신성 잔해들의 적외선 방출 기작에 대해 토의하였다.

이와 더불어, 아카리 우주망원경으로 근적외선 분광관측을 이용하여 대마젤란 운에 위치한 초신성 잔해 N49에 대한 상세한 연구를 수행하였다. 관측은 적외선에서 밝은 N49의 동쪽 영역 대부분을 포함하는 방식(coarse mapping 방식)으로 이루어 졌으며, 이를 이용하여 다양한 선방출들의 분포를 비교하여 그들 사이의 상관관계를 조사할 수 있었다. 이 초신성 잔해 내부에서 3.3 마이크론의 방향족 피쳐(aromatic feature)을 확인할 수 있었으며, 이는 초신성 잔해와 연관된 3.3 마이크론의 방향족 피쳐을 보고하는 최초의 사례이다. 수소 분자 1-0 O(3) 천이 방출선과 3.3 마이크론 방향족 방출선, 브래킷 알파선(Brα)의 방출선 지도들로 부터, 3.3 마이크론 방향족 피쳐의 분포가 다른 방출선들의 분포와 전반적으로 유사하며, 한편으로 국부적인 차이점도 확인할 수 있었다. 이러한 지역적 차이는 그 지역들의 물리적 조건들을 반영하고 있다고 생각된다. 다른 파장대에서의 아카이브 관측 이미지들을 이용하여 비교한 결과, 방향족 방출이 이온화된 기체나 분자 기체들과 연관되어 있음을 재확인할 수 있었다. N49의 스피쳐 아카이브 자료를 이용하여 3.3 마이크론 방향족 피쳐와 관련된 다른 다환성 방향족 탄화수소(polycyclic aromatic hydrocarbon) 피쳐를 6.2, 7.7, 그리고 11.3 마이크론에서도 찾을 수 있었다. 이 다환성 방향족 탄화수소 밴드들의 세기비를 바탕으로, 이 초신성 잔해 내의 다환성 방향족 탄화수소들이 대체적으로 중성을 띄고 있으며 크기가 작다는 사실을 확인하였다. N49에서 관측된 이 다환성 방향족 탄화수소 방출의 기원을 토의해 본 결과, 이 방출이 충격파를 겪고 살아남았거나 충격파가 도달하지 않은 지역에서 복사 전조에 의해 가열된 다환성 방향족 탄화수소들에 의해 발생할 수 있을 것으로 여겨진다.

주요어: 성간물질: 먼지, 소광 – 적외선: 성간물질: 선과 밴드 – 성간물질: 초신성 잔해 – 마젤란운

학 번: 2006-20463

감 사 의 글

대학원에 입학하여 박사 졸업 논문은 언제 쓰게 될까 상상하던 것이 엊그제 같은데 이렇게 졸업논문의 마지막 페이지를 쓰고 있자니 감회가 새롭습니다. 이 한 편의 졸업 논문이 지난 6년 반 간의 대학원 생활의 결실이라고 생각하니 뿌듯하기도 하고 시원섭섭하기도 합니다. 하지만, 이 논문 한편으로는 표현할 수 없는, 많은 것들을 보고, 듣고, 배우고, 경험한 이 대학원 생활이 저에게는 잊지 못할 행운이였고, 지금의 저에게 또 미래의 저에게 크나큰 밑걸음이 될 것임은 믿어의심치 않습니다. 앞으로 이 곳 대학원을 떠나 더 많은 것을 배우고 익혀, 자랑스러운 제자, 후배, 동기, 선배가 되도록 노력하겠습니다.

아무것도 모르는 저를 정말 잘 이끌어 주신 구본철 교수님. 정말 감사드립니다. 제가 속도 많이 썩인것 같아 죄송하구요. 교수님께 지도 받게 된 것이 저에겐 정말 큰 행운이였습니다. 선생님께 부끄럽지 않은 제자가 되도록 노력하겠습니다. 앞으로도 잘 부탁드립니다. 건강하세요. 대학교 신입생 때 수강한 홍승수 교수님의 일반 천문학 강의는 제게 문화적 충격에 가까웠습니다. 홍승수 교수님의 천문학에 대한 열정은 평생 본받고 싶습니다. 수업을 통해서, 혹은 수업 밖에서, 다양한 방면에 대한 깊은 가르침을 주신 이상각 교수님, 이형목 교수님, 이명균 교수님, 박용선 교수님, 채종철 교수님, 김웅태 교수님, 임명신 교수님, 이정훈 교수님, 우종학 교수님, 이시구로 교수님. 모두 너무나 감사드립니다. 여러 가지 행정적인 일들로 도움을 많이 받았던 김병만 선생님, 김경옥 선생님, 현주 언니, 오은정 조교님, 감사합니다. 고흥에 있는 산적 오빠도 너무 고마워요. 또한, 짧은 시간이었지만 동경대학교에서 생활을 하면서 저의 좁은 시각이 조금이나마 넓혀질 수 있었고 그곳의 학생들로부터 많은 자극을 받을 수 있었습니다. I truly appreciate all of the consideration of Prof. Onaka.

길다면 길고 험난하다면 험난한 이 대학원 생활은 여러 선배님들과 동기들, 후배님들이 안계셨다면 절대로 이루지 못했을 거라 생각됩니다. 먼저, 저의 팀에 졸업하신 선배님들, 재준 오빠, 호규 오빠, 정원 오빠, 지현 언니. 제가 부족할 때마다 도와주시고 많이 가르쳐주시고, 술!도! 많이 사주신거 너무나 감사드립니다. 제가

너무 받기만 한 것 같이 죄송스러울 따름입니다. 현재 함께 동고동락하고 있는 우리 팀원들. 항상 든든한 일교 오빠와 완기 오빠, 성실한 금숙이, 두번 고마운 현정이 현정이 (미션 완료!), 많이 도와주지 못해 미안한 용현이와 예솔이. 대학원 동기이자 판박이 아들, 딸을 낳은 수진언니! 모두모두 고맙고 화이팅 입니다! 같은 팀이 아니어도 제가 물어볼때마다 항상 상냥하게 도움을 주신 호성 오빠, 정덕 오빠, 종철 오빠, 현진 언니, 정현 오빠, 상훈 오빠, 민진 오빠와 태현 언니. 일본서 너무 반가웠던 나래 오빠. 곧 대만에서 만날 효선 언니. 엉덩이가 예쁜 D라인 창구, 신입생때 처음 본 모습이 잊혀지지 않는 진호. 엘리트 강박사 원석 오빠 (혜진 언니에게도 안부 및 순산 기원을 전해주세욥!) 모두 고맙습니다.

너무 예쁜 아들을 둔 종환 오빠, 재안이에게 담에 이모가 빨간차 사준다고 꼭 전해주세요. 누나랑 놀아줘서 고맙다 주비야, 결혼 미리 축하해요 성순 오빠 & 소영 언니, 광장에서부터 벌써 십년이 넘었구나 광호야, 월랑이랑도 잘 지내구. 윗방 아가씨 이슬이, 술은 적당히 마시고 얼른 졸업하렴. 미국 유학생에서 대전 유학생으로 바뀐 민규야, 카톡 할께. 졸업 학기에 옆에서 잘 받아줘서 고마워 규현아. 기숙사에서 라면 끓여줄께 연락해 희수야. 복서 유경이, 우린 퍼스에서 보자꾸나! 네오 진혁이, 원생 대표 그농이, 덕분에 영화 잘 봤어 우영아. 졸업 얼마 안남은 쌀, 도와줄거 있음 얘기해. 술자리에 너 없으면 재미 없더라 주은아. 우리 연구실 204호 식구들, 댄스 가수 정규, 아버님 영복 오빠, 여수에서 온 MC 요셉이, 사이클 가이 다우, 돌아온 윤아 언니, 귀여운 월랑이, 이걸 볼 까 싶은 단라즈, 얼마 얘기 못해본 오정환씨. 그리고 실험실의 훈남 형준이, 점점 사교적인 홍규, 다정한 용휘 오빠, 유학 잘 다녀 오세요 두호 오빠, 태양팀 넘버 원 동욱 오빠, 다재다능하신 성진 오빠, 항상 성실하신 현종 오빠, 이제는 말을 놓는 대성이, 전파의 석호 오빠, 창희 오빠, 동환이, 귀여원 방원이. 신천의 창수 오빠, 현성이, 도형이, 슈스케급 민희. 이 외에도 많은 도움을 주시 못해 미안하고 아쉬운 후배님들, 인성이, 한나, 세명이, 태석이, 용범이, 재진이, 준섭이, 재형이, 승환이, 형묵이, 진훈이. 모두모두 고맙습니다. 혹시 이름이 빠졌을 모든 선후배님들, 동기들 모두 감사드립니다.

대학교때 만나 지금까지 너무 좋은 우정을 유지하고 있는 내 친구들, 명훈이, 성령이, 종찬이, 현정이 너무나 고맙고. 내 절친 효준이. 이번에는 꼭 시험 잘 보길 바라고. 대학에 입학해서 대학원을 졸업할 때까지 끝까지 믿고 기다려주신 부모

님 감사합니다. 공부하는 딸 두셔서 걱정 많이 하셨을 텐데, 앞으로 더 잘할께요. 공부한답시고 집 떠나 모든 집안 일을 떠넘긴것 같아서 언니한테는 항상 미안하고 고마워. 언니가 하고자 하는 모든 일이 잘 되길 바랄께. 끝으로 대학원 생활의 대부분 기간동안 내 버팀목이 되어준 종석이에게 감사와 사랑의 마음을 전하고 싶습니다.